Louisiana Tech University

Louisiana Tech Digital Commons

Spring 5-2023

Chitosan-based Composite for Wound Healing & Biomedical Applications

Abdul-Razak Masoud

CHITOSAN-BASED COMPOSITE FOR WOUND HEALING

AND BIOMEDICAL APPLICATIONS

by

Abdul-Razak Masoud, MS

A Dissertation Presented in Partial Fulfillment for
Requirements of the
Degree Doctor of Philosophy

COLLEGE OF APPLIED AND NATURAL SCIENCES
LOUISIANA TECH UNIVERSITY

May 2023

LOUISIANA TECH UNIVERSITY

GRADUATE SCHOOL

March 30, 2023

Date of dissertation defense

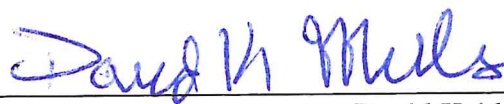We hereby recommend that the dissertation prepared by

Abdul-Razak Masoud

entitled   **Chitosan-Based Composite for Wound Healing & Biomedical**

Applications

be accepted in partial fulfillment of the requirements for the degree of

Doctor of Philosophy in Molecular Sciences and Nanotechnology

David Keith Mills
Supervisor of Dissertation Research

William J. Campbell
Head of Molecular Sciences and Nanotechnology

Doctoral Committee Members:
Gergana Nestorova
Andrew Peters
Teresa Murray
Bryant Hollins

Approved:

Gary A. Kennedy
Dean of Applied & Natural Sciences

Approved:

Ramu Ramachandran
Dean of the Graduate School

ABSTRACT

Polymer composites have witnessed increased research interest in the last decades, and the applications of these materials include drug delivery, tissue engineering, and wound bandages and dressings. Numerous polymers have been studied to fabricate the ideal wound dressing. Making these polymer composites biocompatible, porous, and bioactive with high absorption capabilities is critical to guide cell growth and differentiation and limit their detrimental effects on incorporated therapeutic molecules. This research work aims to address shortcomings of available wound dressings by fabricating a biocompatible, porous, bioactive, and antimicrobial dressing using chitosan (CTS) and carboxymethyl cellulose (CMC) polymers incorporated with zinc-doped halloysites (ZnHNT). In line with the points mentioned earlier, three distinct objectives are proposed in this research that involve using natural biopolymers and nanomaterials. The first objective involves the fabrication and characterization of chitosan/carboxymethylcellulose composite incorporated with zinc-coated halloysites (HNTs) via the solution-gel method, without the use of chemical crosslinkers. Here, the individual biomaterial components used in this research were tested for their inherent antibacterial properties while determining the minimum inhibitory concentration of each constituent biomaterial. A modified physical crosslinking method was used to fabricate a hydrogel biocomposite comprising CTS, CMC, and zinc-coated HNT. The physical characteristics of the hydrogel were assessed via rheological studies. SEM and digital

microscopy were used to observe zinc-coated halloysites and the character of the hydrogel produced. Additional characterization tests carried out in this study include Fourier transform infrared (FTIR) spectroscopy, thermogravimetric analysis, x-ray fluorescence, and x-ray diffraction (XRD). The results showed that zinc doped HNTs, when loaded with a low dose of gentamicin sulfate, stagnated the growth of gram-positive and gram-negative bacteria for extended hours, suggesting the possibility of less dependence on the use of antibiotics. The results also demonstrate the feasibility of fabricating a CTS/CMC polymer conjugate via a simple physical crosslinking method devoid of harsh crosslinking chemical agents.

The second project involved in vitro assessment of the effect of the fabricated chitosan-based composite on wound closure and cell migration. These properties were evaluated via in vitro assays, including proliferation and live/dead assays for cytotoxicity assessment, antimicrobial tests, alizarin red staining and scratch assay. The results suggested that the chitosan polymer conjugate had improved functionalities of biocompatibility, non-toxicity, and antimicrobial properties against gram-positive and gram-negative bacteria. In addition, the fabricated chitosan/CMC composite also showed an improved cell migration effect on human skin dermal fibroblast. This result suggests that the chitosan-based fabricated conjugate could serve as a new promising candidate for wound healing applications.

In a closely related third study, the use of solvent casting method to fabricate CTS/CMC film membranes bearing added functionality for biomedical applications is reported. Material characterization tests were carried out to confirm the presence of the constituted biomaterials. The tests include microscopy imaging and SEM analysis to

determine the physical and surface topography of the fabricated biomaterial. Additional tests carried out include, thermogravimetric analysis (TGA), tensile strength, cell proliferation, cytotoxicity (live/dead), and antibacterial studies. The results of this project showed that the prepared biomaterial was relatively hydrophobic and non-toxic with improved thermal stability. Additional tests will be performed in future studies to obtain the ideal film membrane.

APPROVAL FOR SCHOLARLY DISSEMINATION

The author grants to the Prescott Memorial Library of Louisiana Tech University the right to reproduce, by appropriate methods, upon request, any or all portions of this Dissertation. It is understood that "proper request" consists of the agreement, on the part of the requesting party, that said reproduction is for his personal use and that subsequent reproduction will not occur without written approval of the author of this Dissertation. Further, any portions of the Dissertation used in books, papers, and other works must be appropriately referenced to this Dissertation.

Finally, the author of this Dissertation reserves the right to publish freely, in the literature, at any time, any or all portions of this Dissertation.

Author _____

Date _____

DEDICATION

This Dissertation is dedicated:

To my beloved parents **Hon. Masoud Baba Abdul-Rahman** and **Mrs. Dinah Saadia Masoud,** and to my in-laws for their immense support and words of encouragement that spurred me on when times were tough, and quitting seemed inevitable.

To my gorgeous wife, my dependable companion, my Lubimka **Elmira Masoud**, who has been my strong pillar throughout this PhD journey and continues to provide a shoulder to lean on at all times.

To my wonderful kids **Karim Masoud** and **Malika Masoud**. I am grateful for always giving me a reason to come back home after long lab sessions with a broad smile on my face, and for tolerating the mood swings.

And to my friends who have become more like a family over the many years of us climbing up the educational ladder side by side.

TABLE OF CONTENTS

LIST OF FIGURES

LIST OF TABLES

ACKNOWLEDGMENTS

These projects came to fruition thanks to the abled mentorship, continued support and encouragement of my supervisor, Dr. David K. Mills. I also acknowledge the input of my colleagues in the Biomorph laboratory here at Louisiana Tech University, both past and present, who have contributed immensely to the success of these projects. Additionally, I express my profound gratitude to members of my advisory committee: Dr Teresa Murray, Dr. Gergana Nestorova, Dr. Andrew Peters and Dr. Bryant Hollins for their invaluable contributions towards making this research work thorough and robust. I also extend my sincere gratitude to Dr. Yuri Lvov and his team of researchers, as well as Dr. Sven Eklund for their support and contributions towards the success of this dissertation in diverse ways.

CHAPTER 1

INTRODUCTION

1.1   Research Description

1.1.1   Long Term Goals

The long-term goal of this project is to develop a new polymeric wound healing

and biomedical application composite that possesses modular components for target-

specific applications. The carrier system in the form of halloysite nanotubes serves as a

delivery tool (nano container) for various drugs and antibiotics embedded within the

lumen, as well as a point of attachment for metal nanoparticles for additional

functionality. The successful implementation of the project will serve as the basis for

developing polymer conjugates with additional properties that will enhance the

manipulation of cellular microenvironments for wound healing, regenerative medicine,

and tissue engineering applications.

1.1.2   Hypothesis

Composites used for wound dressings, regenerative medicine, and tissue

engineering applications ideally should be able to provide an environment that is suitable

for mechanically supporting the area of trauma, providing surface area for the cells to

attach, and forming interconnecting pores to allow the migration of cells and growth

factors to the injury site. We hypothesize that the nanocomposites fabricated in this work

possess the above properties due to the inclusion of carboxymethyl cellulose, chitosan,

and halloysite/drug-doped halloysite. In addition, incorporating halloysite nanotubes (HNTs) and metalized (zinc) halloysite nanotubes will provide mechanical properties and additional functionalities such as antibacterial, tissue regeneration, and sustained antibiotic release.

1.1.3 Scientific novelty and significance

Most patients admitted to a wound care center are typically referred to treat chronic wounds. In most patients, these have been present for months or years, and for many patients, they also have multiple attendant medical problems that can impair or delay wound healing [1]. A chronic wound is difficult to heal and requires a complex treatment plan [1], [2]. Wound bed preparation through debridement and granulation tissue promotion is required to encourage proper wound closure in such complex wounds [3]. Negative pressure wound therapy or advanced wound dressings, such as oxidized regenerated cellulose (ORC)/collagen/silver-ORC dressings (among others), are often used to promote the development of granulation tissue in the wound bed [4]. In wounds requiring further treatment, skin substitutes or epidermal grafting may be necessary to promote re-epithelialization, especially in large chronic wounds [5], [6]. Wound dressings are topical materials applied to the surface of wounds to enhance the healing process by reducing healing times and preventing complications due to bacterial infections [5]–[7]. An ideal wound dressing must keep moist at the injury interface and have desirable biocompatibility and gas permeability [7]. Biodegradable composites such as bandages, coatings, hydrogels, films, mats, and sponges have been developed and formulated for treating wounds and dressing burn sites [8]–[11]. A bioengineered scaffold for wound healing and tissue regeneration should mechanically support the area

of trauma, provide a surface area for the cells to attach, and contains a network of interconnecting pores to allow cell migration, proliferation, and differentiation [12]. Making the materials bioactive to guide cell growth and differentiation is critical for its effectiveness. Cells are guided by chemical cues and their interaction with the surrounding substrate and its physicochemical properties [13].

Chitosan, cellulose, collagen, and gelatin have been widely studied as wound dressings because of their hydrophilicity and non-cytotoxicity [14]. Polymers are the most suitable materials that could potentially be engineered to possess most of the properties of an ideal wound dressing. Polymers are increasingly being used in the fabrication of smart wound dressings, that is materials with an ability to respond to biochemical and biophysical stimuli such as pH, temperature, enzymes, magnetic force, and light [15]. For the development of these smart wound dressings, natural polymers such as chitosan are preferred to synthetic polymers owing to their non-immunogenicity and biomimetic capabilities [14].

Chitosan (CTS) is a polymer obtained by deacetylation of chitin [16]. It is biocompatible, biodegradable, non-cytotoxic, readily undergoes degradation, and can be structurally modified using simple chemical modifications. One mechanism to improve chitosan functionality is by subjection to modifications through covalent crosslinking with other compounds [17].

Applications of cellulose have attracted increasing attention in recent years. As one of the most abundant natural polymers, cellulose, and its derivatives show excellent biocompatibility, thus being considered viable for biological and medical applications [18]. Cellulose is currently one of the most promising bio-based polymeric resources.

Due to the increasing demand for sustainable and biocompatible products, a number of functional varieties of cellulose have been developed for different biomedical applications [19]. CMC has been used in the food processing and cosmetics industries as a thickener, edible film and coating agent, emulsion stabilizer, and a carrier of functional materials [20], [21].

Carboxymethyl cellulose (CMC), as a representative water-soluble cellulose derivative, is manufactured by reacting sodium monochloroacetate with cellulose in alkaline. It contains abundant hydroxyl groups so that it can easily form hydrogels with decent structures [8], which retain water molecules in a 3D gel structure, and this property contributes to tuning the flow behavior of aqueous suspensions and solutions [10]. However, the antibacterial and mechanical properties of CMC are not satisfactory [22] and its application in the form of CMC-based films is limited owing to the hydrophilic nature and rather inferior mechanical properties [21]. Reinforcement with nanoparticle fillers such as nano clays [23] and nanometals have increased their material properties [24].

Despite advancements in tissue regeneration, wound dressings that possess all the relevant properties for enhancing wound healing are yet to be fabricated. Therefore, this research developed a novel polymer composite as a hydrogel, film and a patch/textile suitable for wound dressing with improved wound healing properties.

1.2   Objectives

In lieu of all the above-mentioned points, this dissertation has three distinct objectives:

- Objective 1: Fabrication and characterization of sol-gel chitosan/carboxymethyl cellulose composite incorporated with zinc-doped halloysites (HNTs) and characterization of its physical and chemical properties.

- Objective 2: In vitro assessment of the effect of the fabricated chitosan-based composite on wound closure and cell migration.

- Objective 3: Biofabrication and material characterization of Chitosan/Carboxymethyl cellulose solution casted membranes for various biomedical applications.

CHAPTER 2

LITERATURE REVIEW

2.1   Evolution of Biomaterials

Biomaterials are commonly described as materials that serve as modes of contact, mostly with biological systems. This term, up until approximately 70 years ago, was nonexistent. Today, it encompasses synthetic and natural materials used in medical and nonmedical fields, including chemistry, biology, mechanics, material science, and bioengineering [25]. The field of biomaterial had continued to expand since its inception, which can be traced to 32,000 years before the common era, where mummified remains of ancient Egyptians showed sutures made using fibers, tendons, wool threads, and animal sinew [26], [27]. The use of gold and silver for dental repair traces back to the 16th century in Europe, with technological advances such as X-ray, the discovery of anesthesia, and the emergence of scientific societies and journals furthering this field up into the 1960s. A biomaterials symposium was held in 1969 at Clemson University; that book marked the start of an integrated effort between medicine and engineering to enhance the field of biomaterial research, with the first International Congress of Biomaterials taking place in 1978 [28].

Arguably, a pre-advanced era of biomaterial was pioneered by Harold Ridley, who noticed the self-healing capability of canopy plastic, poly(methyl methacrylate), for use as lenses, Charnley, who focused on hip implants and Kolff whose worked revolutionized kidney dialysis. Their works served as foundation for evolving the field of biomaterials, particularly birthing the idea of biomaterials releasing toxic substances thus making them non biocompatible.

Knowledge of wound healing biology is a force driving the new generation of biomaterials termed biologically inspired biomaterials. As a result, novel biomaterials with enhanced properties and the ability to perform desired functions mimicking in vivo processes continue to emerge. These properties are conferred to biomaterials via various approaches, including surface modification by additive manufacturing, 3D printing, finite element modeling, and nanotechnology [28].

2.1.1   Polymers and Polymer composites

Polymers, long chains of covalently bonded natural or manmade molecules, makeup the largest class of biomaterials [1]. The units in a polymer are referred to as monomers and can be made of the same molecule or can have more than one type. Reflecting this diversity, polymers are commonly called plastic, rubber, proteins, peptides, oligonucleotide, and other names that allude to the type of monomers in the polymer. Thousands to hundreds of thousands of monomers are typically crosslinked to form long polymer chains for various biomedical applications.

DNA, RNA, and proteins are a few examples of natural polymers (bio-based) that continue to be manipulated and genetically engineered, leading to the discovery and development of biological functions. The inherent properties of these natural polymers

have been employed to form unnatural materials, a prime example being the formation of molecular screens from grids of DNA due to the ability of this molecule to form double strands.

Proteins another large class of natural polymers, are comprised of sequentially added amino acids held together by covalent bonds in a linear chain [2]. This arrangement gives rise to the primary structure of the protein. The secondary structure of proteins is a result of the natural folding of proteins into patterns due to the electrical charges of the constituent amino acids. A protein will continue to fold into a more complex, ***tertiary structure*** because of natural attraction and repulsion of amino acids in the secondary structure and with the help of chaperone proteins inside the cell. Some proteins are made of two or more proteins. In this case each of the proteins is known as a subunit. When this occurs, it is known as ***quaternary*** structure [3]. Polymer chains of proteins are assembled mostly via condensation reactions, where the reaction produces water [2].

Due to the repetitive nature of proteins, they serve as ideal candidates for understanding how single unit changes via genetic engineering could result in the production of biomaterials with unique desirable material properties such as self-assembly, mechanical strength, adhesion, and thermal responsiveness.

Natural biomaterials can be classified into protein-based biomaterials, polysaccharide-based biomaterials, glycosaminoglycan-derived biomaterials and tissue-derived biomaterials [4]. Polysaccharide-based, protein-based, and glycosaminoglycan-derived biomaterials, particularly chitosan, cellulose and its derivatives, Hyaluronic acid,

and collagen, continue to be actively researched for biomedical and tissue engineering applications as they have been found to better mimic the biological and mechanical function of the native extracellular matrix (ECM) in both repair and replacement cases of body tissue [5]–[7].
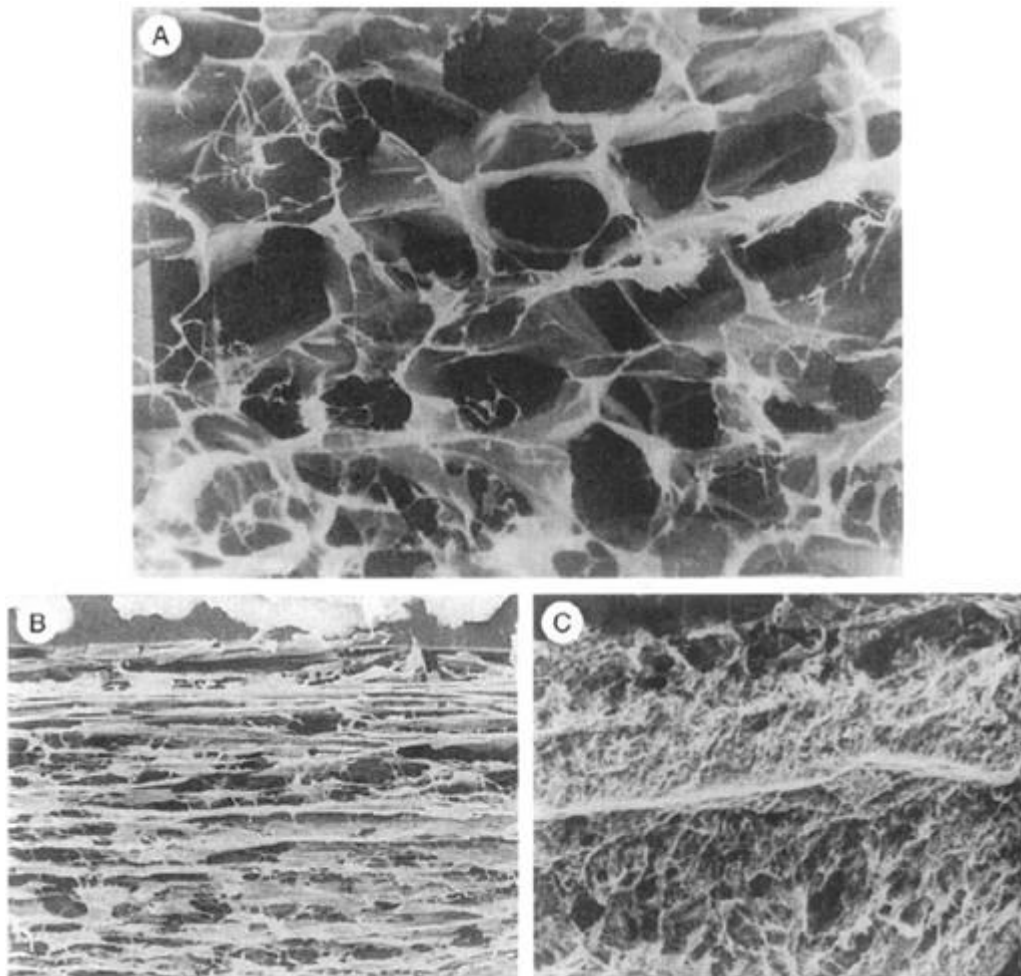
Figure 2-1 SEM images of pore structures obtained from collagen-GAG copolymers, adapted from Ratner et al 2004.

The extracellular matrix (ECM) is the non-cellular component that forms a porous scaffold withing which biochemical and biomechanical process occur. It is primarily made of water, proteins, and polysaccharides. The ECM is ubiquitous, but unique to each tissue [8]. The ECM is fundamental to wound healing and tissue regeneration with it playing roles in cell adhesion and cell behavior. Components of ECM are increasingly being studied in attempts to reconstruct damaged ECM during injury. Blomback and co-authors discussed in detail the use fibrin to fabricate a natural biodegradable scaffold [9]. Despite the huge strides made, there remains the need for well-defined microenvironments that would augment and supplement the native environments for wound healing and tissue regeneration.

Chitosan (CTS)

Chitin, a polysaccharide like cellulose, is mainly extracted from the exoskeleton of crustaceans, insects, and fungi and is characterized by a β-(1-4) glycosidic bond and can be transformed into the water-soluble chitosan following deacetylation in robust alkaline solutions. The structure of chitosan is similar to that of cellulose, except at carbon-2, where an amino group replaces the hydroxy group of cellulose. Although the *β*-(1-4) anhydro-glycosidic bond of chitosan is also present in cellulose, the characteristic properties are not the same as cellulose. Thus, chitosan is made of repeating units of N-acetyl-D-glucosamine and D-glucosamine copolymers with a degree of acetylation of at least 60%. It is obtained from chitin by chemical hydrolysis under alkaline/acidic conditions or by enzymatic treatment [36].

Molecular weight and F_A (acetylation) value are major factors implicated in the solubility of chitosan at neutral pH. At this pH, highly chitosan has been shown to be

soluble when its molecular weight is lowered close to the degree of polymerization. High molecular weight chitosan on the contrary is soluble at neutral pH when the degree of acetylation is above 40% [10]. The insolubility of chitosan in aqueous solutions affects an important property as antimicrobial efficacy likely because its positive charge is neutralized at higher pH thus, limiting its interaction with negative charges in the bacterial cell wall and membrane [11] [12]. This linear natural polymer is also structurally similar to glycosaminoglycans that play crucial roles in cell-to-cell adhesion within the extracellular matrix (ECM).

Chitosan's physical properties can be tuned by changing its degree of deacetylation, molecular weight, degree of depolymerization, and by modifying its interactions with both hydroxyl and amine groups that are present in its molecular backbone for added functionality. These modifications can be classified into physical modifications, chemical modifications, and molecular imprinting [13].

Table 1 Properties improved by modification of chitosan.

Chitosan polymer	Modification to chitosan backbone	properties
Quartenized chitosan[40]	N,N,N-trimethyl group added N-propyl-N,N-dimethyl group added N-furfuryl-N,N-dimethyl	Water-soluble at acidic, basic and neutral pH Improved antibacterial activity
Carboxymethyl chitosan[41]	carboxymethyl group added	Low toxicity, improved drug encapsulation properties
Hydroxy butyl chitosan[42]	Hydroxy butyl group added	Improved thermal response
N-alkylated disaccharide chitosan[43]	N-alkylation with mono and disaccharides	Improved antimicrobial property

Chitosan has been shown to possess various biological properties, including it being biocompatible: since it is of a natural origin, it is safe and non-toxic to mammalian cells but selectively binds to and destroys microbial cells, enhances tissue regeneration, accelerates the formation of osteoblasts, hemostatic, fungistatic, bactericidal, antitumor, or anticancer, anti-cholesteric, central nervous system depressant, immunoadjuvant. It is also very abundant and is obtained from various sources compared to other natural polysaccharides [17].

These properties, among others, increase the use of chitosan for various biomedical applications. For example, chitosan has been shown to possess strong hemostatic activity independent of the host coagulation pathway in wound healing, as shown by multiple studies [40], [41].

Chitosan has also increasingly been used in the industrial space. A promising technology involves the use of chitosan as edible coatings in the food manufacturing industry for extending the shelf life of fruits and vegetables. Chitosan has been used to create protective films around fruits and vegetables, thus limiting water evaporation and subsequent dehydration of these produce. The thin film membrane formation typically involves dipping, air brushing, casting [14], or spraying chitosan directly unto the food produce. Abhijeet Bhimrao Muley et al prepared a chitosan and whey protein isolate conjugate film for encapsulating strawberries which significantly extended their shelf life [14]. Similarly, Gianfranco Romanazzi et al identified and described the recent applications of chitosan on other fruits including the potential of chitosan preventing fungal decay and reducing product waste [15]. The cosmetic industry has witnessed the use of chitosan for various purposes [16]. Researchers in a recent study combined chitosan with hyaluronic acid and collagen for fabricating thin films via solvent evaporation. The fabricated films were shown to possess enhanced mechanical properties capable of improving hair thickness [17]. Chitosan and its derivatives have also been used in the paper industry, the textile industry, and agriculture [18].

The environmental application of chitosan has seen it being used a flocculating agent, where small colloidal particles in wastewater are destabilized and further aggregated into larger flocs for subsequent removal [19] Chitosan is also used as a chelating agent for trapping heavy metals [20], [21] for removing pollutants organic in nature [22].

Carboxymethyl Cellulose (CMC)

Cellulose is mostly modified by making chemical alterations to the hydroxyl groups in the cellulose backbone resulting in a cellulose ester or a cellulose ether [23].
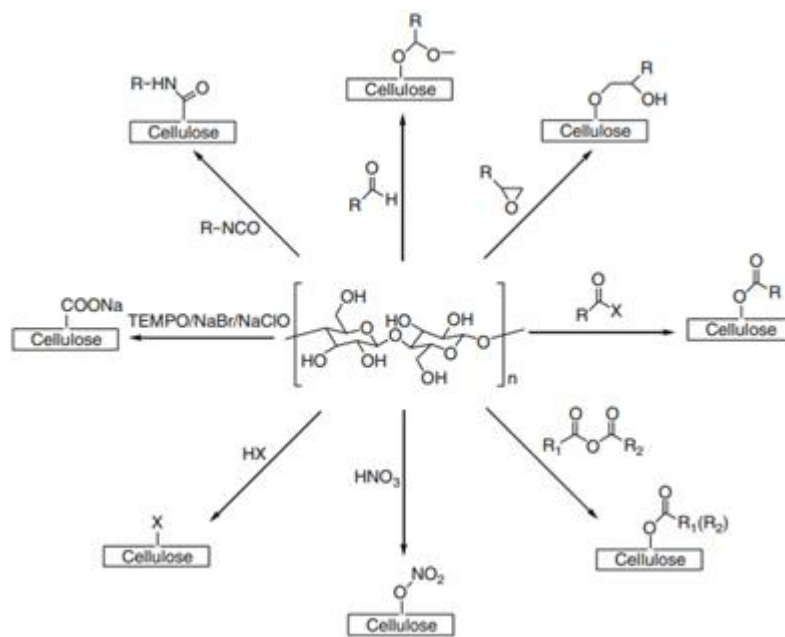
Figure 2-2 Chemical structure of cellulose derivatives

Carboxymethyl cellulose (CMC) is one of such cellulose derivatives, specifically a cellulose ether which is an anionic, linear, water-soluble polymer of anhydro-glucose with each unit held to the next by β-1-4-glycosidic bonds. The sources of CMC have gradually evolved from the typical wood-based plants to other low-cost and greener alternatives including recyclable materials such as waste paper [24] and waste textile [25] at laboratory scale. On a commercial scale the main sources of cellulose for CMC production are cotton linters and wood. CMC is ultimately obtained from cellulose in a two-step process that involves suspending cellulose in an alkaline medium followed by

reacting it with monochloroacetate [26]. Manipulations of cellulose and cellulose derivatives including carboxymethyl cellulose via hydrolysis or mechanical treatment result mainly in the formation of nano whiskers and nanofibers respectively [27].

Similar to chitosan, the applications of CMC and CMC-based hybrid materials encompass a wide range of fields: biomedical, pharmaceutical, cosmetics, construction, food, plastics, paper, and textile industries.

Researchers in the field of biomedical science successfully designed a composite film comprising of carboxy methyl cellulose/poly vinyl alcohol doped with magnesium oxide nanoparticles for skin tissue engineering. The fabricated film possessed improved properties such as cell adhesion, desired swelling, controlled degradation, and tensile strength among others [28].

Another group of scientists in the pharmaceutical field found a multi-component-crosslinked carboxymethyl cellulose composite to be a safe carrier of antibiotics for the oral delivery of gentamicin [29]. With regards to textile digital printing, Javed Sheikh and his co-authors recycled cellulosic waste into carboxymethyl cellulose and subsequently used it as a thickener for textile printing. The authors demonstrated that there was no decline in color and strength properties of the printed textile [30].

The food industry is in constant need of odorless and physiologically inert thickeners, emulsion, and adhesive stabilizers for packaging and other purposes and in this regard, Gregorova et al fabricated a PVP-CMC film as a packaging material that fulfilled several of the above-mentioned objectives [31]. Additionally, researchers found that the stability of acidified milk drinks increased when CMC with decreased degrees of

substitution at positions C-2 or increased degrees of substitution at position C-6 was used as a stabilizer [32].

Despite the numerous advantages associated with the use of CMC in the above-mentioned fields, the prospect of utilizing CMC for in vivo bio-sensing, developing CMC-based composites for stimuli-responsive applications, developing novel CMC-based biomaterials for 3D and 4D bioprinting processes remains to be fully explored [33].

Hyaluronic Acid (HA)

This molecule, a major component of connective tissues, comprises repeating disaccharide units of N-acetyl-d-glucosamine and d-glucuronic acid. This structure is highly modifiable to serve for the creation of varying forms of this molecule, thus providing versatility of the use of HA in the various fields while satisfying the required characteristics for each field of use. Hyaluronic acid possesses numerous bodily functions, including but not exclusive to cell signaling, cell migration, and wound repair. HA has been employed in biomedical for making hydrogels [33], [62], fibers via electrospinning and blow spinning [63], scaffolds [64], and nanoparticle-containing solutions.

Polymer composites comprise of two or more polymer materials held together in a dispersed or matrix phase for the purpose of attaining a novel, improved characteristic from those of their individual components. Considering the concept of matrix phase, polymer composites are divided into metal matrix composites, ceramic matrix composites and polymer matrix composites. Another classification based on reinforcing material categorizes polymer composites into Fibrous, particulate, and laminate polymer composites [34]. Composite materials were sub-classified by Zhago et al iton metals,

ceramics and polymers (based on matrix material), as well as fibrous, particulate and luminate (based on reinforcing material) [29].

Biodegradable and non-biodegradable composites as well as a combination of the two (hybrid) when used for mimicking living materials, make up a group of fibrous composites classified as natural or synthetic biocomposite. These materials tend to have excellent biocompatibility, improved mechanical strength and better environmental degradation, thus enhancing their safe application in many fields [35].

2.2   Synthesis of Polymer Composite Biomaterials

The use of polymer composites for specific biomedical applications is directly or indirectly influenced by the techniques used for fabricating such polymer composites. A few of the fabrication techniques include solution blow spinning, electrospinning, melt-extrusion, solution mixing, cast molding and in situ methods [36].

2.2.1   Solution blow spinning

This is a facile technique for fabricating non-woven polymer fibers from a concentrated polymer solution subjected to a high-pressure gas source. For this process, it is important that the polymer is dissolved in a volatile solution. Unlike electrospinning, solution bow spinning does not require sophisticated apparatus; cosmetic airbrushes have efficiently been used to make fibers with varying parameters [37].

As an alternative to electrospinning, precise and site-specific in situ deposition of uniform layers of nanofiber meshes and scaffolds directly over large areas and areas where conventional suturing may not be possible become feasible via solution blow spinning [38], [39]. Recently a group of researchers used the blow spinning technique thus, overcoming the limitations of conventional electro spun fiber fabrication to generate

gelatin-based nanofibers that exhibited excellent biocompatibility and supported stem cell

growth [40].

Blow spinning technique is a low cost, high throughput technique with a plethora

of advantages over alternative fabrication methods and a growing demand in the global

nanofiber market. However, reproducibility and alignment of micro-and nanofibers

remain a few of the challenges associated with this technique.

2.2.2   Electrospinning

This fabrication technique allows the processing of with great precision (2 nm to

several micrometers) via high electric field resulting in polymers and composites with

larger surface area, mechanical strength, and ease of functionalization [41]. The

electrospinning process involves an electric field formed between a syringe and a

grounded collector in either a coaxial or near field setting [42].
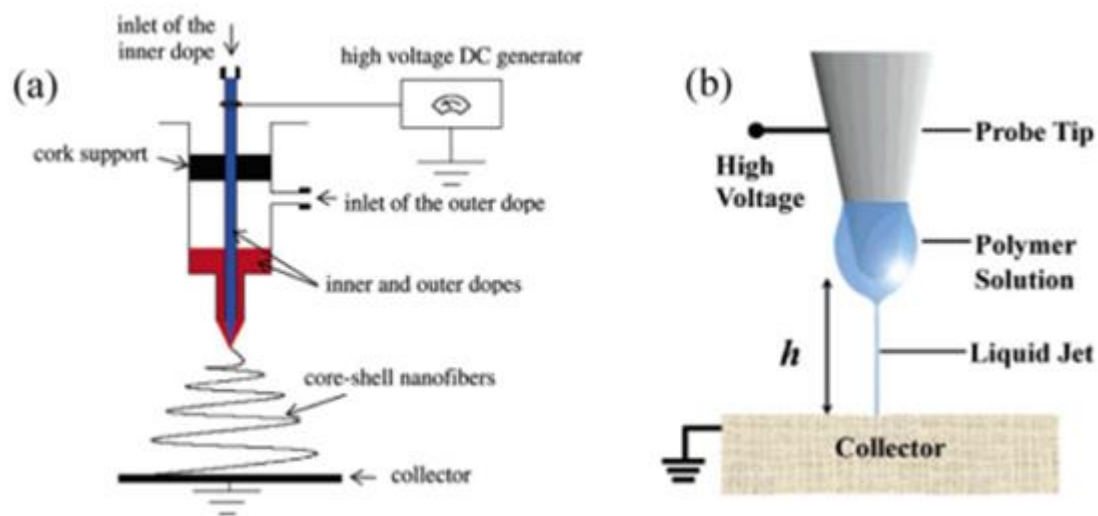
Figure 2-3 Diagram of electrospinning apparatus (a) Coaxial electrospinning (b) near-field electrospinning, adapted from Liu et al [77]

A direct current is applied to a polymer solution, or a solution containing a mixture of polymers and evaporated to produce fibers which are collected on the collector. With respect to wound healing and tissue engineering electrospinning results in easily modified materials that mimic the native extracellular matrix. This technique also allows for flexibility with choosing suitable components for controlled delivery of drugs and other biologically active additives [43].

2.2.3   Melt-extrusion

This is an additive manufacturing that involves the use of an extruder with nozzle for melting and extruding polymer and polymer composite filaments. These filaments are subsequently used in various fields that require simple layer by layer deposition in bottom-up procedures as well as 3D layer deposition at the nano, micro and macro scales [44]. Fengze Wang and co-authors carried out a solvent-free fabrication of polycaprolactone (PCL) and hydroxyapatite (HA) composite filament for 3D printing a scaffold with increased compressive strength, surface roughness, porosity, and elastic modulus, using melt-extrusion technology [45].

2.2.4   Solvent casting

This composite fabrication method is a simple, wet manufacturing process that involves minimal non-sophisticated equipment. The process requires the mixing individual polymer components and any additive material in the appropriate solvent

(typically water or a volatile solvent), mechanical agitation, followed by casting and subsequent drying to remove the solvent [46].
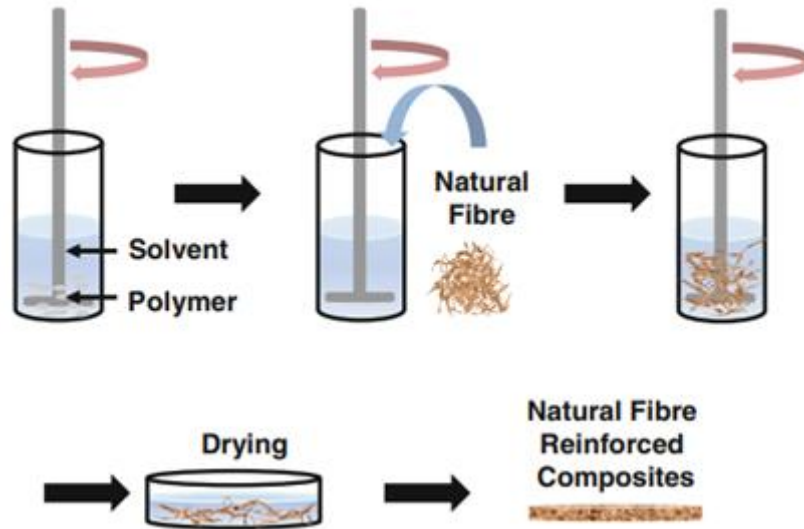
Figure 2-4 Fabrication of polymer composites by solvent casting method, adapted from [81]

2.3   Current and Future Applications of Polymer Composites

The growing demand for new biomaterials has necessitated increased research into fabricating new materials with a wide range of properties using both natural and synthetic sources. These novel polymer biomaterials are widely used in medical practice for fabricating heart valves, artificial joints, ligaments, and tendons, dental implants and nerve stimulating implants. The field of wound healing and tissue regeneration has also seen increased use of combination biomaterials for fabricating scaffolds that support cells and bioactive molecules.

Synthetic biomaterials in the form of hydrogels have increasingly been fabricated owing to their high-water content and tissue-like structure. These hydrogels form

crosslinked polymer networks that are swellable without dissolving in aqueous

environments. Since the pioneering fabrication of hydrogels using synthetic poly-2-

hydroxyethyl methacrylate by researchers Lim and Wichterle for biological use [47],

hydrogels continue to be of interest to researchers.

Advances in technology mean that new hydrogels with satisfactory cytotoxicity

and biocompatibility are increasingly being fabricated via modifications in the chemical

structure of the materials used. Poly(hydroxyethyl methacrylate), a commonly used

hydrogel polymer was crosslinked with polyethylene glycol di methacrylate via free

radical crosslinking copolymerization. The resultant hydrogel biomaterial was shown to

be porous (for controlling permeation of cells and nutrients), with a favorable drug

release profile [48].

Other chemically crosslinked polyethylene glycol hydrogels have been fabricated

specifically for use in drug delivery systems for carrying drugs to disease targets. These

biomaterials form matrices for controlled biomolecule release of single [49], [50] and

multiple therapeutics [51] for regenerative purposes.

Another interesting field of synthetic hydrogel application envelopes around

injectable implants and soft tissue fillers. Polymer hydrogels and hydrogels from polymer

composites are modified to polymerize after injection in physiological conditions making

them attractive for new tissue engineering applications. The crosslinking is feasible either

under chemical influence with initiators [52] or without [53], or via physical means void

of any chemicals [54].

In the experiments carried out by Zhu et al, an initiator complex comprising of ammonium persulfate and N,N,N,N-tetramethyl ethylene diamine were used polymerize macromers of poly(ethylene glycol) in a redox-initiated reaction. The hydrogel formed showed potential for use a tissue engineered material free of porogen techniques and less invasive in implantation [52].

Despite visible progress in fabricating hydrogel materials via chemical crosslinking, residue initiators and gelation agents remain plausible sources of biocompatibility issues.

2.4   Chitosan and Cellulose Blends

Multi-component composites possess promising functionalities that typically cannot be obtained from the individual components. For instance, the strong hygroscopic nature of chitosan, its purity as well as difficulty with miscibility confer multiple challenges working with this polymer, hence the decrease in number of chitosan-based products on the market [27].

In chitosan and cellulose polymer blends, the amino groups present in the chitosan molecule facilitate an intermolecular interaction with cellulose and its derivatives via hydrogen bonding. Specifically, the ionized amino (NH^{3+}) groups of chitosan get electrostatically attracted to the carboxylic (COO^-) groups of the anionic polymer [55]. The resultant composites have been shown in various studies to have improved thermal stability and antibacterial effect, [56]

2.5   Nanoparticles

Nanoparticles have seen recent use in fields where biological applications intercept with nanotechnology. For example, the emergence of antibiotic-resistant pathogens remains one of the biggest threats to global health, food security, and development, with the World Health Organization reporting an ever-increasing range of infections globally [88]. The estimated number of illnesses caused by these antibiotic-resistant pathogens in the USA is 2,868,700 annually, as reported by the Centers for Disease Control (CDC) [88].

A promising approach to counteract antibiotic resistance emergence involves using nanoparticles with inherent antimicrobial properties. Several studies have demonstrated the capacity of metal nanoparticles and metal oxides such as iron oxide, magnesium oxide, zinc oxide, copper oxide, silver nanoparticles, gold nanoparticles, and titanium oxide to effectively combat bacterial infections via non-specific bacterial toxicity mechanisms [89].

Another existing approach involves using nanocarriers that efficiently deliver antibiotics to their targets, thus increasing the effectiveness of the antibiotic agents [90].

2.5.1   Copper oxide (CuO)

Metal oxides of copper, a transitional metal has found several applications as a nanomaterial in various fields including energy, biomedical and environment studies. The nanomaterials have gained increased interest among researchers for the assessment of their biological activities and photocatalytic activities [57]. Others have probed copper oxides for their antimicrobial [58] and anticancer [59] properties.

In the field of wound healing and tissue regeneration, copper oxide nanoparticles have been used as active agents for promoting growth of new blood vessels, and regenerating skin which ultimately enhance wound healing [60], [61]. Copper nanoparticles are mostly synthesized by physical, chemical, and biological approaches as comprehensively reviewed by Manoj B. Gawande and co-authors [62].

2.5.2   Zinc oxide (ZnO)

The enormous physiological functions of zinc in the body makes it an nanomaterial especially for biomedical applications [63], [64]. The excellent, broad spectrum antibacterial properties of zinc nanoparticles against gram positive bacteria as well as its toxicity against cancer cells by apoptosis through lipid peroxidation were reported by Premanathan and co-authors. The authors suggested that ZnO toxicity against cancerous human myeloblastic leukemia cells was exerted in a dose-dependent manner via apoptosis and the generation of reactive oxygen species (ROS). They also found that ZnO significantly suppressed the growth of *E. coli, P. aeruginosa, and S. aureus* [65]. Similarly zinc oxide was shown to be effective against gram negative bacteria [66].

2.5.3   Silver nanoparticles (AgNPs)

The medical, pharmaceutical, food, healthcare, cosmetic and many other industries are in demand of silver nanoparticles. The physical, chemical, and biological properties of these nanomaterials are readily modifiable hence, their increased application across the above-mentioned fields as antibacterial agents, components of medical devices, and additives in wound dressings [67].

AgNPs are synthesized via physical, chemical, and biological means. The physical and chemical approaches for synthesizing AgNPs have been shown to be costly

and not hazard-free. There is therefore an increase in preparation of AgNPs via biological means (green synthesis) in conjunction with microorganisms such as Escherichia coli, strains of Lactobacillus, Pseudomonas stutzeri, and Fusarium oxysporum [68].

Moreover, biological synthesis is advantageous due to ability of controlling particle size, the high throughput and stability of AgNPs produced, and this method occurs mostly in a single step. The green synthesis method has been used to obtain AgNPs from various sources including plants and small molecules such as amino acids and vitamins [69].

Post synthesis, AgNPs are characterized for the elucidating important physicochemical aspects regarding size and shape using analytical techniques such as XRD, FT-IR, SEM, TEM, and AFM. Typically, SEM together with EDX allow for determining the morphology and elemental composition of the nanoparticles [70]. TEM analysis produces results similar to SEM but with better resolution since thin slice samples are used with electron beams traversing the samples [71]. AFM analytical technique, when used for physicochemical characterization of nanoparticles allows for assessing the dispersion and aggregation rate of the nanomaterial using scanning modes different from SEM and TEM [72].

Silver nanoparticles have been shown to be one of the most promising alternatives for the treatment of cancer. Its ability for use as nanocarriers in targeted drug delivery against tumor cells is discussed by Helena Gomes [73]. Th antibacterial and anti-inflammatory properties of silver nanoparticles have also been discussed in detail by Tamara Bruna and Kenneth Wong respectively [74], [75].

2.5.4   <u>Halloysite</u>

Halloysite nanotubes (HNTs) are ubiquitous, easily accessible nanomaterials that obtained from clay mineral deposits [76]. Structurally, halloysites are hollow and tubular in nature with two layers of aluminosilicate ($Al_2Si_2O_5(OH)_4nH_2O$). Halloysites exist in the sub-micron range with an outer diameter range of 50–80 nm and an inner lumen ranging 10-15 nm [77]. With an aspect ratio of approximately 50, HNTs have a relatively large surface area and a lumen that can be loaded with various materials, such as drugs, metals, and biomacromolecules making it an excellent nanocarrier [78]–[80].

The inner lumen of HNTs has successfully be filled with antibiotics, cancer drugs, biomolecules, dyes and a wide range of active agents mainly using vacuum as the driving mechanism [81]–[84]. The outer surface of halloysites has also been modified with nanomaterials using varying techniques for a number of applications [85], [86]. HNTs have increasing been used as filler nanocomposites [87], nanocarriers of drugs [88], adsorbent materials [89], and as catalysts [90] due to their tubular microstructure, biocompatibility, high mechanical strength, thermal stability, and potential for surface modification [86].

 Research has shown halloysite nanotubes to be non-cytotoxic on several cell types, including chondrocytes, dermal fibroblasts, osteoblasts, and stem cells on halloysite-doped composites. These cells proliferated and maintained their cellular phenotype after exposure to varying concentrations of HNT [91]–[93].

The low level of cytotoxicity exhibited by halloysite nanotubes makes them optimal candidates for wound healing and polymer-based tissue regeneration applications [94].

Surface modification of halloysite nanotubes

Free radical modification

The free radical modification of halloysite surfaces is feasible owing to the presence of hydroxyl groups on both outer HNT surface and the surface of the inner lumen, to which reactive monomers could be attached. In a radical polymerization process Liu and co-authors grafted polymethyl methacrylate (PMMA) unto the surface of HNTs with the resultant modified HNTs incorporated into poly(vinyl chloride). This significantly improved the toughness, strength and modulus of the PVC [95]. HNTs gained added functionality through free radical modification when they were surfaced modified by the coating with polymers via atom transfer radial polymerization. The authors reported that the resulting composite demonstrated improved wettability properties [96].

 Metal sintering of halloysite nanotubes

Sintering of halloysite nanotubes is a cost-effective, chemical free process of modifying the surface of halloysites at high temperatures under dry conditions. Temperature of 300°C and beyond cause the dissociation of most metal acetylacetonates, allowing the free metal ions to attach the outer surface of halloysites via strong electrostatic interactions [97]. Jammalamadaka and co-authors deposited barium sulfate nanoparticles on the surface of HNTs for subsequent use in enhancing the mechanical properties of PMMA bone cement [98].

Electrodeposition for metalizing HNTs

The phenomenon of electrolysis where direct current is used to drive an otherwise non-spontaneous reaction can be employed for depositing nanoparticles onto halloysites,

thus modifying its surface and lumen [99]. This technique is advantageous over other existing HNT modification methods owing to the low cost involved. The resultant hybrid HNT nanocomposites have found applications in nano-bio sensors, biomedical devices, theragnostic systems, radiation adsorption composites, industrial catalytic systems, and antibacterial nanomaterials [100]. Humayan and co-authors demonstrated a voltage regulated electrophoretic deposition of zinc nanoparticles onto the surface of halloysites [85].

Physical Adsorption or Self-Assembly

Halloysites have been shown to have the tendency of adhering ions onto their surfaces through physical interactions between opposite charges. Positively charged metal ions were reported to be electrostatically bound to halloysites forming a cluster of metals on the surface via an intercalation mechanism [101].

Direct adsorption of silver acetate onto halloysite clay nanotubes was also shown to be feasible through metal ion reduction in aqueous halloysite dispersion based on the concentration and particulate size of the silver nanoparticles [102]. Wenjing Yang and co-authors designed and fabricated antibacterial and magnetic HNTs by adsorbing Fe_3O_4 magnetic nanoparticles onto HNTs via electrostatic adsorption.

Further manipulations of the modified halloysites conferred additional properties such as improvement in cell activity, antibacterial activity, and increased cell proliferation [103]. Fabrication conditions such as increased temperature and pH have been shown to facilitate the self-assembly of silver ions onto the surface of unmodified halloysite in an aqueous solution [104].

 Solvothermal

Modification of halloysites by solvothermal synthesis usually involves subjecting HNTs to a solvent-mediated reaction in a vessel capable of withstanding high pressure and temperatures surplus of the boiling point of the reaction medium [143]. TiO2 and ZnO have been deposited onto Halloysites by solvothermal synthesis for improved photocatalytic activity and for improved mechanical and antimicrobial properties respectively [144], [145].

2.6   The Wound Healing Process

Homeostasis, inflammatory, proliferation and remodeling make up the overlapping stages of wound healing. The sequence of physiological events immediately after an injury is geared towards restricting or completely halting bleeding [105], [106]. These 4 stages of physiological events remain the same whether the healing process occurs by primary or secondary intention.
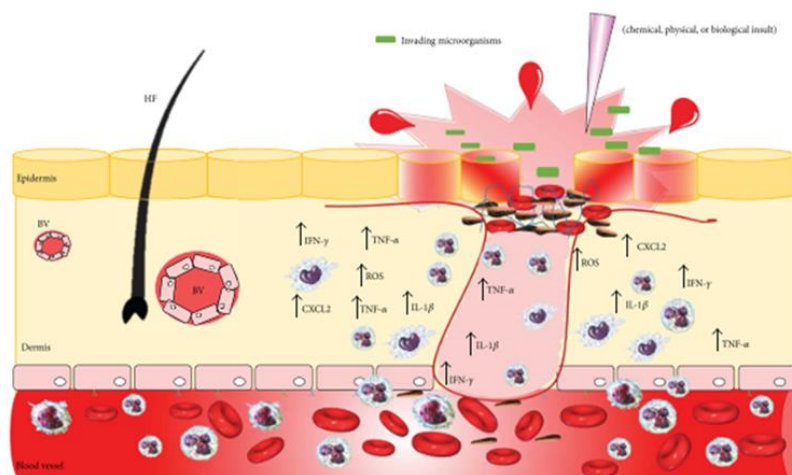
Figure 2-5 Image depicting the wound healing process, Adapted from Silva et al [107]

2.6.1 Homeostasis stage

Hemorrhage or bleeding is characteristic of any wound that penetrates the dermis. A natural occurrence that follows is the constriction of blood vessels thus restricting the flow of blood to the site of injury [108]. Platelets play a key role by adhering and aggregating at the injury site, by so doing sealing the break in the blood vessel. Fibrin clots, in the form of a mesh, are subsequently formed serving as a provisional matrix to keep the area moist and hydrated [109].

2.6.2 Inflammatory stage

This stage of the wound healing process is characterized by the release of cytokines and inflammatory mediators leading to inflammation. This results in and infiltration of the wound area by neutrophils from the blood [110]. Neutrophils are granulocytic polymorphonuclear cells that are also phagocytic. These cells digest bacteria, pathogens, and dead necrotic cells at the site of injury thereby, reduce the risk of infection. The neutrophils also release cytokines that attract a lot more of the neutrophils and macrophages [111].

2.6.3 Proliferation stage

Even before the end of the inflammatory stage, macrophages attracted to the site of injury release growth factors that stimulate cell proliferation. During this stage, fibroblasts migrate to the wound area as a result of the coordinating cytokine-growth factor releasing activity of macrophages [112]. Plasminogen, a soluble plasma protein, is converted to plasmin that digests and breaks up fibrin strands in a process referred to as

fibrinolysis. Fibroblasts also secrete collagen and matrix or ground substance, mostly

glycoproteins, that fill, contract and cover the wound area [113].

The wound bed is also filled with collagen fibers and growth factors that enhance

vascularization via angiogenesis to oxygenate the tissue. Proliferation of B lymphocytes

causes the infiltration of plasma cells that secrete antibodies (immunoglobin molecules)

for providing immunity. Adjacent cells increasingly proliferate, with the wound edges

contracting due to the activity of myofibroblasts (strips of fibroblasts) and components

that make up the granulation tissue [113], [114]. The latter phase of this proliferation

stage is characterized by migration of epithelial cells which rapidly form the epithelium

[115].

2.6.4 <u>Maturation phase</u>

This is the final stage of the wound healing process and is also referred to as remodeling

stage. Wounds can heal by regeneration or fibrosis. A suitably moist and hydrated wound

healing environment could heal via regeneration due to increased mitosis and cell

migration whereas an accumulation of more collagen-based fibrous tissue could result in

the formation of scar tissue [116]. During this remodeling stage of wound healing

vascularity of scars is seen to reduce over time, and re-arrangement of collagen is via

crosslinking is seen to occur resulting in a new tissue with less tensile strength compared

to unwounded skin [117].

2.7 Trends in wound management

Wound management is primarily focused on preventing scar tissue formation.

Complications could delay or prevent wound healing if the granulation tissue and re-

epithelization cells are kept relatively moist. Most complications have been attributed to

microbial infections. A typical wound management approach is polymeric wound dressings, gels, and dermal films [151]. The availability of current state-of-the-art technology means that the ideal wound care/management should encompass wound treatment using a wound dressing that prevents biofilm formation, prevents hypoxia, enhances balancing of the wound healing phases and incorporates cell therapy as well as nanocarrier systems for delivery of therapeutics.

2.8 Cells in Biomaterial Research

Biomaterials, mechanical stimuli, and cells are the major factors identified in tissue engineering [118]. Biomaterials engineered for tissue regenerative purposes should mimic the structural and biochemical support provided by the native extracellular matrix (ECM). The extracellular matrix (ECM) is composed of proteins and protein-polysaccharide complexes such as collagen, fibronectin, and proteoglycan complexes, that serve as cues and stimuli via their three-dimensional structure. Receptors in the cell plasma membrane react to materials in or on the body. As a result, cells can change functions based on the properties of the materials they are in contact with, hence the need to consider cells in biomaterial research. Cell types commonly used in biomedical research include mesenchymal stem cells (MSCs), induced pluripotent stem cells (iPSCs), embryonic stem cells (ESCs) and Schwann cells. These cells are mostly obtained from autologous, allogenic, and xenogeneic sources for use in conjunction with biomaterials for tissue engineering purposes.

Mesenchymal stem cells, also known as adult stem cells, are multipotential cells that together with hematopoietic stem cells provide the niche and progenitors for bone, cartilage, muscle, tendons, and fat. Studies have shown the feasibility of differentiating

MSCs into non mesenchymal cell lines including neural cells and epithelial cells. They are characterized by their non expression of surface markers such as CD45, CD34 and CD14, as well as the expression of CD166, CD105 and CD44 though these molecules are not exclusive to MSCs. However, common features of MSCs include plastic adhesion, morphology, and differentiation potential into cells with osteogenic, adipogenic and chondrogenic phenotypes. In addition to bone marrow, MSCs have been isolated and expanded from adipose tissue, umbilical cord, synovium, periosteum, teeth, lung and muscle. MSCs have found therapeutic applications in regenerative medicine, where they support the local repair of different tissue types. For this purpose, MScs are applied via direct loading to infarct zone for the treatment of myocardial infarction, to lung tissue for protection against bleomycin-induced lung injury, to the spinal cord for improvement in spinal function, and to joints for engraftment to meniscus, fat pad and synovium leading to protection of cartilage in an animal model of arthritis [119].

Induced pluripotent stem cells (iPSCs) are somatic cells genetically engineered into multipotent stem cells that possess the ability to differentiate into all cell types. They have found a variety of applications in regenerative since their discovery via transduction of regulatory genes in retroviruses and lentiviruses. More potent and recent methods for generating Induced pluripotent stem cells include synthesized RNAs [120], proteins [121] and plasmids [122]. Two major lines of Induced pluripotent stem cells (iPSCs) application have been reported in literature: directed differentiation into specific cell lineages or direct reprogramming [123]. Researchers have successfully differentiated iPSCs into cardiovascular cells [124], neural cells [125], and hepatocytes [126] via direct differentiation. For instance, Mauritz et al differentiated iPS cells in cardiomyocytes that

showed typical characteristics of this cell line including contracting embryoid bodies. The differentiated cells also expressed multiple marker genes typical of cardiomyocytes [127]. Similarly, the use of a neuron growth factor (NGF)-grafted poly(ε-caprolactone) (PCL)-poly(b-hydroxybutyrate) (PHB) scaffold was shown to enhance the differentiation of iPSCs into neurons by a group of researchers. This research work also showed that increased polymer concentration, while increased the adhesion of iPSCs likewise decreased the viability of the cells [125].

In summary, cells play a crucial role in the use of biomaterials for biomedical and tissue regeneration purposes. Mesenchymal stem cells and induced pluripotent stem cells are increasingly being studied for their cell-to-cell interactions as well as their cell-to-matrix (biomaterials and scaffold) interactions. They have the added advantage of being patient-specific thus, reducing the risk of immune suppression.

CHAPTER 3

METHODS

3.1   Project 1: Fabrication and characterization of Sol-Gel

Chitosan/Carboxymethylcellulose composite incorporated with zinc-doped

halloysites (HNTs) and characterization of its physico-chemical properties.

3.1.1   Overview

A carboxy-methylcellulose (CMC)/chitosan (CS)/HNT composite was prepared

via a simple solution-gel transition method, and its material properties and cellular effects

were investigated. Samples with different CMC/chitosan/HNT ratios were therefore,

fabricated. The microstructure of the dried composites was analyzed by Scanning

Electron Microscope (SEM). Molecular interactions between polymers were confirmed

by Fourier transform infrared (FTIR) spectra and thermal gravimetric analyze (TGA).

The swelling degree, weight loss, in vitro drug release behavior and antibacterial property

of the composites were also determined. Gentamicin (GEN) was used as a model

hydrophilic drug.

3.1.2   Materials

Chitosan (MW, deacetylation), carboxymethyl cellulose sodium salt (Lot #

SLCG5902), were purchased from sigma Aldrich (St. Louis, MO, USA). Halloysite

nanotubes were purchased from ALFA Chemistry (CAS # 1332-58-7, Lot #

A20D06061). Zinc oxide nanoparticles were purchased from Nanostructures &

Amorphous Materials Inc (CAS # 1314-13-2, Lot # 581-072011). Zinc sulphate was purchased from Eisen Golden laboratories (CAS # 7446-19-7, ID # EG ZNSO4-8).

3.1.3 Methods

Zinc-coating of Halloysites (HNTs)

Zinc and alloys of zinc have found wide application as prospective nanomaterials in diverse scientific fields. Zinc-coated HNTs were prepared based on an electrolytic method with the setup consisting of titanium meshes held parallel to each other at a distance of 2 inches and connected to a DC power input (VWR Accupower 500 electrophoresis power supply). An ultrasonicated 700 ml aqueous solution of 142 mg zinc oxide and 350 mg HNTs was poured in a beaker. Twenty volts (20V) was then be applied with switching of polarity at the platinum electrodes every 5 minutes under constant stirring. This was done to increase the accumulation of metal ions in the solution. The solution was allowed to settle, and the supernatant subsequently decanted after every round of washing in three repeats to remove non-adsorbed metal particles. This was followed by centrifugation at 5000 rpm for 5 minutes and drying at 37 ºC. The procedure is illustrated in Figure 3-1 below.
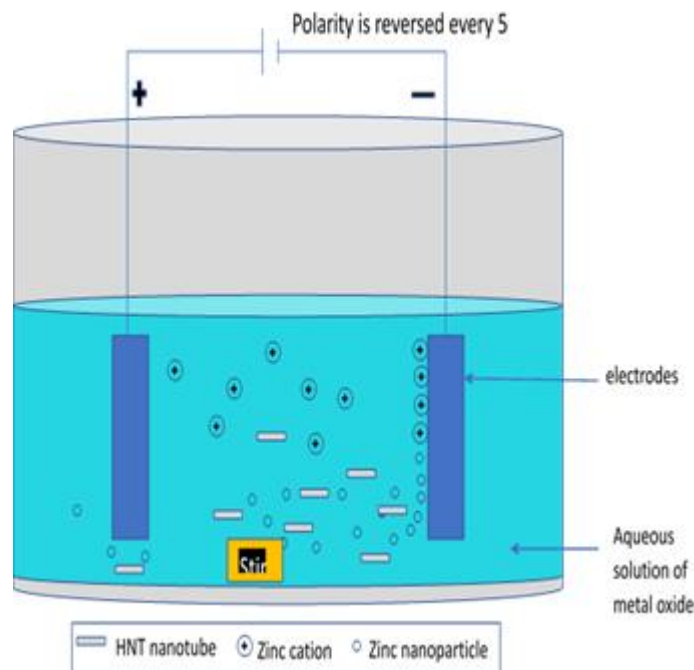
Figure 3-1 Schematic for doping halloysite nanotubes with metal nanoparticles via electrophoretic deposition

Characterization of HNTs and Zn-doped HNTs

SEM and EDS

  The surface topography of HNTs and zinc doped HNTS were analyzed on a S4800 Field Emission scanning electron microscope (Hitachi) under high vacuum. For improved resolution, samples were made more electrically conductive via sputter-coating with a thin layer of gold.

  Element analysis of HNTs and zinc doped HNTS was further carried out on an EDAX dispersive X-ray analyzer coupled to the scanning electron microscope using the following parameters: stage distance – 15mm, acceleration voltage – 20kV.

X-Ray Diffraction (XRD)

XRD pattern analysis was carried out on HNTS, ZnO and Zinc doped HNTS to study the crystal structure of the samples. This was done on a Bruker D8 Venture diffractometer (Brunker, Germany) under the following conditions: speed – 2 sec, step size – 0.02o. Patterns were detected on a Philips PW 1710 x-ray diffractometer over 2ϴ within 3° and 85°.

X-Ray Fluorescence (XRF)

Elemental analysis of zinc-doped halloysites in comparison to pristine halloysite nanotubes was conducted to confirm the electrophoretic deposition of zinc nanoparticles onto the surface of the halloysite nanotubes using x-ray fluorescence. The spectra obtained were analyzed on a Wintrace 7.1™ software (Thermo Fisher Scientific, Waltham, MA).

Fourier transform infrared spectroscopy (FT-IR)

Fourier transform infrared spectroscopy (FT-IR) spectra of HNTs, ZnO, $ZnSO_4$, ZnO-doped HNTs and $ZnSO_4$-doped HNTs were recorded on a FT-IR spectrometer in the range of 400–4000 cm−1 at a 6 cm−1 resolution and 32 scans using KBr pellets.

Loading of HNTs and ZnHNTs with gentamicin

Gentamicin sulphate (2mg) was loaded into HNTs (200 mg) and Zinc-coated (200 mg) HNTs by vacuum method. The samples were initially sterilized under UV light for 1 hour and then added to 10 ml of autoclaved ddH20. The suspension was placed in a vacuum chamber and subjected to 5 repeats of 75 cm Hg vacuum pressure for 20 minutes per cycle and released, with intermittent shaking. The gentamicin-loaded HNTs and zinc-

coated HNTs were allowed to settle, the supernatant was discarded, and the samples

washed with distilled water thrice to get rid of any excess gentamicin sulfate.

Test for minimal inhibitory concentration

The micro titration method was used to evaluate the minimal concentration of

anhydrous CS, CMC, HNT, ZnHNT and gentamicin loaded HNTs and Zn-doped HNTs

capable of inhibiting bacterial growth rate using the microtitration method. Equal

volumes of all the test materials (200 μl) at three different concentrations 2, 1 & 0.5

(mg/ml) were used in this study. Three clean colony cultures of gram-positive bacteria –

S. aureus and gram-negative bacteria – *E. coli* were chosen with bacterial growth rate

tests performed in 3 repeats. Bacteria was grown on Luria-Bertani (LB) broth, and the

test was conducted in Miller Hilton broth.

Fabrication – chitosan/carboxymethylcellulose composite

Chitosan/carboxymethylcellulose composites were prepared according to the

schematic in figure 3-2 below. In order to obtain the desired hydrogel, low molecular

weight chitosan was dissolved in 4% critic acid solution to form a 2% chitosan

concentration. For the purpose of this research work, 2% chitosan concentration is

deemed optimal as shown from our previous study Yangyang et al. [128].

Carboxymethylcellulose sodium salt (Sigma Aldrich) was also be obtained and dissolved

in distilled water to form a 2% CMC solution. Various volume-to-volume ratios of CTS

and CMS (1:8, 1:4, 1:1, 4:1, 8:1) were prepared by mixing the appropriate volumes of

each polymer solution. The resultant mixtures were then left at room temperature for

gelation to occur. After gelation, the hydrogels formed were washed in distilled water

and placed in dialysis tubes, and subsequently immersed in a large water container

overnight to equilibrate and get rid of residual unreacted organic solvents and chemicals.

This was followed by lyophilization of the composites via freeze-drying for further

analyses.
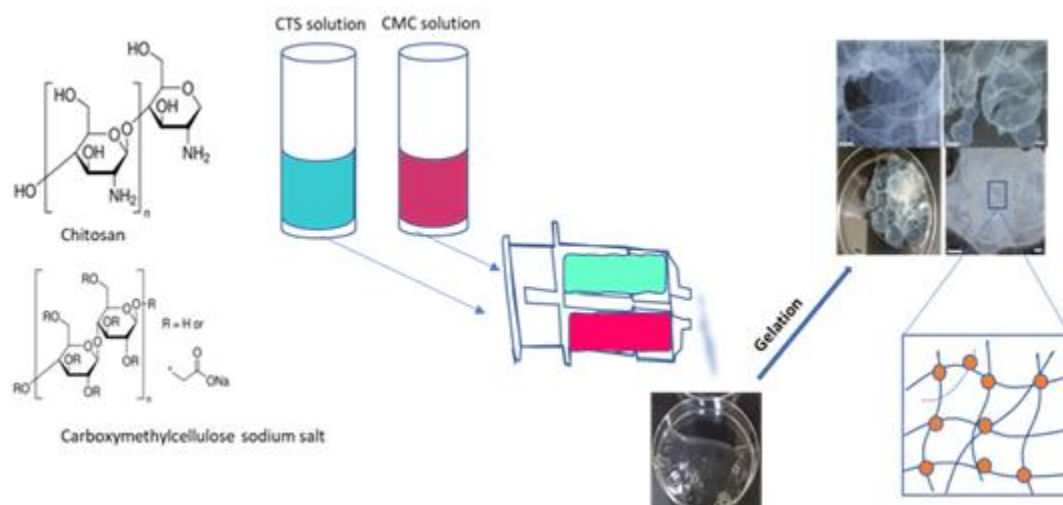
Figure 3-2 A schematic diagram depicting the fabrication process of CTS/CMC polymer
hydrogel.

Characterization of physico-chemical properties of fabricated composites

Rheological measurements

Assessment of the mechanical behavior of liquids using a rheometer is one way

to differentiate between viscous liquids and gels. Two main parameters, that is storage

modulus (G'), which is a measure of the stored energy representing the elastic portion,

and loss modulus (G"), which is a measure of the energy dissipated as heat, representing

the viscous portion, was recorded. These viscoelastic properties of the samples were

examined in the frequency range of $0.1–10 \text{ rs}^{-1}$. The chitosan to carboxymethyl ratio that

yielded a hydrogel with the optimal yield strength was used to fabricate groups of

lyophilized samples for further analyses. The experiment was run on a Bohlin C-VOR

rheological Instrument.

Spreadability test

A known mass of each CTS/CMC sample was placed on a glass slide and covered with a second glass. A fixed weight was placed on the construct for 2 minutes. Upon removal of the weight, contact angles of sessile drops of each chitosan-based sample were analyzed under a contact angle analyzer equipped with axis symmetric drop shape analysis profile as a qualitative measure of the ability of samples to spread.
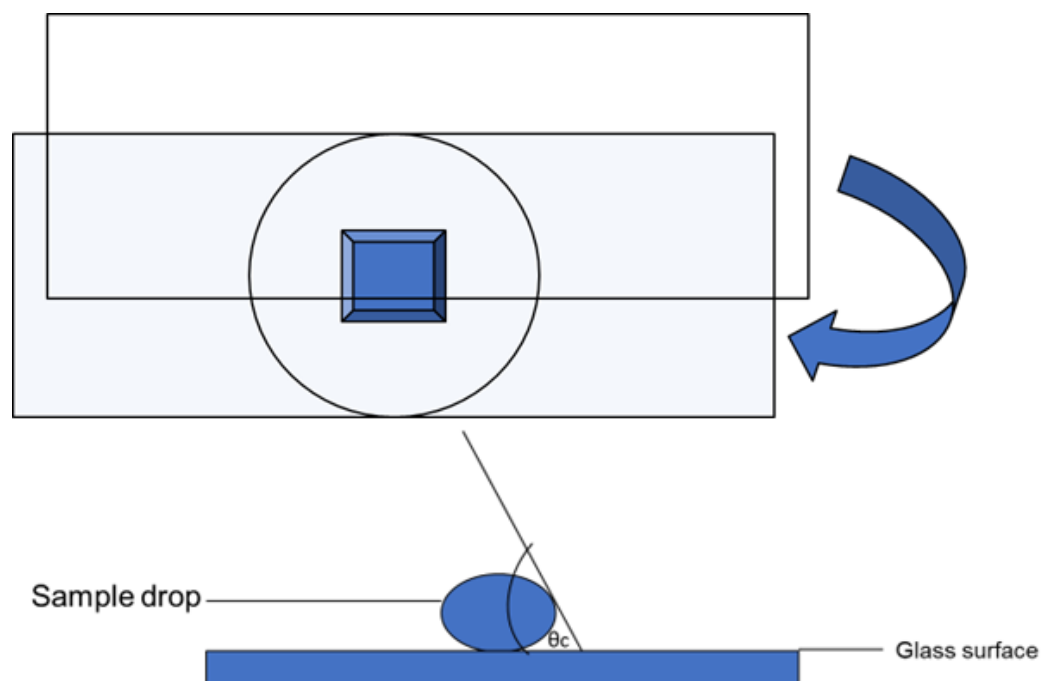
Figure 3-3 A schematic diagram depicting the process of assessing sample Spreadability.

Fourier-Transform Infrared (FT-IR) characterization

The structures of CTS, CMC, and lyophilized CTS/CMC composite were examined at room temperature on an FT-IR spectrometer (Spectrum 2000, Perkin Elmer Co, Norwalk, USA) using the potassium bromide (KBr) disc technique. An average of 16 scans with a resolution of 2 cm-1 was taken to confirm the intermolecular interaction of chitosan and carboxymethyl cellulose.

Assessment of polymer thermo-responsiveness via thermogravimetric analysis

Chitosan, carboxymethylcellulose, and the resultant lyophilized CTS/CMC composite were subjected to thermogravimetric analysis to assess their response to fluctuating temperature. This was carried out in an inert nitrogen atmosphere from 40 ºC to 600 ºC at a heating rate of 10 ºC per minute using a Q50 TGA system (TA Instruments, New Castle, Delaware, USA).

Scanning Electron Microscopy (SEM) Examination of Freeze-Dried Hydrogels

Hydrogels were frozen at 80 °C and then lyophilized by a freeze-dried method. The resulting dried samples were examined using an S4800 Field Emission SEM, HITACHI. The high magnification attained by SEM allowed for a close assessment of the surface morphologies of samples.

Energy Dispersive Spectroscopy (EDX)

EDAX dispersive X-ray analyzer attached to the HITACHI S-4800 SEM was used to evaluate the elemental composition and weight percentage of Zinc on the HNTs. EDS analyses were carried out at distance of 15mm with an acceleration voltage of 20kV and the spectra was analyzed using the EDAX Genesis software.

 Multi BET/Pore Size Testing

Determining the average pore size is a critical aspect for fabricating biomaterials. Microporous, microporous, and mesoporous biomaterials affect the permeability, surface area for cell attachment, and the mechanical strength of fabricated biomaterials. A MultiBET pore size analyzer (Brunauer-Emmett-Teller) was used to assess the differences in pore sizes of freeze-dried CTS/CMC composites fabricated at pH 2, pH 4 and pH 6. Analysis was done in the presence of helium gas at 60 °C outgas temperature

for 24 hours. Additionally, the samples: CTS/CMC, CTS/CMC+1%HNT and CTS/CMS+5% HNT were analyzed on the same equipment (NOVA 2200e surface area and pore analyzer) to assess the effect of halloysite nanoparticle addition on sample pore sizes.

Determination of Swelling Properties

The lyophilized chitosan-based samples were weighed (50 mg) and immersed in 25 mL of water. Samples were retrieved at pre-set time intervals and re-weighed to determine their swelling ratios and water content ratios using the formulae below:

$$Swelling\ ratio = \ Ms/Md$$

$$Water\ content, \% = \ ^{(Ms - Md)}/_{Ms} * 100\%$$

Where Ms is the mass of wet sample and Md is the mass of dry sample.

Statistical Analysis

The data obtained from these results will predominantly be qualitative. The data obtained was presented as mean ± standard error of the mean value (Mean ± SEM). The standard deviations between experimental groups were evaluated using one-way ANOVA (one-way ANOVA) followed by Bonferroni criteria of multiple comparison. The values were considered statistically valid at $p < 0.05$. The analysis was performed using excel statistical software pack.

3.2   Project 2: In vitro assessment of the effect of the fabricated chitosan-based composite on wound closure and cell migration

3.2.1   Overview

It is common that bleeding disorder and cut wound patients are treated with chitosan-based hemostatic composites. Wound healing involves a cascade of chemokine and cellular activity that leads to the regeneration of damaged tissue. With chitosan, halloysites and zinc nanoparticles being associated with different stages of the wound healing process [129]–[131], it is necessary to evaluate the combined effect of their interaction on cellular response in vitro by conducting antimicrobial tests, proliferation tests, cytotoxicity tests and cell migration tests including scratch assay and trans-well migration assay.

3.2.2   Materials

Dulbecco's Modified Eagle's Medium (DMEM), alpha Minimum Essential Medium (MEM α), penicillin-streptomycin sulphate, tryplE, and fetal bovine serum were used at various stages of the cell culture process. Human dermal fibroblast cell line, Adipose-derived mesenchymal stem cells, pre-osteoblast cells, and bacterial cell lines (*E. coli & S. aureus*) were purchased from ATCC.

3.2.3   Methods

Kirby Bauer Disk Susceptibility Test

E. coli (ATCC 25922) and *S. aureus* (ATCC 6538) were streaked on agar plates. Three similar colonies of the bacteria were identified and transferred with inoculation loops into 5ml of Tryptic Soy Broth. The broth cultures were incubated at 35 degrees C. to develop a turbidity equivalent to an absorbance of 0.08-0.1 at 630 nm which

corresponds to 1 to 2 x 108 CFU/ml. Lawns of these bacteria were then grown on Muller-Hilton agar plates via spreading of 100 μl of bacterial culture onto the plates using a spreader.

Chitosan-based samples, specifically CTS/CMC, CTS/CMC+1%HNT, CTC/CMC+2.5%HNT, CTS/CMC+5%HNT, CTC/CMC+1%LHNT, CTC/CMC+2.5LHNT, CTS/CMC+5%LHNT, CTS/CMC+1%ZnHNT, CTC/CMC+2.5%ZnHNT, CTS/CMC+5%ZnHNT, CTS/CMC+1%LZnHNT, CTC/CMC+2.5%LZnHNT and CTS/CMC+5%LZnHNT were made into discs similar to commercially available gentamicin controls discs (15mg weight, 6mm in diameter), and were impregnated on the Mueller-Hilton agar plates using aseptic precautions. The plates were incubated at 37 degrees celsius. After 18-24 hours of incubation, the plates were examined for zones showing inhibition via gross visual inspection, and the diameters of the zones of inhibition recorded.

Cell Culture

Human dermal fibroblasts and adipose-derived mesenchymal stem cells were purchased from ATCC and delivered in cryopreserved vials. The vials were thawed and brought to room temperature prior to use. Complete culture medium containing Dulbecco's modified Eagle medium (DMEM), 10% fetal bovine serum (FBS) and 1% penicillin/streptomycin antibiotic was prepared for supporting the growth of these cell lines at 37°C, 5% CO2. The DMEM used was obtained from GIBCO Invitrogen, the FBS was obtained from Neuromics, Cat No. FBS002, Lot No. N21H21 and penicillin/streptomycin was purchased from Gibco, REF. 15070-063. Additionally, mouse pre-osteoblast cell line (ATCC® CRL-2593™) (MC3T3) was purchased from

ATCC (Manassas, VA), thawed, and cultured in Alpha Minimum Essential Media (α -

MEM) supplemented with 10% FBS and 1% penicillin/streptomycin antibiotic. The cells

were cultured in a humidified incubator at 37°C, 5% CO2. After reaching a confluence

level of 80-90%, all cells were passaged by detaching with TryplE cell dissociation

medium. Passaging was carried out at 3000 * rcf for 3-5 minutes, followed by

resuspension of cells in appropriate amount of complete medium. All cells used for

experiments were at least passage 3 cells (P3) to ensure stability and viability. Cell

medium was changed every three days when cells were not confluent, unless stated

otherwise.

Sample conditioning

Chitosan-based samples were weighed (150 mg) and sterilized under UV light for

2 hours. The sterilized samples were then used to condition cell culture media by placing

them in 5 mL of complete DMEM at 4°C for 24 hours. The mixture was then centrifuged,

and the supernatant further diluted in 5 mL of a fresh complete medium.

Cell Proliferation assay

A suspension of cells in pre-conditioned media was made and seeded into wells of

a 96-well plate at a density of 1000 cells/well. The cell culture plates were then pre-

incubated in a humidified incubator at 37°C, 5% CO2. CCK-8 reagent was thawed in a

water bath at 37°C, 10 μl of it was added to each well of the plate and incubated for 2

hours in the incubator. At given times, the absorbance was measured at 450 nm using a

microplate reader (BioTek Instruments, Inc., REF 800TS). The proliferation assay was

conducted on day 1, 2, 3, 4, and 5.

Cytotoxicity Testing

The cytotoxicity of chitosan-based composites was analyzed via live/dead assay using human dermal fibroblast cells. Dulbecco's Modified Eagle's Medium supplemented with 10% fetal bovine serum and 1% penicillin/streptomycin was pre-conditioned via the method described above. The human dermal fibroblast cells were seeded in 500 µL of the pre-conditioned media at a density of 1000 cells/well on 48 well plates and cultured at 37°C, 5% CO2. Additionally, a staining solution containing 5 µL of 4mM Calcein, 20 µL of 2mM EthD, and 10 mL PBS was prepared. On given days 1, 3 and 5, the culture medium was aspirated, the cells were washed three times with phosphate buffered saline (PBS) and stained in 200 µL of the staining medium. This was followed by a 30–45-minute incubation at room temperature. Fluorescence images were taken on ECHO microscope with live and dead cells counted using Image J software.

Alizarin Red Staining

Alizarin red staining and quantification assay (ScienCell Research Laboratories Cat. #8678) was used to assess matrix mineralization via evaluation of calcium deposits in cell culture post-osteogenic differentiation. Cells were cultured in appropriate sample-conditioned cell media for different time periods (1, 7 and 14 days) and subsequently fixed using 4% formaldehyde for 15 min at room temperature. The cells were then stained with 1 mL of 40mM alizarin red stain for 30 min with gentle shaking, washed 5 times with deionized water and observed under a microscope. A monolayer of cells cultured pristine culture medium served as control cell group. The alizarin dye was extracted and quantified on a plate reader (BioTek Instruments, Inc., REF 800TS) at 405

nm to calculate the staining concentration by comparing it to optical density readings of alizarin red staining standards of known concentrations.

Dye Extraction

Plates containing cells stained with alizarin red dye were tilted at an angle for 2 mins to remove excess water from them. They were then stored overnight at -20°C prior to dye extraction. Acetic acid (10%) was added to wells of a 24-well plate containing stained cells in a volume of 200 µL/ well. The plates were then incubated for 30 minutes at room temperature with gentle shaking. The cells were detached into the acetic acid solution using a cell scraper, collected into 1.5 mL Eppendorf tubes., and vortexed for 30 seconds. This was followed by sample heating at 85°C for 10 minutes and 5 minutes incubation on ice. Subsequent steps involved centrifugation of the slurry at 20,000 g for 15 minutes, transferring 200 µL of the supernatant to new 1.5 mL Eppendorf tubes and increasing the pH of the solution to between 4.1 and 4.5 using 75 µL of 10% ammonium hydroxide. Fifty (50 µL/well) microliters of each sample were aliquoted into wells of a 96-well plate in triplicates, and the absorbance reading was taken at 405 nm on a plate reader (BioTek Instruments, Inc., REF 800TS).

Standard Preparation

Alizarin red stain (ARS) was added to a standard dilution solution in volumes of 100 µL and 900 µL respectively in a 1.5 mL Eppendorf tube. Next, microcentrifuge tubes were labeled #1 through #8, with 500 µL/tube of standard dilution solution added to them. 500 µL of the first mix was added to tube #1 and then serially diluted through #7. Tube #8 served as a control tube (blank). Absorbance readings were then taken at 405 nm using a plate reader (BioTek Instruments, Inc., REF 800TS).

S-β-Galactosidase Staining

A senescence cell histochemical staining kit (Sigma-Aldrich Cat. #CS0030-1KT) was used to assess the expression of β-galactosidase according to the manufacturer's protocol. Pre-osteoblast cells were grown in the presence of conditioned samples and fixed in 1X fixation buffer at room temperature for 6-7 minutes, followed by the addition of the staining mixture to stain the cells, incubated at 37°C overnight. The ratio of blue-stained cells was used to calculate the senescent cells (the percentage of cells expressing β-galactosidase).

Scratch assay

A scratch assay protocol was designed to measure cell migration in vitro after exposure of human dermal fibroblasts to chitosan-based composites in comparison with control unexposed cells. Confluent fibroblasts were detached from cell culture flasks, resuspended in DMEM supplemented with 10% fetal bovine serum and 1% penicillin/streptomycin, and plated on 48 well cell culture plates at a density of 1000 cells/well. The plates were kept at 37 ºC, 5% CO_2 until confluent. Once confluent, the cell monolayers were scraped in a straight line in each group with a p20 pipet tip. The debris was removed via washing with 1 ml of complete growth medium. Two (2) milliliters of fresh growth medium were added to the control group and the experimental group of cells contained 2 ml of media pre-conditioned with the appropriate chitosan-based composites supplemented with 10% fetal bovine serum and 1% penicillin/streptomycin. Phase contrast images were taken at given time periods (0-12 hours).
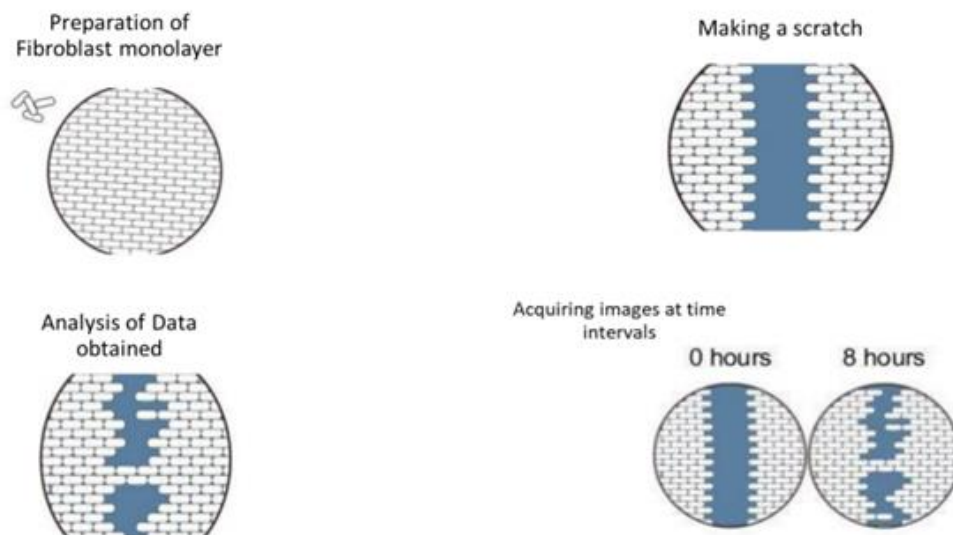
Figure 3-4 Schematic of scratch wound assay

3.3   Project 3: Biofabrication and material characterization of Chitosan/Carboxymethyl cellulose solution casted membranes for various biomedical applications.

3.3.1   Overview

Over the years, polymer composites are increasingly being researched for their ability to supplement or replace conventional materials. Section 3.1 of this dissertation research was focused on synthesizing CTS/CMC composites reinforced with halloysites and zinc-doped halloysites via solution-gel synthesis method. Inconclusive results were obtained with regards to possible zinc toxicity to mesenchymal stem cells and human dermal fibroblast cells. This was suggested and attributed to the CTS/CMC fabrication method, which involved the dissolution of chitosan in an acidic environment as well as the undesirable cellular response to zinc (zinc toxicity) arising due to its concentration or

the buffer conditions (pH) of the cell culture media as reported by other studies [132]–[135].

Chitosan/carboxymethyl cellulose composites reinforced with halloysites and copper-doped halloysites were therefore, fabricated via solvent casting method and investigated for their mechanical, chemical, and morphological properties as well as in vitro cellular response.

3.3.2　Materials

Water-soluble chitosan was purchased from Matexcel (10-30mpa.s, cat. # NAT-0033), carboxymethyl cellulose sodium salt was purchased Sigma Aldrich (St. Louis, MO, USA), while halloysite nanotubes were purchased from ALFA Chemistry (CAS # 1332-58-7). Copper oxide (CuO) nanoparticles were also purchased from Alpha Chemicals. Additionally, Dulbecco's Modified Eagle's Medium (DMEM), penicillin-streptomycin sulphate, tryplE, and fetal bovine serum were used at various stages of the cell culture process. Human dermal fibroblast cell line, Adipose-derived mesenchymal stem cells, and bacterial cell lines (*E. coli* & *S. aureus*) were purchased from ATCC.

3.3.3　Methods

Copper-coating of Halloysites (HNTs)

In a process similar to the coating of halloysites with zinc, copper nanoparticles were attached to the surface of HNTs via electrodeposition. An ultrasonicated 700 ml aqueous solution of 139 mg copper (II) oxide and 350 mg HNTs was poured in a beaker. Twenty volts (20V) was then be applied with switching of polarity at the platinum electrodes every 5 minutes under constant stirring. This was done to increase the accumulation of copper ions in the solution. The solution was allowed to settle, and the

supernatant subsequently decanted after every round of washing in three repeats to remove non-adsorbed copper nanoparticles. This was followed by centrifugation at 5000 rpm for 5 minutes and drying at 37 °C.

SEM and EDS

Similar to the SEM and EDS processes in section 3.1.3. the surface topography of copper doped HNTs sputter-coated with a thin layer of gold were analyzed on a S4800 Field Emission scanning electron microscope (Hitachi) under high vacuum. Element analysis of the sample was further carried out on an EDS dispersive X-ray analyzer attached to the scanning electron microscope using the following parameters: stage distance – 15mm, acceleration voltage – 20kV.

X-Ray Diffraction (XRD)

XRD pattern analysis of pristine halloysites, copper oxide and copper-doped halloysites was carried to study the crystal structure of the samples using a Bruker D8 Venture diffractometer (Brunker, Germany) under the following conditions: speed – 2 sec, step size – 0.02°. Patterns were detected on a Philips PW 1710 x-ray diffractometer over 2Ө within 3° and 85°.

Fourier transform infrared spectroscopy (FT-IR)

Fourier transform infrared spectroscopy (FT-IR) spectra of HNTs, CuO and CuO-doped HNTs were recorded on a FT-IR spectrometer in the range of 400–4000 cm−1 at a 6 cm−1 resolution and 32 scans using KBr pellets.

Loading of HNTs and CuOHNTs with gentamicin

Gentamicin sulphate (2mg) was loaded into HNTs (200 mg) and copper doped (200 mg) HNTs by vacuum method. The samples were initially sterilized under UV light

for 1 hour and then added to 10 ml of autoclaved ddH20. The suspension was placed in a

vacuum chamber and subjected to 5 repeats of 75 cm Hg vacuum pressure for 20 minutes

per cycle and released, with intermittent shaking. The gentamicin-loaded HNTs and

copper-coated HNTs were allowed to settle, the supernatant was discarded, and the

samples washed with distilled water thrice to get rid of any excess gentamicin sulfate.

Fabrication of chitosan-based membranes

The solution casting/solvent casting approach was adopted from Kavitha et al

with some modifications [136]. Water-soluble chitosan (4g) was dissolved in 400 ml of

distilled water by stirring at 500 rpm to obtain a 1% chitosan solution. Similarly,

carboxymethyl cellulose (4 g) was also dissolved in 500 ml distilled water to obtain a 1%

CMC solution. CTS/CMC solutions were prepared by mixing 20 ml of the 1% CTS

solution with 40 ml of the 1% CMC solution. CTS/CMC+1% HNT, CTS/CMC+5%HNT,

CTS/CMC+1% CuHNT and CTS/CMC+5% CuHNT samples were made by

incorporating the appropriate amounts of HNT and CuHNT (w/v) and mixing the

components together by stirring at 1000 rpm for 1hour. The mixtures were subsequently

poured into plastic petri dishes and dried at 40 °C overnight.

Characterization of membranes by FT-IR

Post-fabrication, the chitosan-based membranes were subjected to transmission

FT-IR analysis to the interactions occurring between the constituent components,

specifically, chitosan, carboxymethyl cellulose, CTS/CMC and halloysites using a

Mattson Genesis II FTIR spectrometer.

Scanning Electron Microscopy (SEM)

The pure chitosan/carboxymethyl cellulose film membranes as well as membranes reinforced with HNTS and copper oxide HNTs were examined for their surface structure using an S4800 Field Emission SEM, HITACHI. The high magnification attained by SEM allowed for a close assessment of the surface morphologies of the samples.

Themo-gravimetric analysis

Similar to the thermo-gravimetric procedures carried out in the previous section, the fabricated CTS-based film membranes were assessed for their response to temperature. This was done via thermos-gravimetric analysis in an inert nitrogen atmosphere from 40 ºC to 600 ºC at a heating rate of 10 ºC per minute using a Q50 TGA system (TA Instruments, New Castle, Delaware, USA). To study the weight gain or loss properties of the samples with increasing temperature, an empty pan was placed on a high precision scale and zeroed to serve as standard. The samples were then simultaneously place in a pan and placed on the scale and then run on the Q50 TGA equipment until a temperature of 600 ºC was reached.

Tensile strength measurement

The fabricated CTS-based membranes were subjected to a pulling force (2000 N) at a displacement rate of 0.2 mm per second using a tensile strength analyzer (Cellscale biomaterial testing, USA). All samples were analyzed in 3 repeats and the results averaged. From the data obtained, a stress displacement-curve was generated, and the tensile strength of each film was determined as the stress at the break point.

Kirby Bauer Disk Susceptibility Test

The fabricated film membranes were tested for their antimicrobial properties against *E. coli* and *S. aureus* using the Kirby Bauer Disk Susceptibility test as described above in Kirby Bauer Disk Susceptibility Test procedure explained in previous section.

Sample conditioning

Chitosan-based film membranes were sterilized under UV light for 2 hours and then used to condition cell culture media by placing them in 5 mL of complete DMEM at 4°C for 24 hours. The mixture was then centrifuged, and the supernatant further diluted in 5 mL of a fresh complete medium.

Cell Proliferation assay

Similar to the Cell Proliferation assay procedure in the previous section, a suspension of cells in pre-conditioned media was made and aliquoted into wells of a 96-well plate at a density of 1000 cells/well. This was followed by pre-incubation of the plates containing the cells in a humidified incubator at 37 ° C, 5% CO_2. CCK-8 reagent was thawed in a water bath at 37°C, 10 μl of it was added to each well of the plate and incubated for 2 hours in the incubator. At given times, the absorbance was measured at 450 nm using a microplate reader (BioTek Instruments, Inc., REF 800TS). The proliferation assay was conducted on day 1, 2, 3, 4, and 5.

Cytotoxicity test (live/dead assay)

The biocompatibility of the chitosan-based film membranes was assessed using a Biotium cytotoxicity/viability assay for animal cells (cat# 30002) on days 3, 5 and 7. Calcein and EthD dyes were prepared according to the manufacturer's protocol and added to cells in a 24-well plate exposed to the different chitosan-based film membranes.

Medium conditioning was done by sterilizing equal masses of the thin film membranes under ultraviolet light and adding them to 50 ml of DMEM supplemented with 10% FBS and 1% penicillin/streptomycin (complete medium). The cell culture media were then incubated for 24 hours at 4 degrees Celsius followed by centrifugation to precipitate the debris. The supernatant was then collected into fresh 50 ml Eppendorf tubes and used for subsequent cell culturing. The control group of fibroblasts were cultured in pristine complete medium.

CHAPTER 4

RESULTS

4.1   Project 1: Fabrication and characterization of Sol-Gel

Chitosan/Carboxymethylcellulose composite incorporated with zinc-doped

halloysites (HNTs) and characterization of its physico-chemical properties.

4.1.1   Evaluation of halloysite coating with zinc oxide nanoparticles

SEM and EDX

Zinc metal nanoparticle adsorption on the surface of halloysites is explained by applied voltage likely driving the cathodic reduction of Zn^{2+} to $Zn^{2+}NPs$, thus making the nanoparticles available for deposition on the surface of the halloysite nanotubes present in solution. Deposition of Zn Nanoparticles of HNTs was confirmed by SEM image analysis. Plain HNTs served as control.
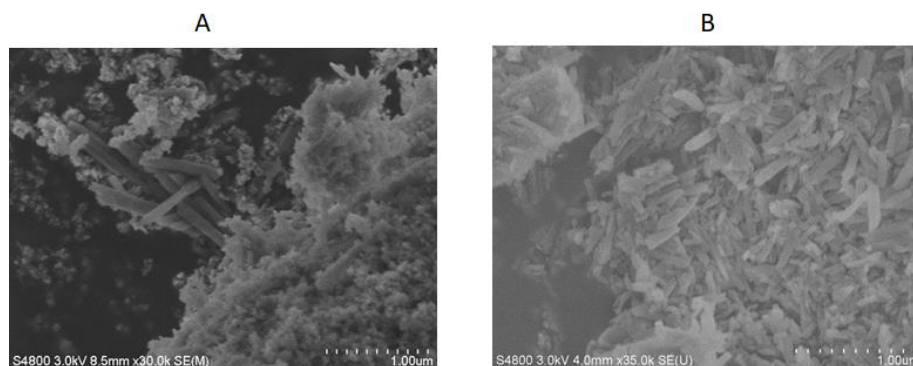
Figure 4-1 SEM images of A. Plain HNTs and B. Zn-coated HNTs.

The occurrence of halloysites as small cylindrical or rod-like structure is shown in the above figures 4 A and B. In figure 4A HNTs are seen to have a plain and smooth surface topography, whereas in 4B their appearance in seen to differ with the occurrence of tiny clusters and granules suggesting the successful deposition of metal nanoparticles.
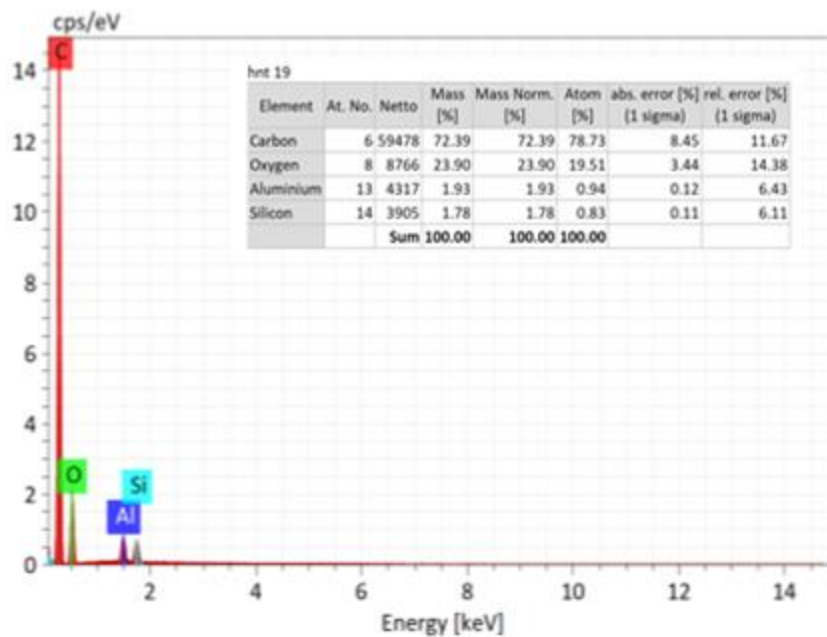
Figure 4-2 The quantitative elemental analysis of pristine HNT showing the wt% of carbon [C], aluminum [Al], silicon [Si], oxygen [O]
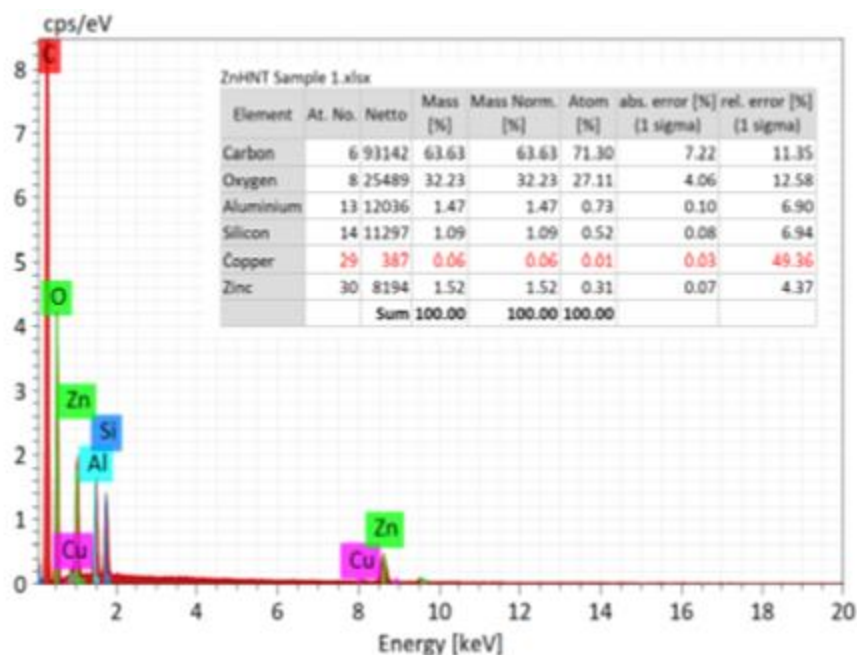
Figure 4-3 The quantitative elemental analysis of zinc doped HNTS, showing the wt% of carbon [C], aluminum [Al], silicon [Si], oxygen [O] and Zinc [Zn].

In figure 4-2 above, the elemental analysis of pristine halloysites showed the presence of the expected elements, specifically carbon, oxygen, aluminum, and silicon, whereas Figure 4-3 showed the presence of zinc in addition to the above-mentioned elements. As seen from the EDS of the zinc-doped HNT sample, a defined peak attributed to zinc is seen wth a corresponding percentage mass of 1.52, thus confirmimg the success of the electrodeposition method.

FT-IR Analysis

The transmission FT-IR spectrum of HNT showed characteristic bands at 748, 903, 1000, 3620 and 3690 cm^{-1}. These bands are assigned to Si-O stretching vibrations, vibrations of inner hydroxyl groups (O-H), in-plane Si-O stretching, inner groups vibrations and inner surface O-H group stretching respectively. FTIR determination of functional groups of ZnO NPs in figure showed a characteristic broad absorption peak

withing the range of 400 - 500 cm^{-1} which is attributed to Zn-O stretching vibration. The additional peak 3417 cm^{-1} is attributed to hydroxyl group stretching. FTIR analysis of the ZnO-doped HNT samples showed characteristic band absorptions attributed to Zn-O stretching as well as peaks specific to components of halloysite nanotubes. Absorption bands of various functional groups characteristic to $ZnSO_4$ were also observed at the range of 400 – 4000 cm^{-1}. A broad absorption band representing stretching water vibration was visible at approximately 3000 -3700 cm^{-1} in accordance with literature [137] with an additional medium band at approximately 1616 cm-1 attributed to bending vibration of water molecules. Fundamental vibrations of free $SO4^{2-}$ were observed at 613, 981 and 1104 cm-1. FTIR analysis of ZnSO4-doped HNTs exhibited absorption bands specific to ZnSO4 as well as peaks characteristic of HNTs (Jewel-BJAS). Additionally, figure shows the interpretation of FTIR data confirming that the test sample is composed of Kaolin clays/alumina-silicates.
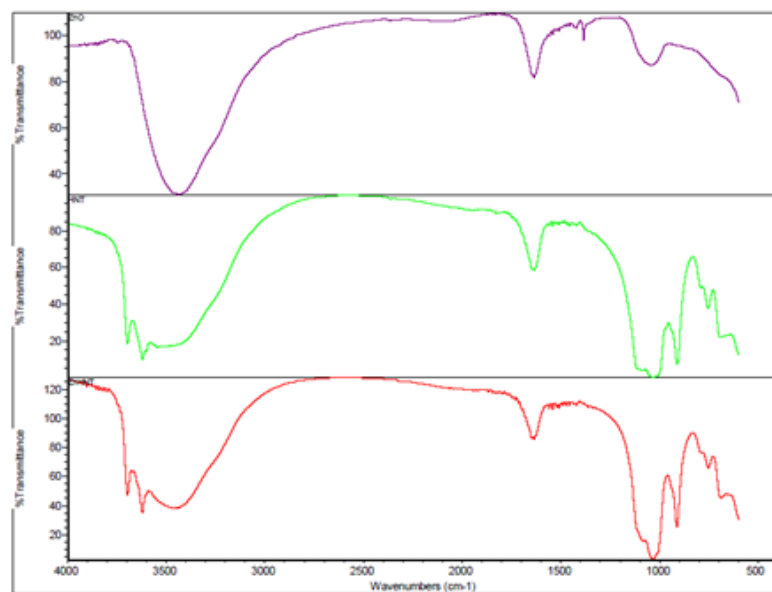
Figure 4-4 Transmission FTIR analysis of HNTs, ZnO and ZnO-doped HNTs displaying the characteristic FTIR absorption bands.
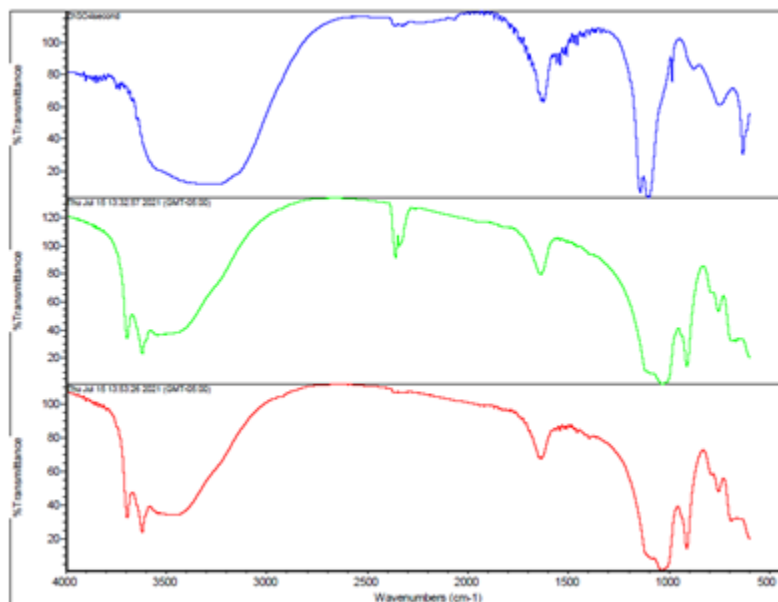
Figure 4-5 Transmission FTIR analysis of HNTs, ZnSO4 and ZnSO4-doped HNTs displaying the characteristic FTIR absorption bands.
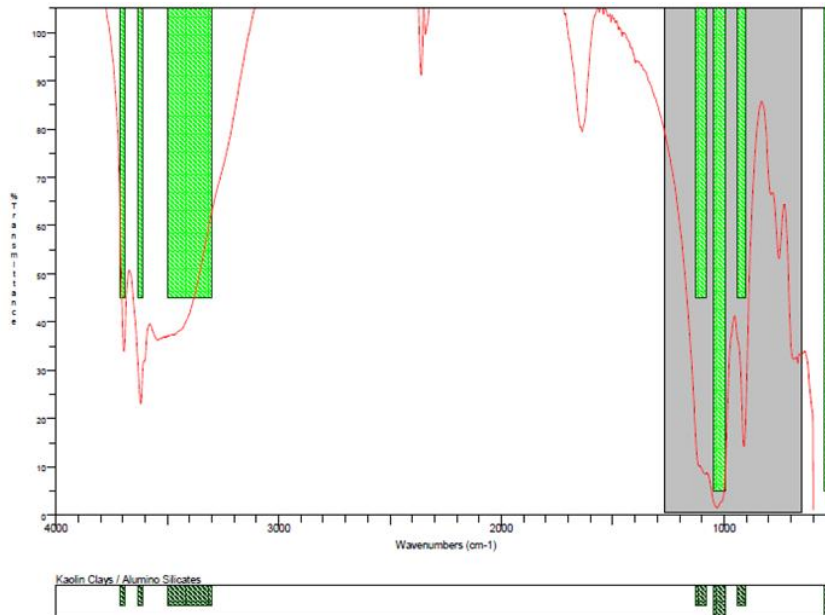
Figure 4-6 Interpretation HNT peaks

X-ray Fluorescence (XRF) was used to further confirm the presence of Zn and the successful coating of HNTs with Zn respectively. The result is shown in Figure 4-7 below.
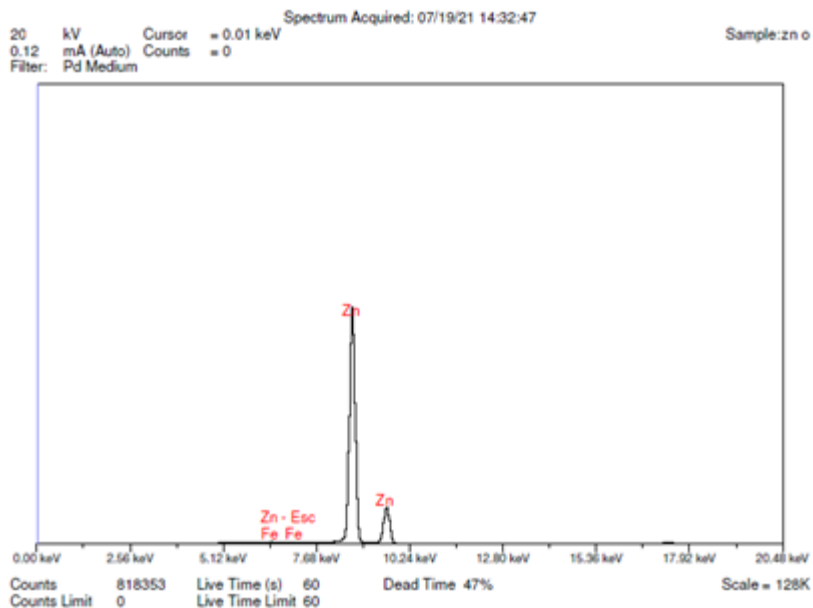
Figure 4-7 XRF analysis of samples showing peaks attributed to zinc.

Results of the XRF study showed a very intense peak for Zn, suggesting the presence of Zn in the ZnO-coated HNT sample after several wash steps.

XRD

With respect to XRD patterns attributed to HNT, secondary peaks are detected in Figure 6 at 2 theta angle of approximately 22º and 26.27º suggestive of phases such as cristobalite and quartz. Distinct peaks were detected at 2 theta angles of 12.12º, 20.08º, 24.59º and 35º, characteristic of some HNT lattice points: 001, 110 and 002. Sharp diffraction peaks were seen for ZnO suggesting the good crystallinity of the nanoparticles. There were distinct peaks characteristic of ZnO at 2 theta angles of 31.8 (100), 34.5 (002) and 36.33 (101). The XRD pattern for zinc doped HNT showed subdued peaks of HNT likely due to the presence of zinc nanoparticles on the surface of the halloysite nanotubes.
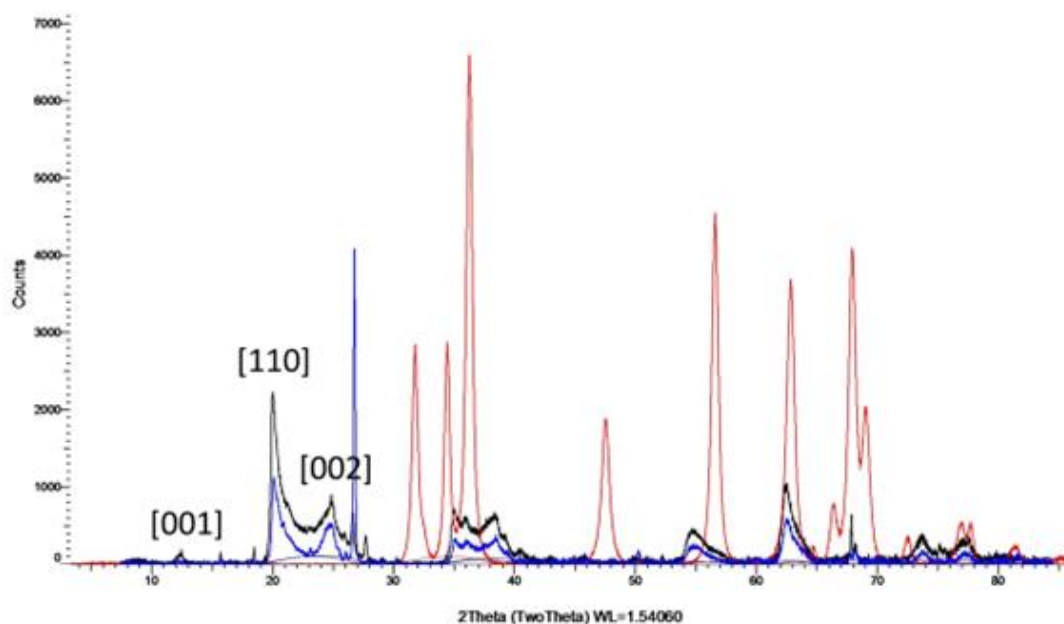
Figure 4-8 XRD graph image of HNT (black), ZnO (red)and Zn doped HNT (blue).

Minimum Inhibitory concentration

E. coli

The micro titration test results showed that 2 mg/µl, 1 mg/µl and 0.5 mg/µl concentrations of all the test sample stagnated *E. coli* growth in culture medium for up to 36 hours in comparison to the negative control sample (untreated *E. coli* bacterial culture) and the positive control sample (*E. coli* cultured in medium containing 2, 1 & 0.5 mg/µl gentamicin sulfate) as seen in figure. Zn-doped HNT loaded with gentamicin sulphate showed bacterial growth inhibition properties similar to the positive control sample at all three concentrations.
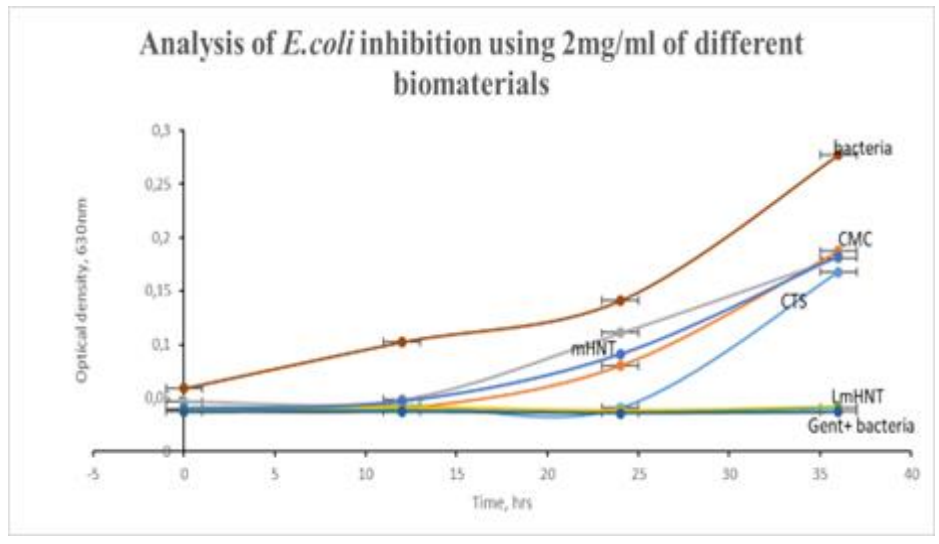
Figure 4-9 Graph depicting the inhibitory effect of 2 mg test samples against *E. coli* growth. N=3
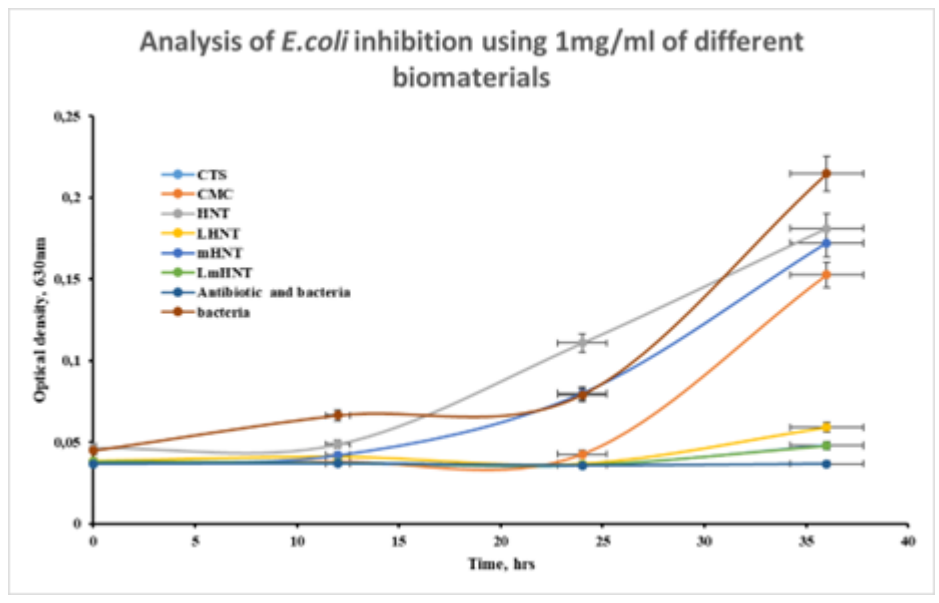
Figure 4-10 Graph depicting the inhibitory effect of 1 mg test samples against *E. coli* growth. N=3
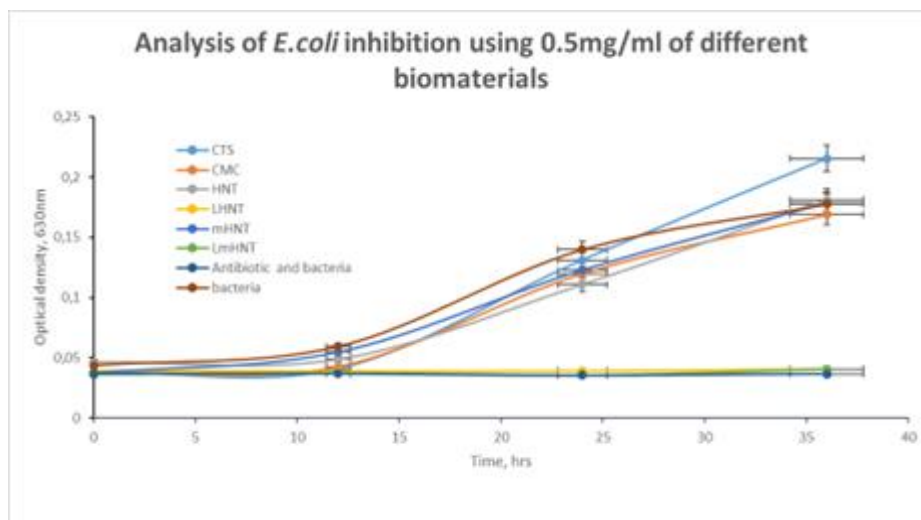
Figure 4-11 Graph depicting the inhibitory effect of 0.5 mg test samples against *E. coli* growth. N=3

S. aureus

Similar to results of the test carried out using *E.coli*, the micro titration test results using *S.aureus* showed that 2 mg/µl, 1 mg/µl and 0.5 mg/µl concentrations of all the test sample stagnated *S.aureus* bacterial growth in culture medium for up to 36 hours in comparison to the negative control sample (untreated *S.aureus* bacterial culture) and the positive control sample (*S.aureus* bacteria cultured in medium containing 2, 1 & 0.5 mg/µl gentamicin sulfate) as seen in figure. Zn-doped HNT loaded with gentamicin sulphate showed bacterial growth inhibition properties similar to the positive control sample at all three concentrations.
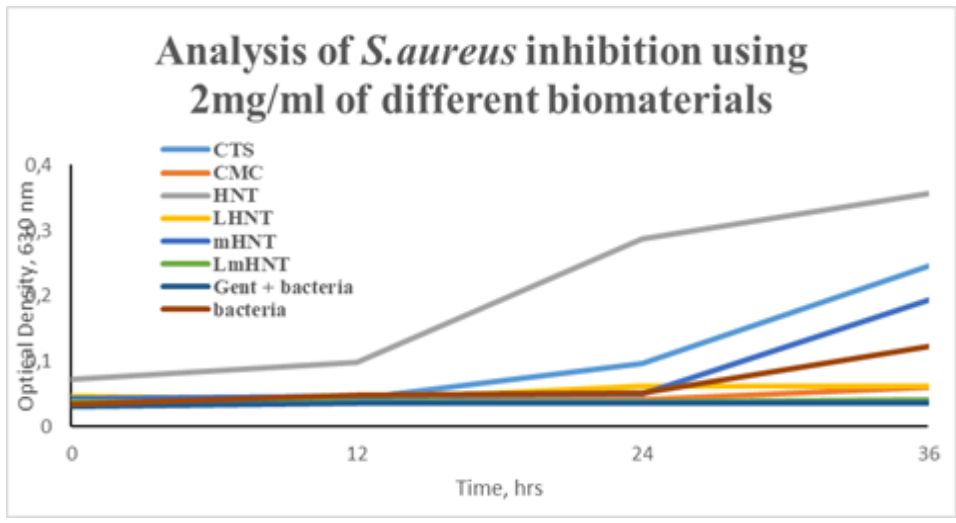
Figure 4-12 Graph depicting the inhibitory effect of 2 mg/ml test samples against *S. aureus* growth.
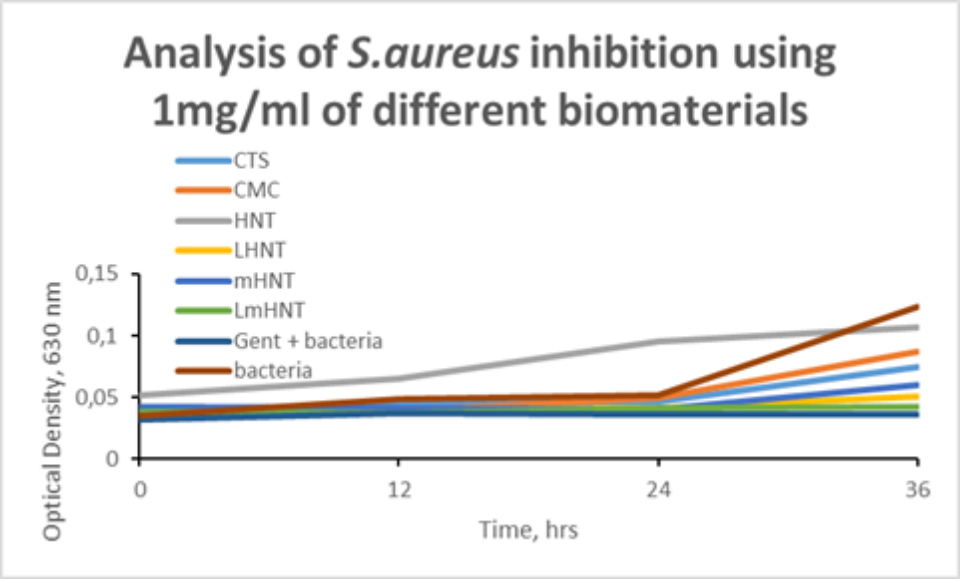
Figure 4-13 Graph depicting the inhibitory effect of 1 mg/ml test samples against *S. aureus* growth.
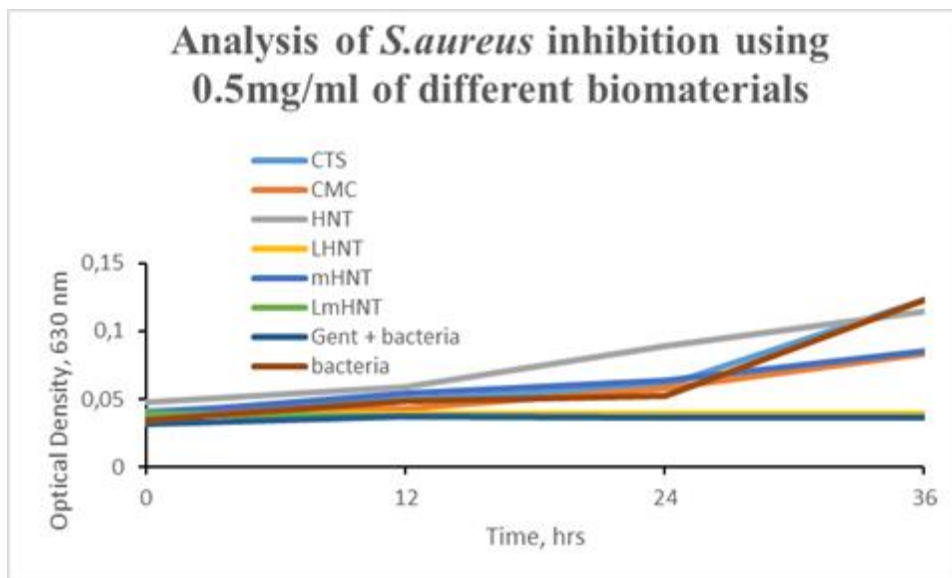
Figure 4-14 Graph depicting the inhibitory effect of 0.5 mg/ml test samples against *S. aureus* growth.

4.1.2   Fabrication and characterization of chitosan/carboxymethylcellulose

conjugate

VHX microscopy

Electrostatic interactions between the cationic amine groups of chitosan and the

anionic carboxyl groups of carboxymethyl cellulose resulted in a hydrogel as seen in

Figure 4-15 at magnifications of 20 X, 40X and 80X with resolutions of 2000 μm, 1000

um and 500 μm respectively.
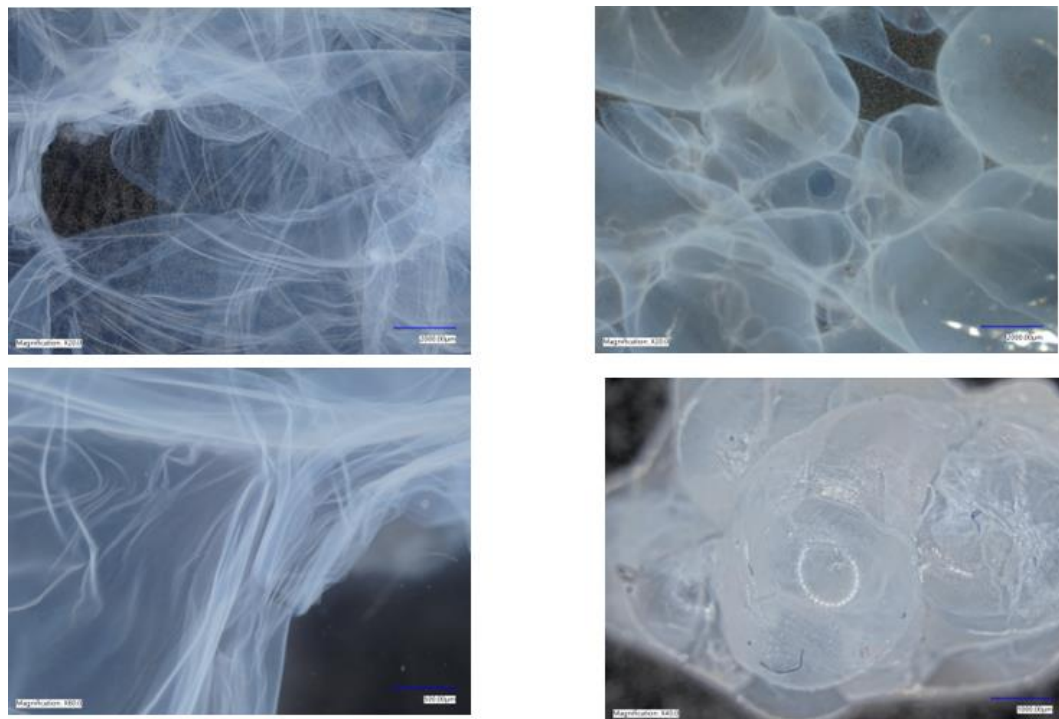
Figure 4-15 VHX Microscopy images of fabricated hydrogel.

Gelation was seen to occur within 5 minutes of mixing Chitosan with carboxymethylcellulose at a volume-to-volume ratio of 1:1.

Rheological studies

The rheological properties of the various volume-to-volume ratios of CTS and CMS (1:8, 1:4, 1:1, 4:1, 8:1) were examined by using an oscillatory shear force applied to the samples. This is one way to differentiate between a gel and a highly viscous liquid. Initial amplitude sweep tests were carried out at a fixed frequency of 1Hz followed by frequency sweep tests at room temperature. Results of the amplitude sweep test for the various volume-to-volume ratio CTS/CMS hydrogels are presented below in the graphs below (figure 4-16), with strain plotted on the x-axis and elastic modulus on the y-axis. This was done to determine the linear viscoelastic region that represents the safe range

for carrying out the rheological tests without causing damage to the structure of the

hydrogels. This optimal strain value was determined to be 0.01 for all the hydrogel

variants.
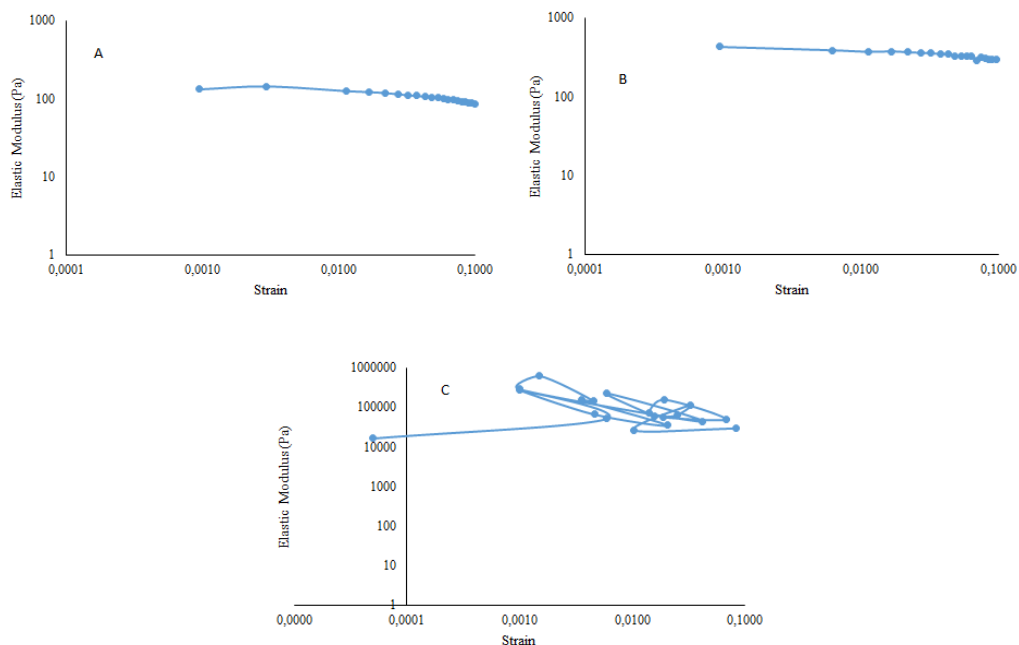
Figure 4-16 Variation of Elastic Modulus profile with shear strain at a) 1 Hz b) 10 Hz c) 100 Hz for 1:1 volume-to-volume CTS/CMC blend.

The results expressed as graphs below in Figure 4-17 below show the frequency

sweep experiments that were carried out using the different volume-to-volume ratios of

CTS and CMS (1:8, 1:4, 1:1, 4:1, 8:1) at a strain of 0.01.
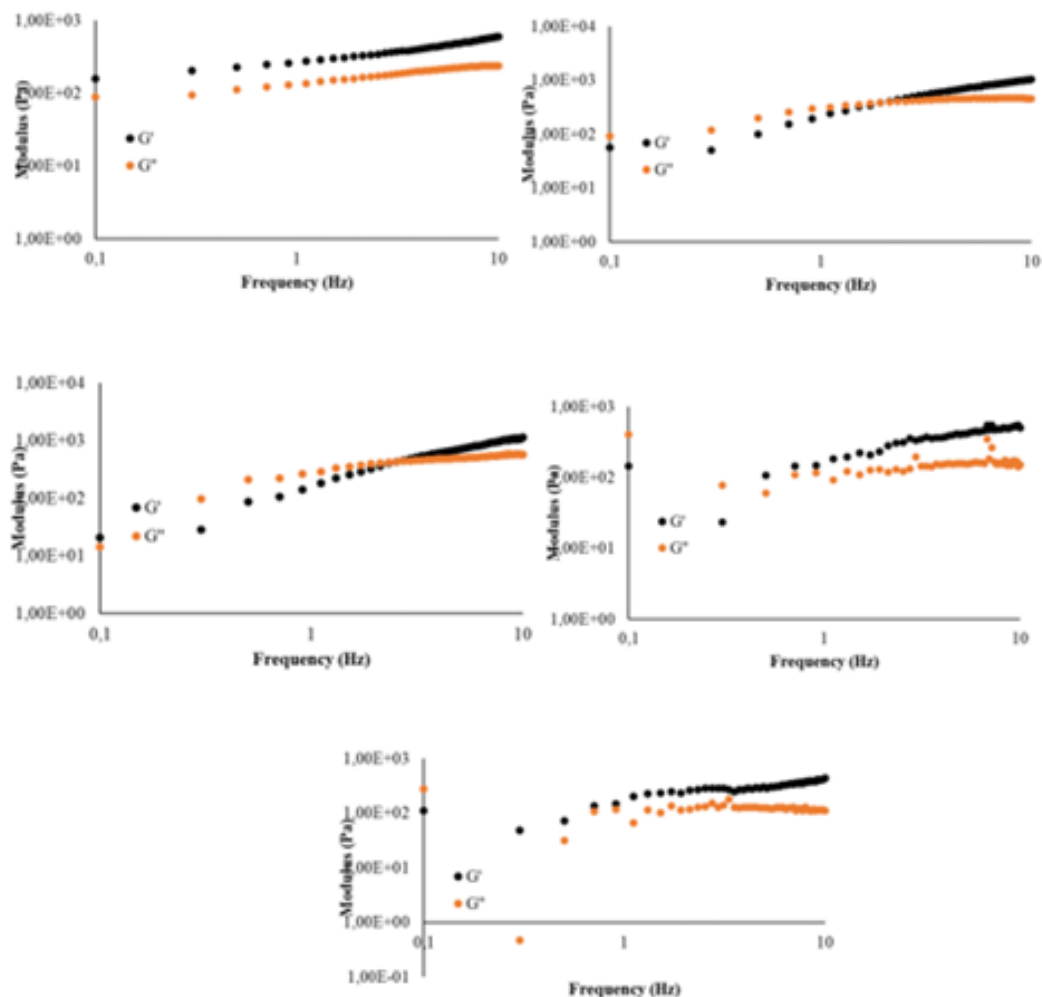
Figure 4-17 Variation of G and ´ G with frequency for a) 1:1 CTS/CMC b) 4:1 CTS/CMC c) 8:1 CTS/CMC d) 1:4 CTS/CMC e) 1:8 CTS/CMC

For most of the formulation ratios, specifically 1:1, 1:4, 1:8 CTS/CMC the frequency sweep experiment with frequency range of 0.1-10 Hz and a strain of 0.5 showed G' to be larger than G''. The values of G' and G'' were seen to increase in all formulation ratio variants with increasing frequency, demonstrating the formation of a true gel with elements of robustness. This also suggests the existence of electrostatic interactions between chitosan and carboxymethylcellulose. For formulations 1:4 and 1:8

CTS/CMC, overlaps are seen in both graphs suggesting a transition from gel state to solution.

Furthermore, a graph of stress versus strain was plotted for all the samples with different formulation ratios and presented in figure below. This was done to determine the Elastic modulus, also called the Young's modulus or elastic constant (E), of all the hydrogels. From the graphs, it was seen that most of the CTS/CMC polymer composites had an elastic region comprising of three or more points including the origin that were linear. The slopes of straight lines of the linear regions of the graph, which was determined by the stress divided by the strain at that higher point on the line were calculated. The yield strengths of the various hydrogels on a stress-strain plot were determined by identifying the points at which the elastic region slope begins to curve. The Elastic modulus values for 4:1, 8:1, 1:4, and 1:1 CTS/CMC hydrogel formulations were determined to be 433, 570, 103.89, and 564.7 MPa respectively.

The yield strength values for 4:1, 8:1, 1:4, and 1:1 CTS/CMC hydrogel formulations were determined to be 13.65, 16.12, 13.86, and 23.56 MPa respectively. Some polymers deform so easily that they do not have an elastic region. In that regard, 1:8 CTS/CMC did not have a noticeably lower slope, hence there was no yield point to calculate.
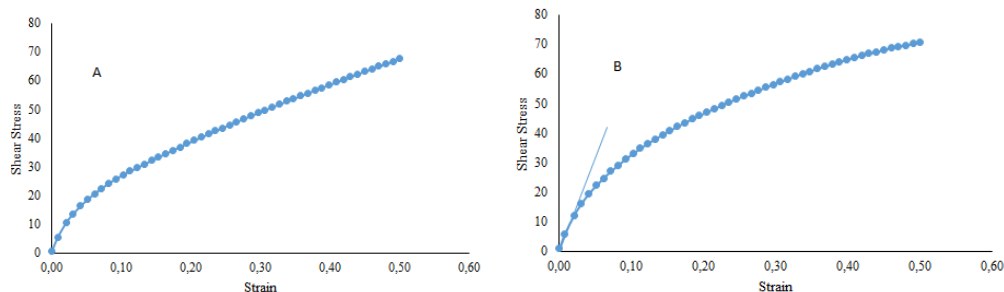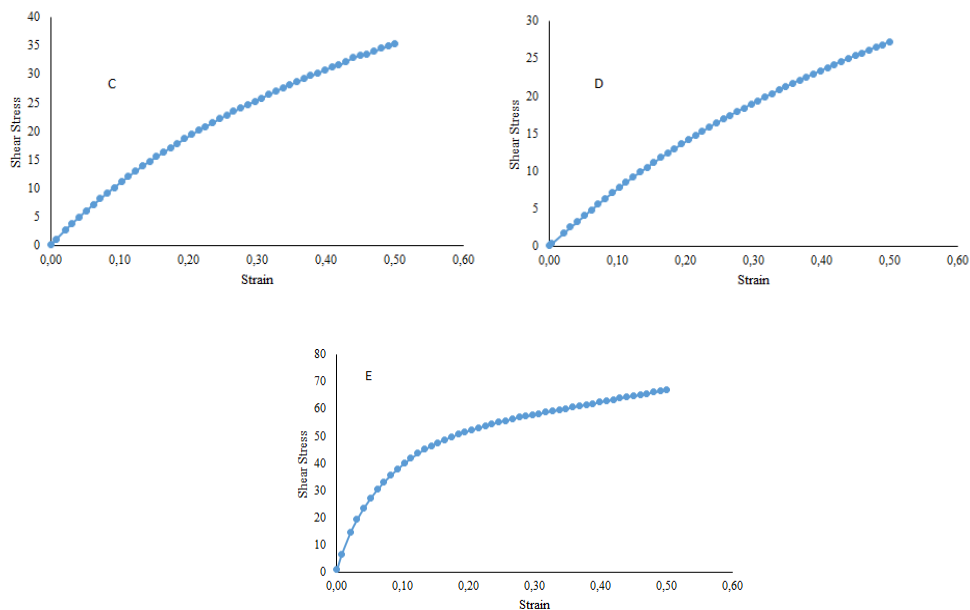
Figure 4-18 Stress versus strain curves for a) 4:1 CTS/CMC b) 8:1 CTS/CMC c) 1:4
CTS/CMC d) 1:8 CTS/CMC e) 1:1 CTS/CMC.

From the results obtained, the optimum CTS/CMC ratio for fabricating the ideal

composite was found to be 1:1.

Classification of Samples into Control and Experimental Groups

Samples were subsequently fabricated based on a 1:1 CTS/CMC volume-to

volume ratio and classified into 7 distinct groups and freeze-dried for further analyses.

- Group 1: CTS/CMC

- Group 2: CTS/CMC with 1% wt. HNT

- Group 3: CTS/CMC with 2.5% wt. HNT

- Group 4: CTS/CMC with 5% wt. HNT

- Group 5: CTS/CMC with 1% wt. Zn-HNT

- Group 6: CTS/CMC with 2.5% wt. Zn-HNT

- Group 7: CTS/CMC with 5% wt. Zn-HNT

Transmission Fourier Transformation Infrared Spectroscopy (FT-IR)

The Transmission FTIR spectra for nonmodified chitosan showed distinct peaks at 564 cm-1 and 711 cm-1 which are attributed to out-of-plane bending vibrations of C-O and NH. Additionally, vibrational peaks corresponding to bending vibrations of a primary amino group and the C-O stretching vibration (amide I) are observed at 1593 cm^{-1} and 1643 cm^{-1} respectively. O-H stretch peak was also noticed at 3400-3600 cm^{-1}.
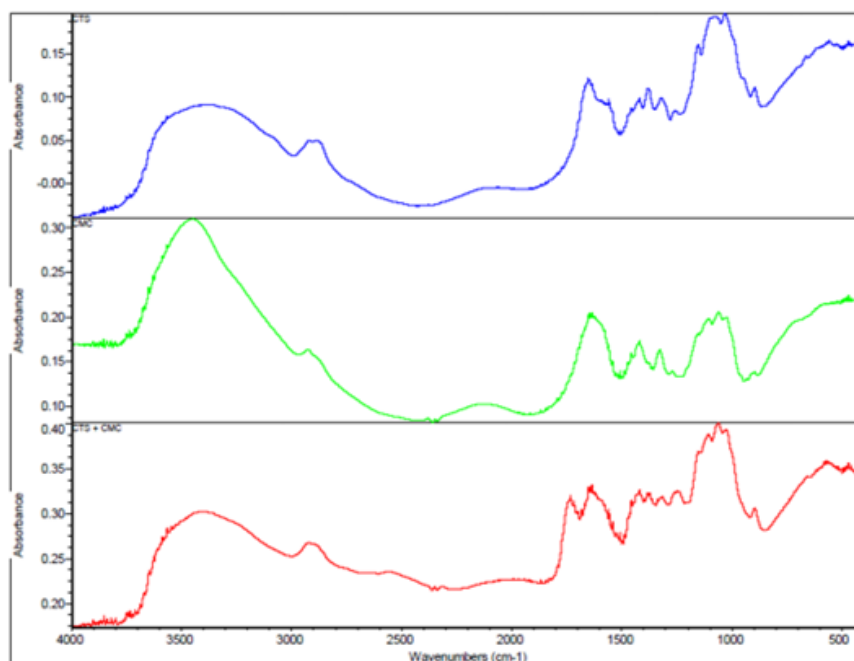
Figure 4-19 Transmission FT-IR showed expected peaks attributed to CTS, CMC, and CTS/CMC blend.

With respect to the FTIR spectra for CMC, peaks that are characteristic of CMC are observed at 1415 cm-1 and 1595 cm-1 corresponding to symmetric -COO and asymmetric -COO respectively. There is a broad absorption band observed at 3337 cm^{-1} corresponding to stretching vibrations of OH group. The peaks at 2948 cm^{-1} and 2134 cm^{-1} are attributed to C-H stretching vibrations and vibrations of -CO groups respectively.

The CTS/CMC blend showed a distinct peak at 1703 cm^{-1} signifying the presence of carbonyl groups. This, together with the broadening of the peak at 3300-3600 cm^{-1} suggest the presence of intermolecular bonding between CTS and CMC.

Attenuated Total Reflectance Fourier Transformation Infrared Spectroscopy (ATR FT-IR)

ATR FTIR technique was used for confirming the characteristic peaks for CTS, CMC and CTS/CMC blends as seen below.
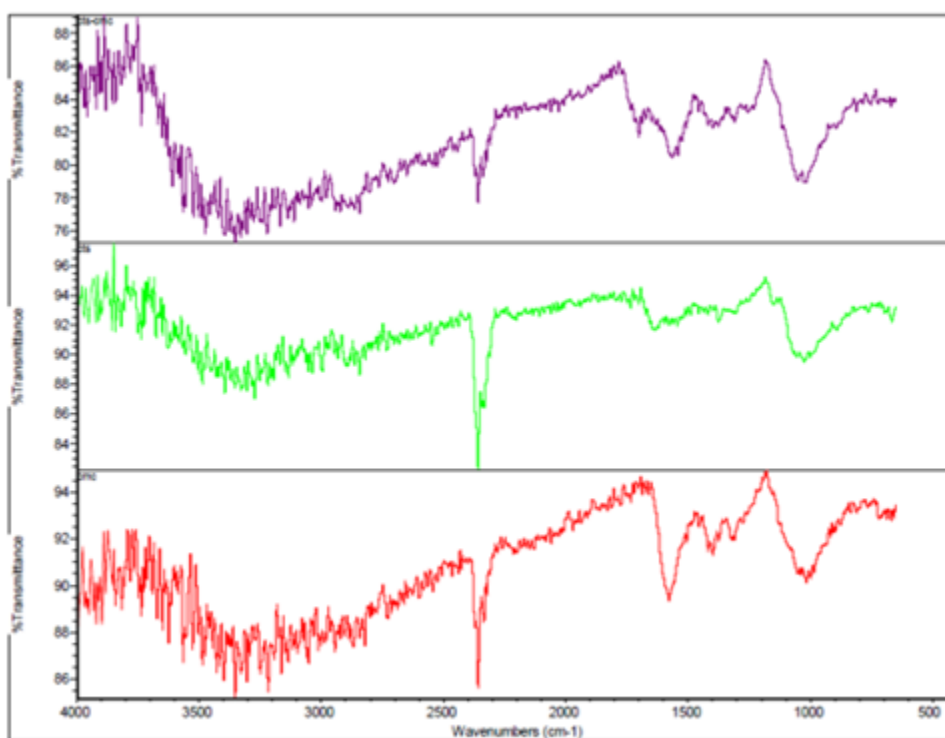
Figure 4-20 ATR FT-IR showed expected peaks attributed to CTS, CMC, and CTS/CMC blend.

Results obtained for the spectra of CTS, CMC and CTS/CMC blend using ATR-FTIR spectroscopy were similar to those obtained using the transmission FTIR spectroscopy for all three samples as described in previous sections above.

Scanning Electron Microscopy analysis

The morphology and surface topography of the freeze-dried CTS/CMC blend was analyzed via scanning electron microscopy at different magnifications with the results presented in Figure 4-21 below.
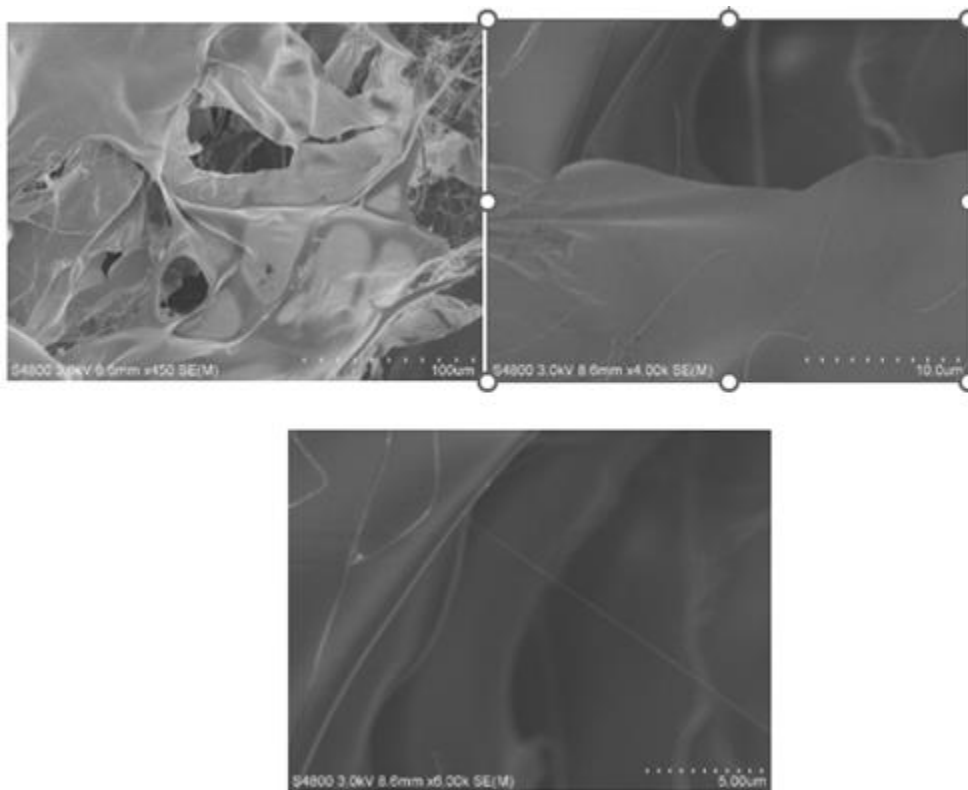
Figure 4-21 Scanning electron microscopy images of cross sections of CTS/CMC composite at a) 100 um b) 10 um c) 5 µm.

These results are suggestive of the formation of a CTS/CMC blend with good microstructure and complex fiber network as seen in figure 3a. The surface was seen to be relatively smooth.

X-Ray Diffraction analysis

Figure 4-22 below shows the XRD results for chitosan, carboxymethyl cellulose and a blend of chitosan and carboxymethyl cellulose. The characteristic peaks for

chitosan are seen with crystalline structure at 2 theta values of 20°. Similarly, CMC also

exhibited a broad peak at 2 thetas equaling 20°.
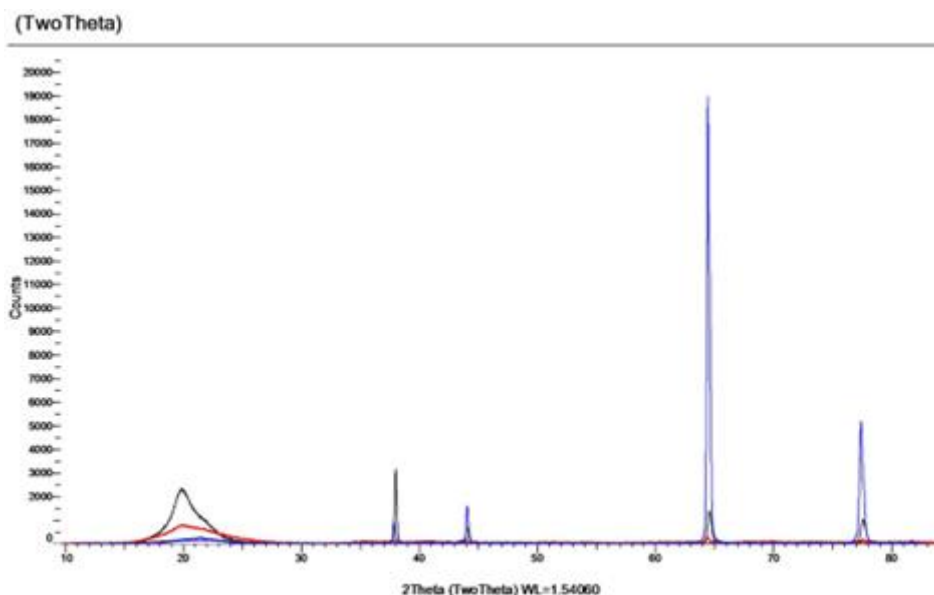
Figure 4-22 XRD graph image of CTS (black), CMC (red) and CTS/CMC blend (blue).

Thermogravimetric analysis

The thermogravimetric curve for pristine HNT showing the percentage mass loss

at increasing from 40 ºC to 600 ºC is shown in figure 4-23 below. The thermally

activated occurrence seen starting from 450 ºC to 600 ºC is attributed to the loss of water

in a dehydration process. Similar to data obtained from literature [176], weight-loss

occurrences at temperatures beyond 450–600 °C are attributed to the loss of structural

water owing to degradation of clays like halloysite. The absence of initial weight loss is indicative of the anhydrous nature of HNTs.
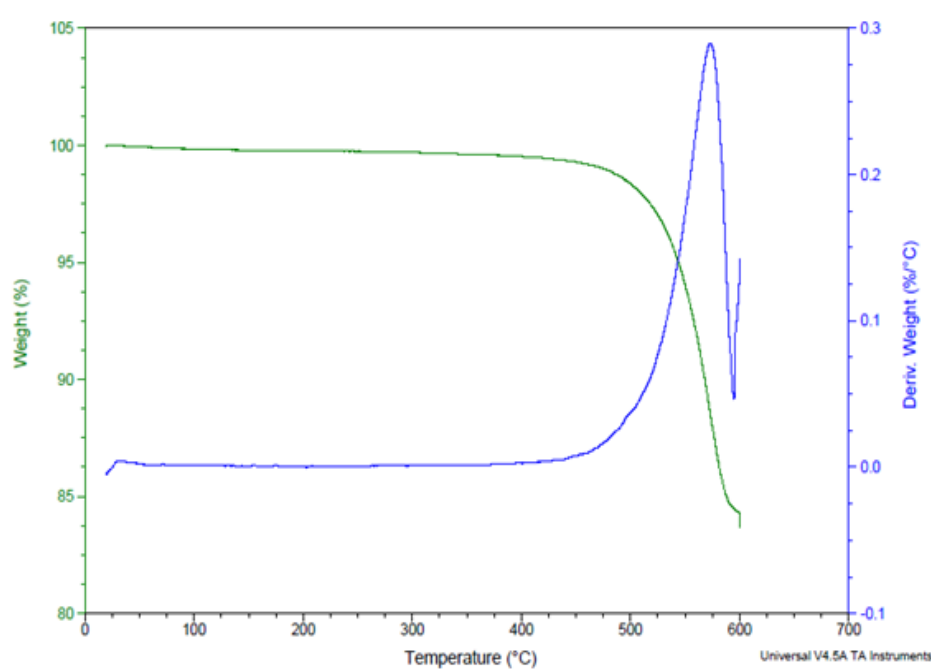
Figure 4-23 Thermogravimetric curve of pristine HNT sample.

The thermogravimetric curve of the CTS/CMC composite showed a significant weight-loss stage at 40–113 °C. This could be attributed to the loss of water molecules that are bound to the composite as well water molecule that were adsorbed onto the biomaterial during the various stages of preparation and storage. A second weight loss

step is observed at 275–480 °C, which could depict the point at which thermal

degradation is initiated. Approximately 60% of the total weight was lost up until 600 ºC.
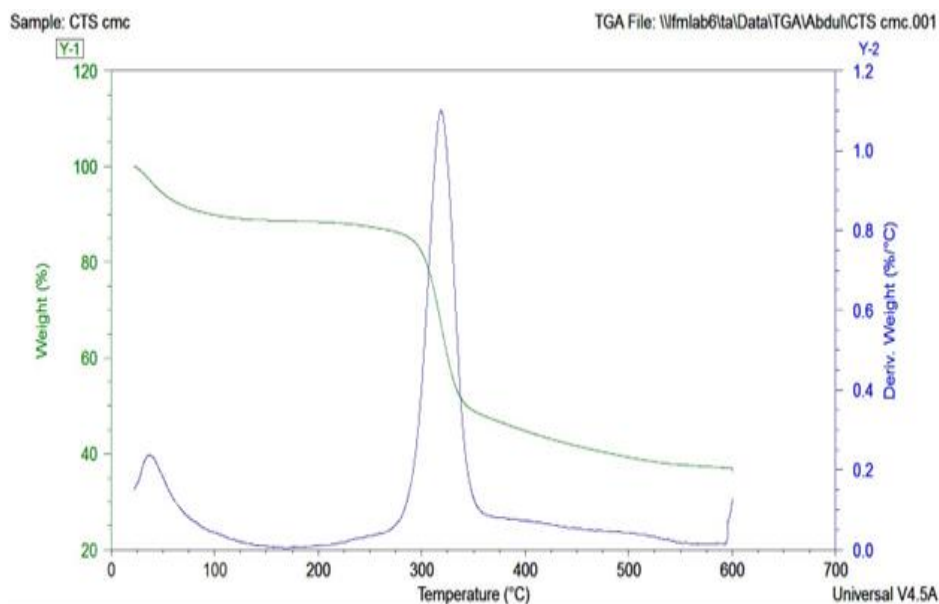
Figure 4-24 TGA curve for CTS/CMC composite blend

The thermogravimetric curve of the CTS/CMC incorporated with 5% w/v zinc-

doped HNT composite showed weight loss patterns similar to that of the CTS/CMC

polymer blend. A significant weight-loss stage attributed to the loss of adsorbed and

structural or bound water molecules is seen at 40–113 °C. A second weight loss step is

observed at 300–480 °C, which could depict the point at which thermal degradation is

initiated. Approximately 35% of the total weight was lost up until 600 ºC.
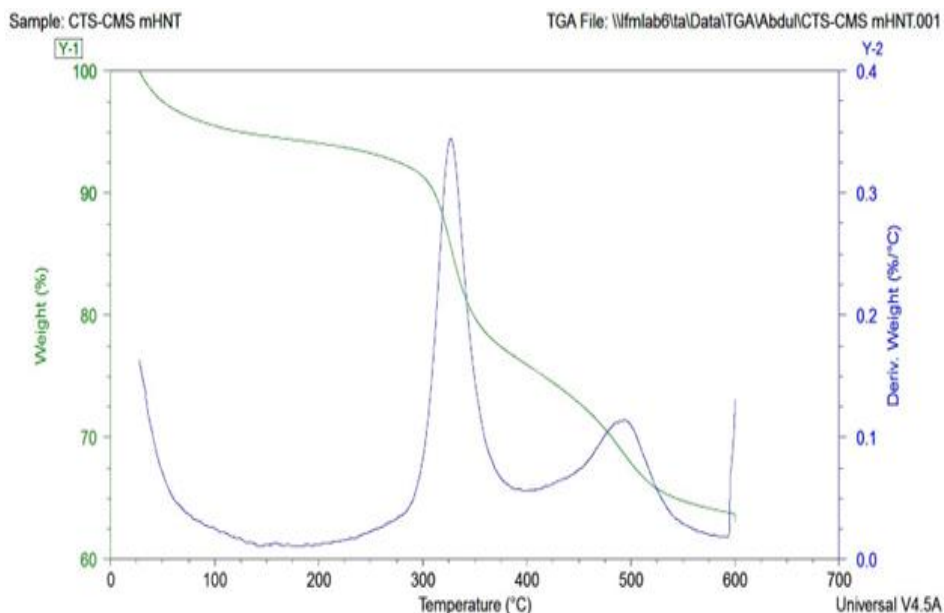
Figure 4-25 TGA curve for CTS/CMC composite blend incorporated with 5% w/v zinc doped HNT.

MultiBET/pore size testing

The freeze-dried samples were purged of all gases and cooled using liquid nitrogen. An inert nitrogen gas was then used to probe the samples by absorbing it onto the sample surface. With the outgas temperature kept constant at 60 ºC, the system pressure was increased to allow adsorption of more gas molecules. The BJH adsorption summary for actual surface area and pore radius of each sample was then deduced by the analyzer based on the number of adsorbed gas molecules.

The results showed that CTS/CMC polymer composite had an average pore of radius 12.092 E. The polymer composites incorporated with 1% HNT had an average pore radius of 13.147 E and the polymer composite doped with 5% HNT had an average pore radius of 14.027 E. There was no significant difference between the pore sizes of

CTS/CMC and CTS/CMC reinforced with 1% HNT. However, incorporation of 5% HNT

into CTS/CMC significantly increased the pore size.
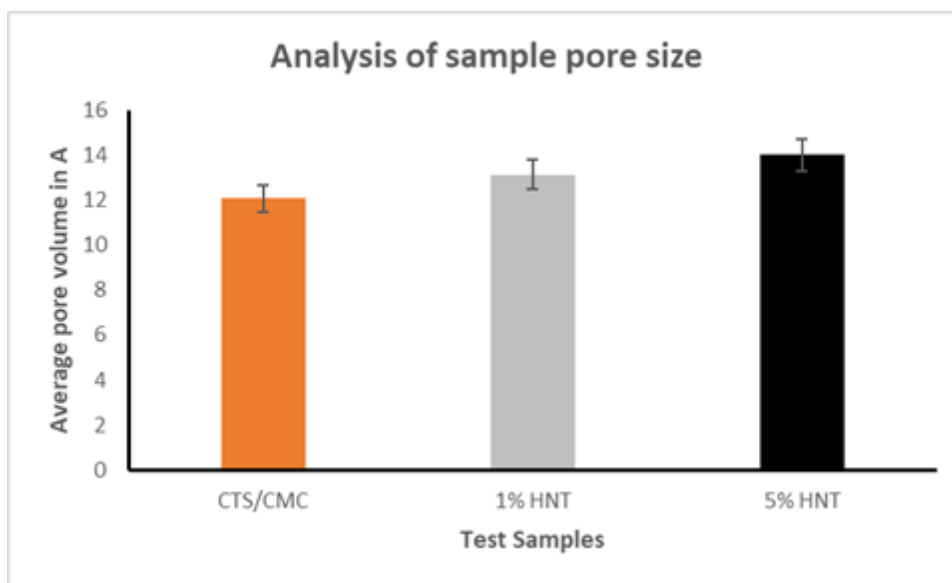
Figure 4-26 Average Pore radius of freeze-dried polymer composites based on percentage of HNT incorporated. N=3

Analysis of the total surface area of the samples anlyzed showed that CTS/CMC

polymer composite had an average surface area of 13.025 ml/g, polymer composites

incorporated with 1% HNT had an average surface area of 16.665 ml/g and polymer

composites doped with 5% HNT had an average surface area of 46.978 ml/g. Therefore,

both pore sizes and total surface area seemed to increase with increasing concentrations
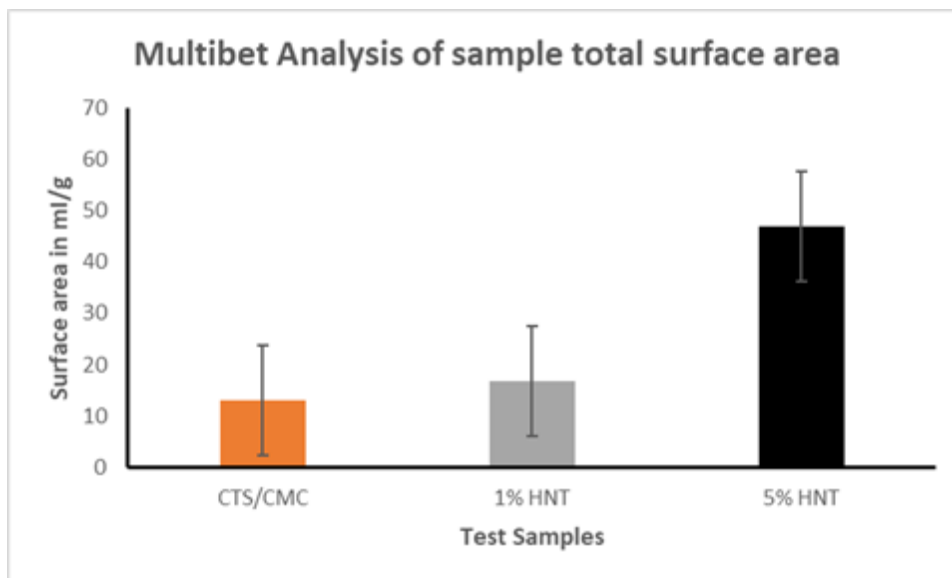
of HNTs.

Figure 4-27 Average surface area of freeze-dried polymer composites based on percentage of HNTs incorporated. N=3

Controlling the porosity microarchitecture of hydrogel-based biomaterials via pH adjustment is a feasible process in tissue engineering. Ananlyses of the pore size and total surface area of the fabricated biomaterial based on pH was carried out and the results presented in figure 4-28 and figure 4-29 below. CTS/CMC freeze-dried test samples fabricated at pH 2, pH 4 and pH 6 had pore radiuses of 12.092 E, 12.159 E and 13.04 E, and total surface areas correspposonding to 30.032 mI/g, 13.025 mI/g and 9.102 mI/g respectively.
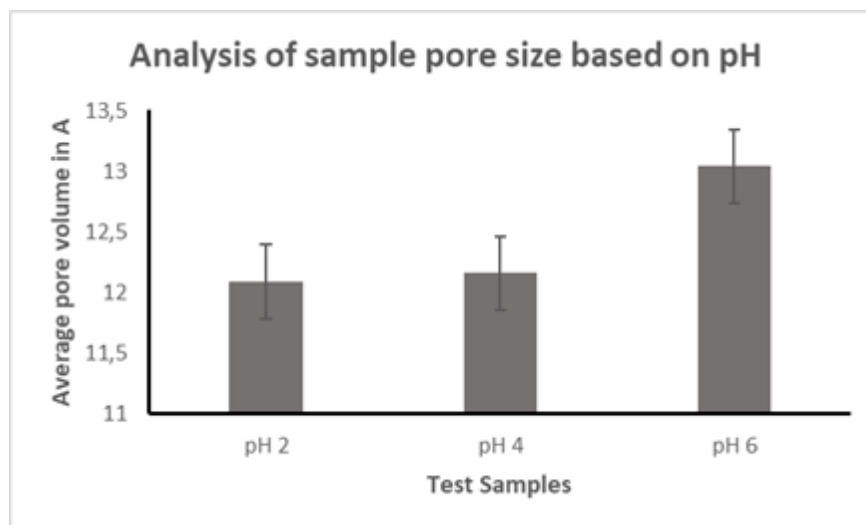
Figure 4-28 Average Pore radius of freeze-dried polymer composites based on % HNT incorporated. N=3

Generally, pore size was seen to increase with increasing pH while the total total surface of the samples decreased with increasing pH.
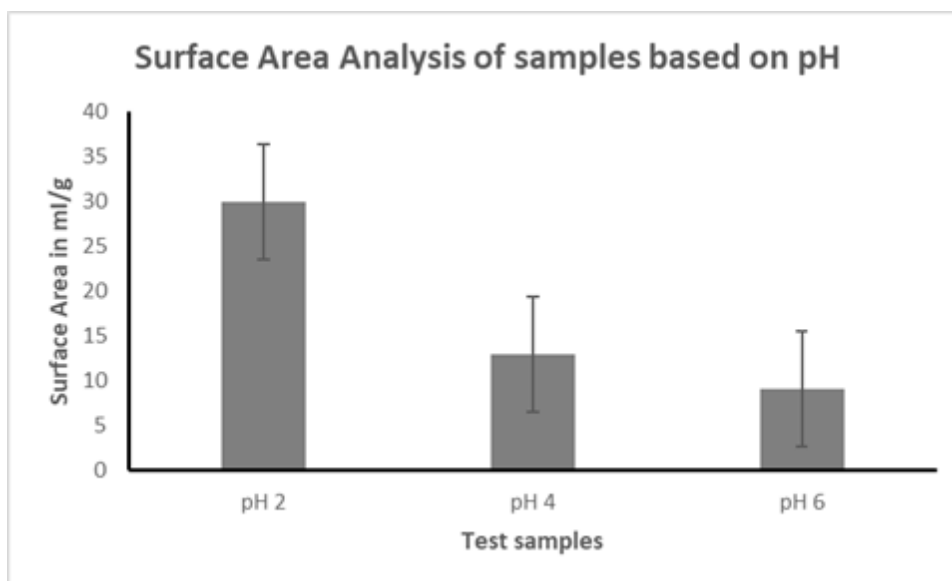
Figure 4-29 Average surface area of freeze-dried polymer composites based on pH. N=3

Spreadability test

Figure 4-30 below shows the results of the Spreadability test carried out using chitosan, carboxymethyl cellulose and a blend of the two polymers. From the results, it can be deduced that the CTS/CMC composite showed the highest spreadability with a contact angle of approximately 45 degrees, making it the most hydrophobic.
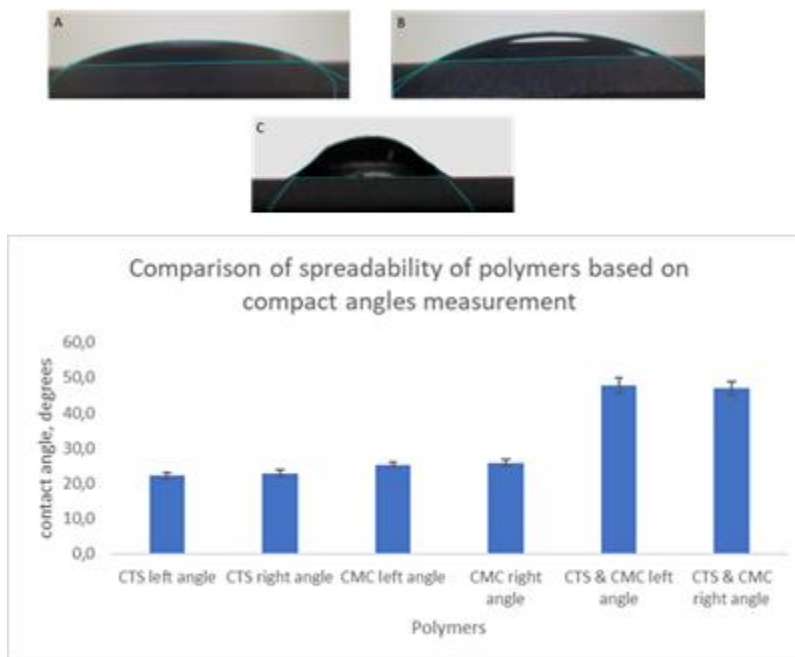
Figure 4-30 (A) Contact angle image of CTS (B) Contact angle image of CMC (C) Contact angle image of CTS+CMC, (D) Graphical representation of polymer spreadability. N=3
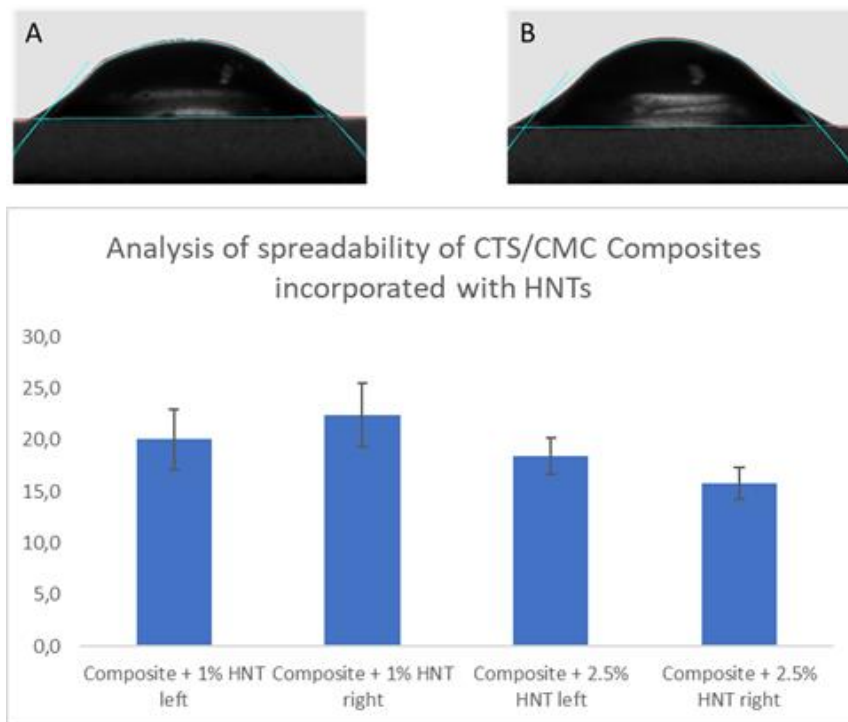
Figure 4-31 (A) Contact angle of composite + 2.5% HNT, (B) Contact angle of composite + 1% HNT (C) Graphical representation of spreadability of composites + HNT. N=3

Assessment of swelling properties and water content

The swelling test using the fabricated composites was carried out to establish the amounnt of water the composites could absorb. The results illustrated in figure 4-32 and figure 4-33 below show that the incoporation of different proportions of halloysites and zinc doped halloysites significantly reduced the swelling properties of the composites compared to the pure chitosan/carboxymethyl cellulose composite. The swelling ratios of all the composites spiked sharply from 0 minuutes to 20 minutes with no further increase in swelling until the 100th minute. The pure CTS/CMC composite exhibited the highest swelling ratio (2000). Relatively equal amount of water was absorbed by the The amount of water absorbed by chitosan-based composites incorporated with 1% HNT, 5% HNT,

1% ZnHNT and 5% ZnHNT post submession in water. The water content remained

content of these components remaind relatively the same for the duration of the test

(approximately 94%). On the contrary, the pure CTS/CMC composite had the highest

water content after 100 minutes of submerssion in water (approximately 98%).
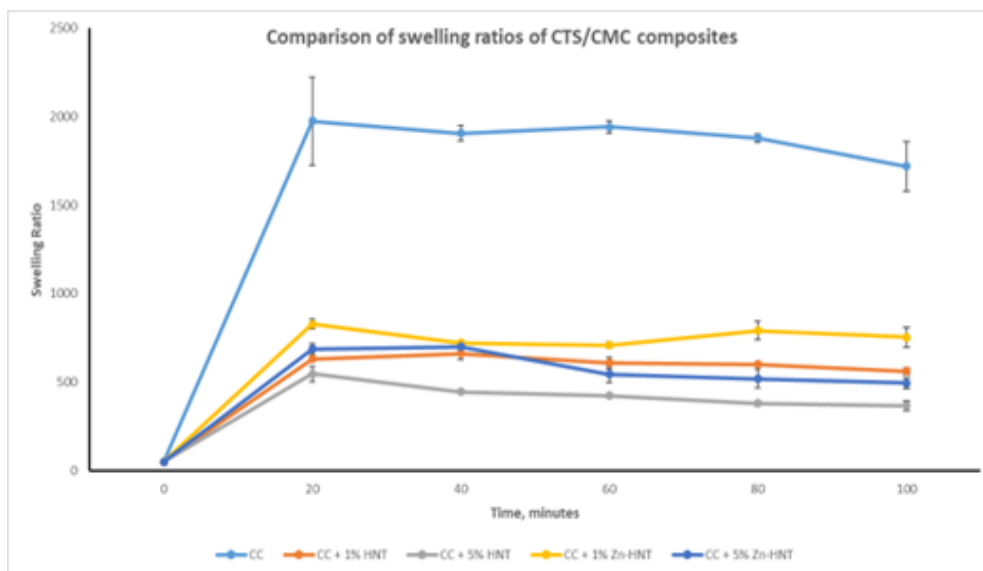
Figure 4-32 Average swelling ratios of CTS/CMC composites. N=3
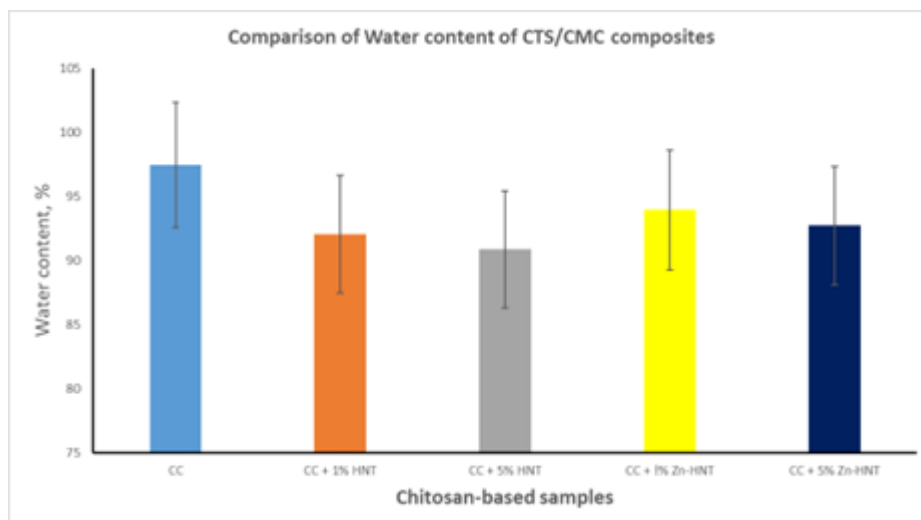
Figure 4-33 Average water content of CTS/CMC composites. N=3

4.2   Project 2: In vitro assessment of the effect of the fabricated chitosan-based composite on wound closure and cell migration

4.2.1   Kirby Bauer Disk Susceptibility Test

Figure 4-34 below shows the successful serial dilution of *E. coli* and *S. aureus* bacteria culture prior to their use for the Kirby Bauer Disc susceptibility test for the assessment of bacterial growth inhibition.
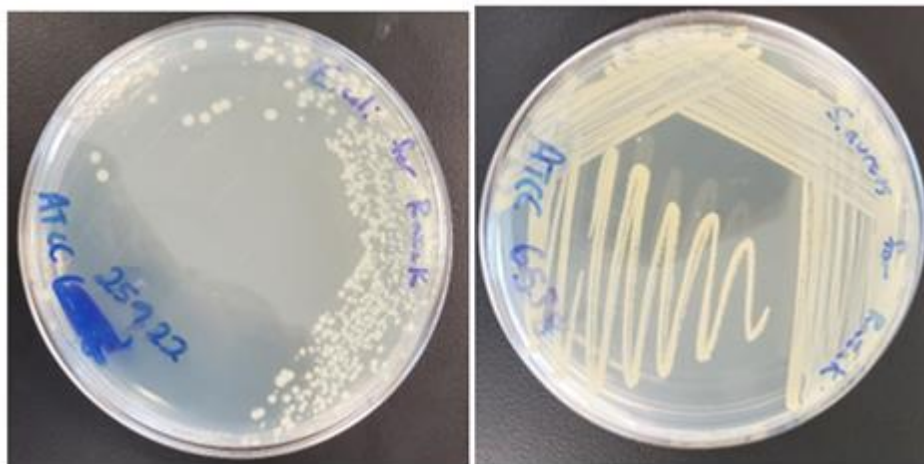
Figure 4-34 *E. coli* and *S. aureus* bacteria grown on plates containing growth media.

Figure 4-35 and Figure 4-37 below depict the images of the zones of inhibition formed against *E. coli* and *S. aureus*. The graphical representations of the results obtained for this test post measurement are presented in Figure 4-36 and Figure 4-38 below for *E. coli* and *S. aureus* respectively. From the results obtained, it is seen that the standard gentamicin disc significantly inhibited the growth of *E. coli* and *S. aureus* after 24 hours and 18 hours respectively. CTS/CMC and CTS/CMC discs doped with different HNT concentrations did not show any significant inhibition of *E. coli* growth compared to the gentamicin control discs. On the contrary, CTS/CMC discs doped with gentamicin loaded HNTS and CTS/CMC discs doped with gentamicin loaded ZnHNTs showed

antimicrobial effects similar to the control discs. The highest zones of inhibition against

E. coli were formed by CTC/CMC discs doped with 5% gentamicin loaded ZnHNTs.
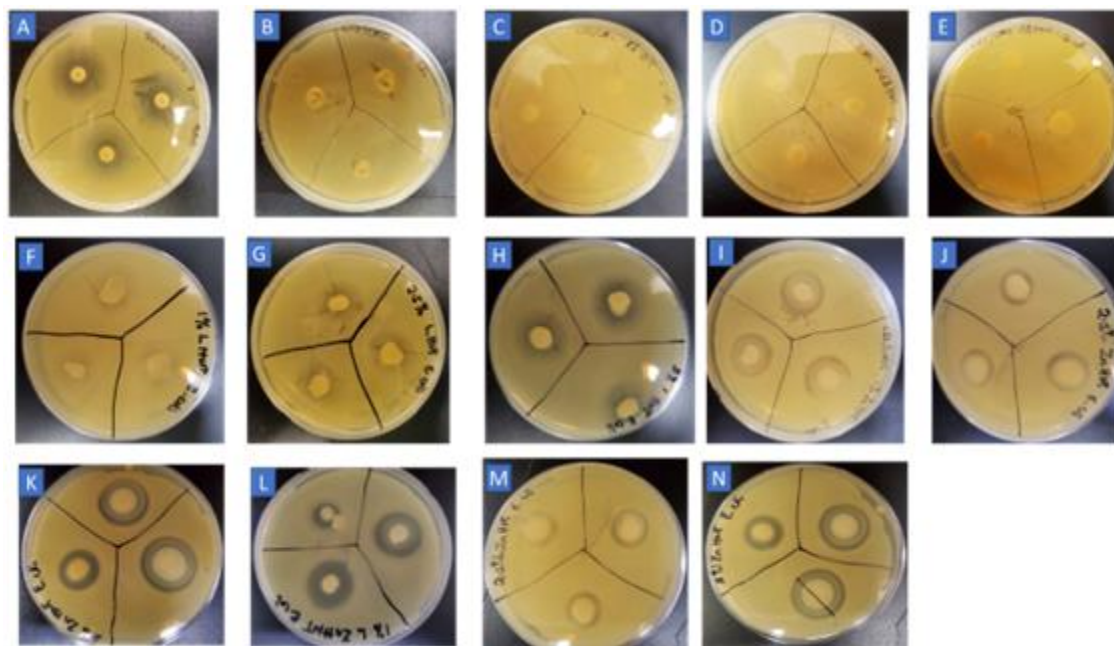
Figure 4-35 Image of *E. coli* bacteria culture plates with (A) Gentamicin disc (B) CTS/CMC (C) CTS/CMC+1%HNT (D) CTS/CMC+2.5%HNT (E) CTS/CMC+5%HNT (F) CTS/CMC+1%LHNT (G) CTS/CMC+2.5%LHNT (H) CTS/CMC+5%LHNT (I) CTS/CMC+1%ZnHNT (J) CTS/CMC+2.5%ZnHNT (K) CTS/CMC+5%ZnHN
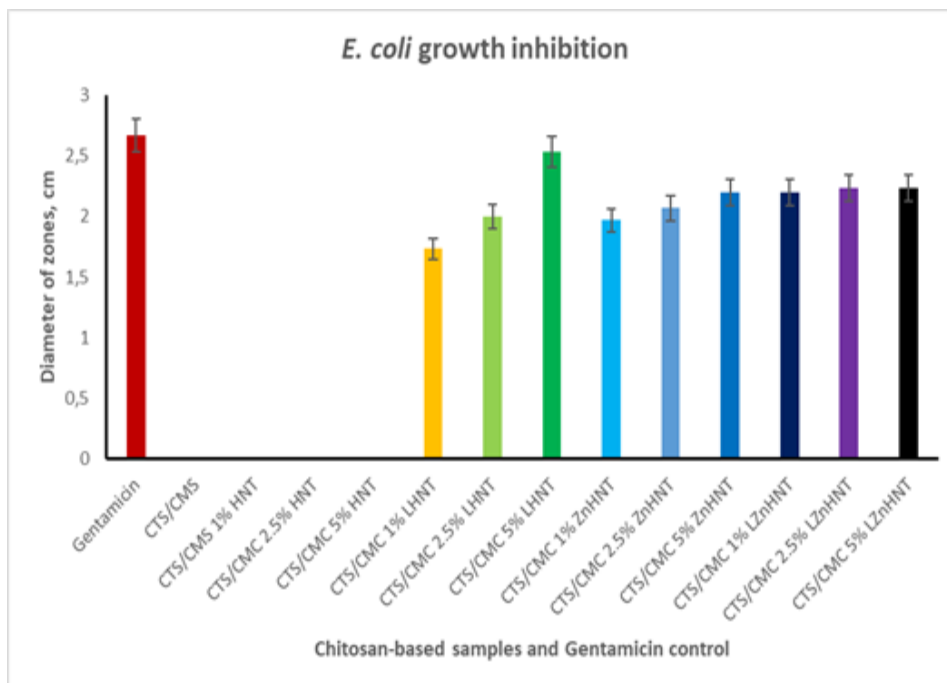
Figure 4-36 Graphical representation of *E. coli* susceptibility to different chitosan-based samples and gentamicin control disc. N=3

Similar results were obtained with respect to *S. aureus* growth inhibition. The

gentamicin control disc was more effective at suppressing the growth of *S. aureus*

compared to CTS/CMC and CTS/CMC discs doped with different HNT concentrations as

seen in the graph below. The most inhibition was recorded in CTS/CMC discs doped

with gentamicin-loaded HNTS and CTS/CMC discs doped with gentamicin-loaded

ZnHNTs. Similarly, Figure 4-37 below shows CTS/CMC samples and CTS/CMC+HNT

samples having so visible zones of inhibition, whereas zones of inhibition were seeable

around the gentamicin control disc, CTS/CMC discs doped with gentamicin-loaded

HNTS and CTS/CMC discs doped with gentamicin-loaded ZnHNTs.
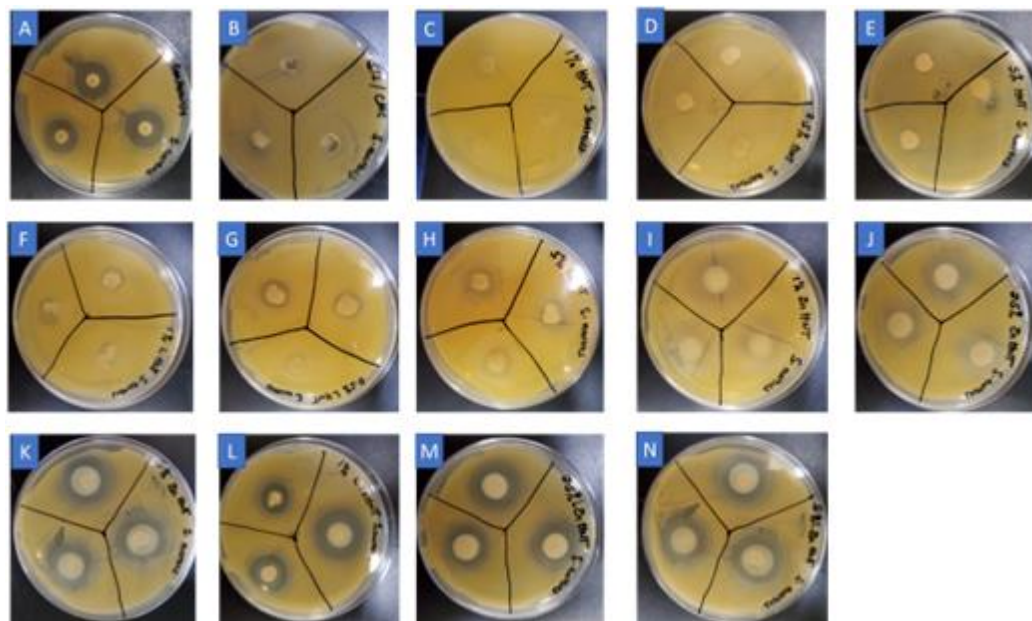
Figure 4-37 Image of *S. aureus* bacteria culture plates with (A) Gentamicin disc (B) CTS/CMC (C) CTS/CMC+1%HNT (D) CTS/CMC+2.5%HNT (E) CTS/CMC+5%HNT (F) CTS/CMC+1%LHNT (G) CTS/CMC+2.5%LHNT (H) CTS/CMC+5%LHNT (I) CTS/CMC+1%ZnHNT (J) CTS/CMC+2.5%ZnHNT (K) CTS/CMC+5%Zn. N=3
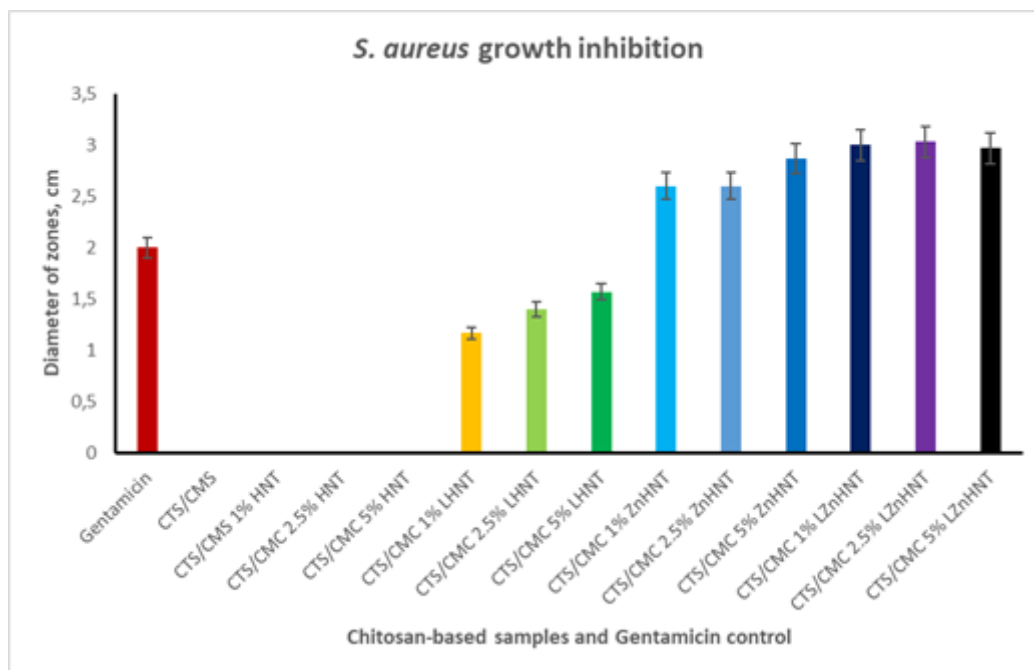
Figure 4-38 Graphical representation of *S. aureus* susceptibility to different chitosan-based samples and gentamicin control disc. (A) CTS/CMC disc (B) CTS/CMC+1%HNT (C) CTS/CMC+2.5%HNT (D) CTS/CMC+5%HNT (E) CTS/CMC+1%LHNT (F) CTS/CMC+2.5%LHNT (G) CTS/CMC+5%LHNT (H) CTS/CMC+1%ZnHNT (I) CTS/CMC+2.5%ZnHNT (J) CTS/CMC+5%ZnHNT(K) CTS/CMC+1%LZnHNT (L) CTS/CMC+2.5%LZnHNT (M) CTS/CMC+5%LZnHNT. N=3

4.2.2 Cell culture

Humand dermal fibroblasts were seen to be round shaped and adhered to the culture plate hours after seeding. The cells were seen to adopt their spindle-like morphology with no signs of contamination upon examination on day 1 and reached

about 70% confluence on day 3 as seen in Figure 4-39 below.

Figure 4-39 Microscopy images of human dermal skin fibroblasts.

Similar results were obtained for the culture of mouse mesenchymal stem cells as seen in Figure 4-40 below. The adipose-derived mesenchymal stem cells adhered to the surface of the culture plate hours after seeding on day 0. The cells began to adopt their spindled-shape morphology on day 3.
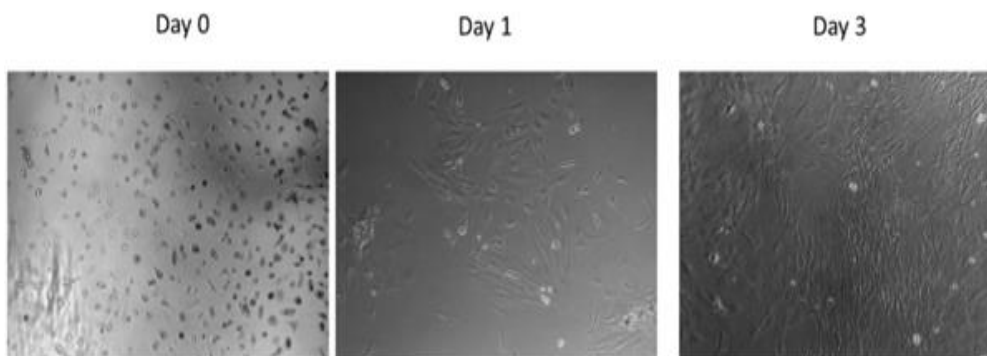
Figure 4-40 Microscopy images of mouse adipose-derived mesenchymal stem cells.

4.2.3 Cell proliferation assay

The proliferation test using fibroblasts showed that the control group of cells had a relatively similar growth profile compared to the pure CTS/CMC samples as well as the

samples incorporated with 1% HNT and 1% ZnHNT. The cells gradually grew in number over a period of 5 days and reached a peak optical density of approximately 1 nm on day 5. On the other hand fibroblasts exposed to CTS/CMC conjugates reinforced with 1% ZnHNT and 5% ZnHNT increased in density on day 1 and then experienced stagnated growth up until day 5 as seen in figure 4-41 below. A similar proliferation profile is seen when adipose-derived mesenchymal stem cells were used. Cells exposed to culture medium pre-conditioned with ZnHNT exhibited stagnated growth from day 1 to 5, compared to all other samples including the control group.
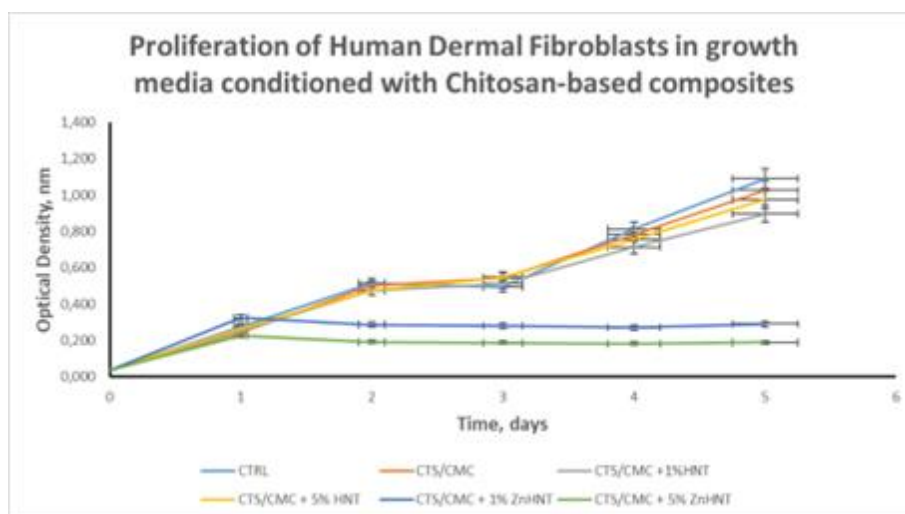
Figure 4-41 Proliferation assay using human skin dermal fibroblasts cultured in medium pre-conditioned with chitosan-based composites. N=3
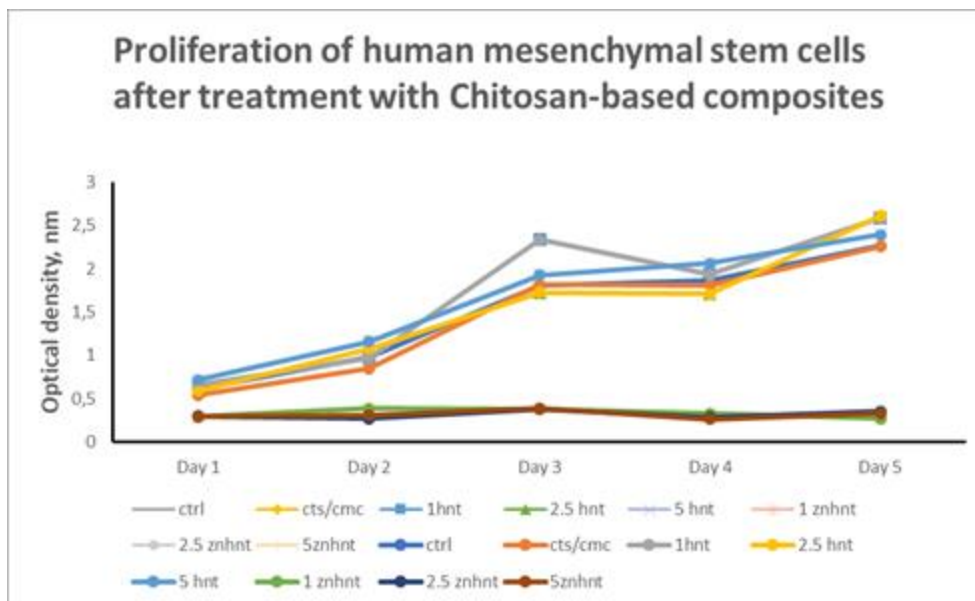
Figure 4-42 Proliferation assay using mesenchymal stem cells cultured in medium pre-conditioned with chitosan-based composites.

Live/dead assay

The live/dead assay was carried out as a measure of cytotoxicity to assess the effect of CTS/CMC composites and variations of it one the viability of human dermal fibroblast cells compared to a control groups. The control group was made up of cells cultured in pristine complete culture medium. Figure 4-43 shows an overlay of both live and dead cells cultured for days 1, 3 and 5. From the image below, live cells are stained green and dead cells are seen in red.
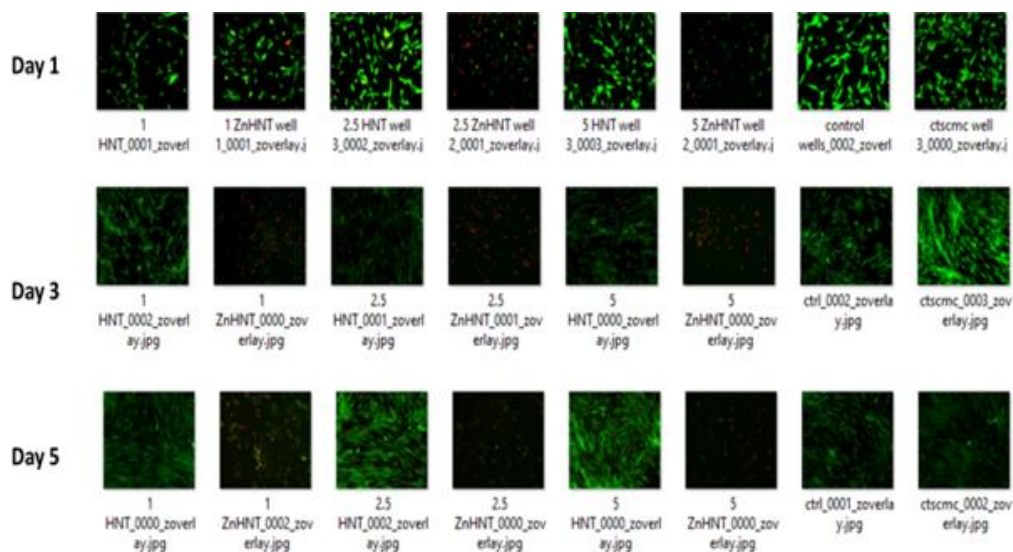
Figure 4-43 Overlay Images of Cytotoxicity test (live/dead assay) using human dermal fibroblasts cultured for 1, 3 & 5 days in media pre-conditioned with chitosan-based samples. Live cells are stained green, dead cells are stained red.
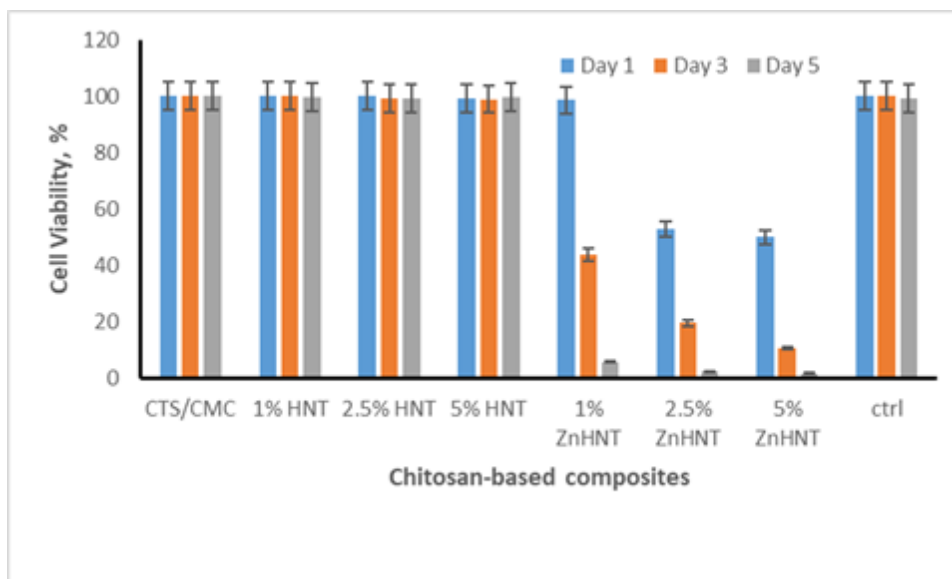
Figure 4-44 Graph showing viability of fibroblasts (live cells/total cell count) post treatment with medium pre-conditioned with chitosan-based composites. Error bars are standard deviations where n = 3.

The results obtained showed that cells treated with pristine halloysites at

concentrations of 1%, 2.5% and 5% remained viable over the 5-day test period similar to

the control cells. Cells treated with 1% ZnHNT were viable (98%) on day 1 with reference to the control group of cells (100%). However, the viability of the cells plummeted to approximately 43% on day 3 and 6% on day 5. Similar results were seen with regards to cells treated with 2.5% ZnHNT and 5% ZnHNT. The viability of cells recorded were 52.8%, 19.5% and 2.5% on days 1, 3 and 5 respectively for 2.5% ZnHNT. For 5% ZnHNT, the viability values obtained were 50%, 10.6% and 1.8% for days 1, 3 and 5 respectively. Cell counting was done using image J software.

4.2.4   Alizarin Red Staining Assay

Figure 4-45 below shows images of pre-osteoblast cells stained with Alizarin Red dye for 14 days post exposure to chitosan-based samples compared with untreated control group. Calcium deposition, represented by the red staining of cells was seen to increase steadily from day 1 to day 7 in cells treated with composites containing 1% HNT, 2.5% HNT, 5% HNT, CTS/CMC composites without HNTs as well as the control group of cells. The red staining of cells in all these groups was seen to be pronounce on day 14. Cells treated with CTS/CMC composites containing 1% ZnHNT, 2.5% ZnHNT and 5% Zn HNT were seen to have a distorted morphology while losing their adhesive properties thus, became less confluent with increasing number of days.

Figure 4-46 below shows the alizarin red standard curve plotted using known concentrations of alizarin red dye and their corresponding absorbance values at 405 nm. The concentrations of alizarin red in all experimental and control groups were determined based on the line of best fit obtained from the graph.

Additionally, a graph showing the quantification of calcium-containing osteocytes (concentration of alizarin dye in mM) post-treatment with chitosan-based samples for 14

days in comparison with untreated control group is presented in Figure 4-47 below. The

results confirm that there was no calcium deposition in the experimental and control

groups on day 1. However, calcium deposition was seen to occur on day 7 with the

highest concentration of alizarin dye obtained from the CTS/CMC and the control

groups. In agreement with the results from Figure 4-45, no calcium deposition was seen

in the groups of cells treated with composites containing zinc-doped halloysites on day 7.
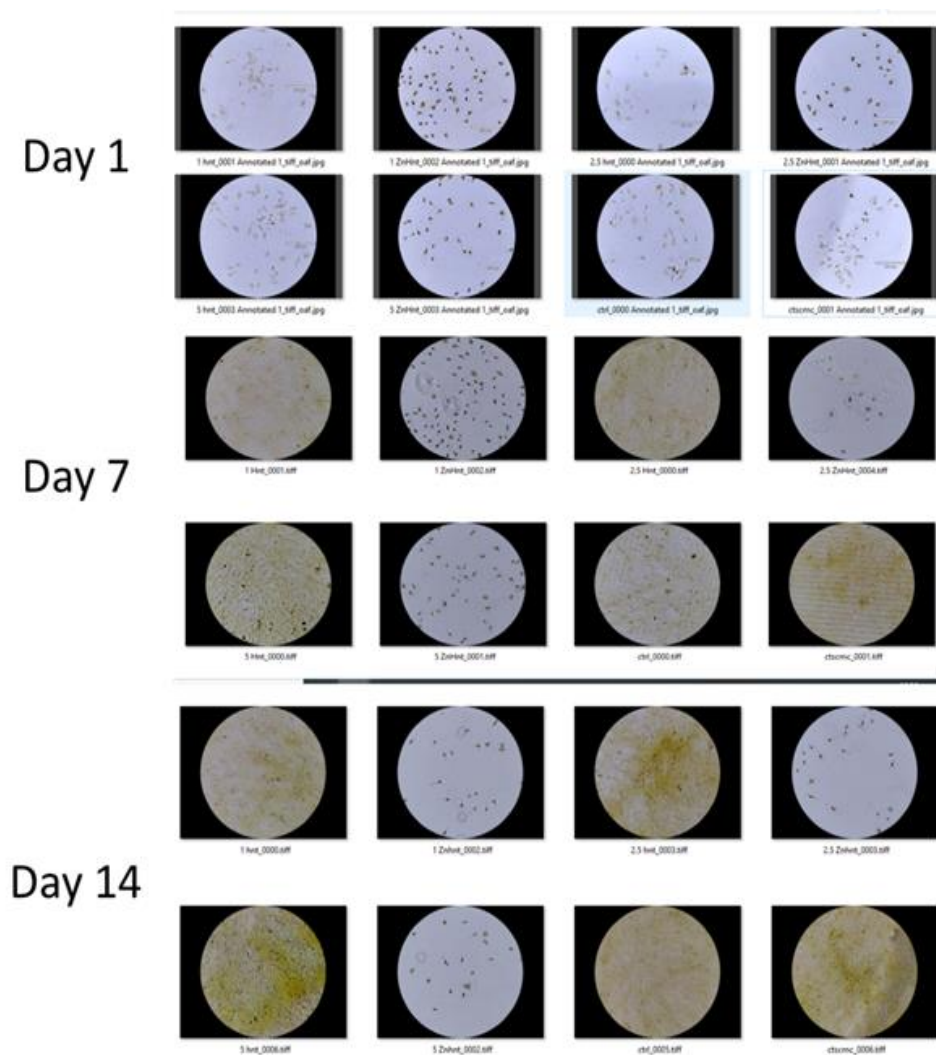
Figure 4-45 Images of Alizarin Red S stain of pre-osteoblast cell after exposure to chitosan-based samples compared with untreated control group.
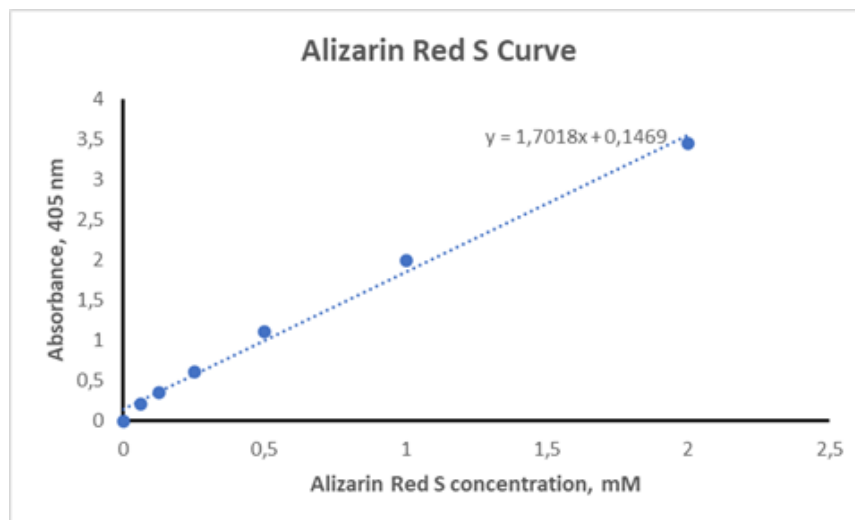
Figure 4-46 Alizarin Red Staining standard curve for quantification of calcification level of pre-osteoblast cells treated with chitosan-based samples in comparison with untreated control group.
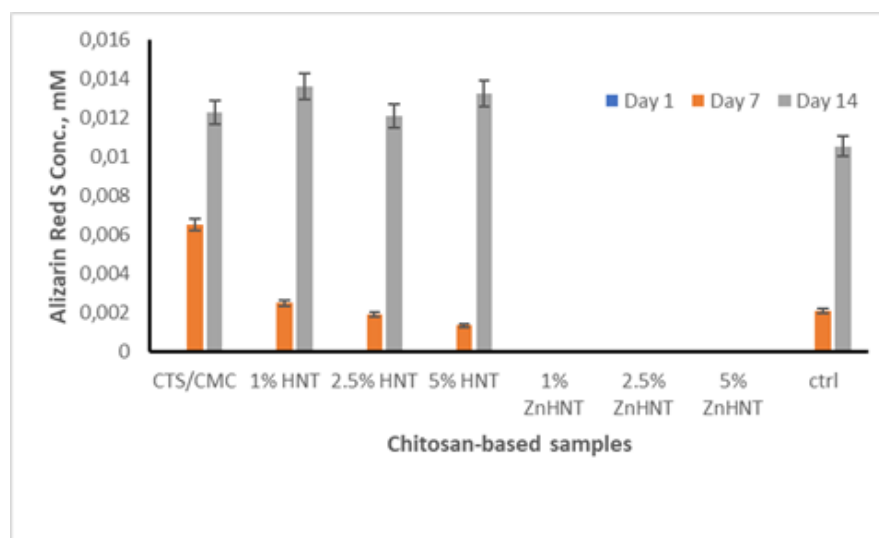
Figure 4-47 Graph showing the quantification of calcium-containing osteocytes post-treatment with chitosan-based samples for 14 days in comparison with untreated control group. N=3

Day 14 saw increased deposition of calcium in all experimental and control groups except those containing zinc doped HNTs. The highest concentration of alizarin dye was seen in the group of cells treated with composites doped with 1% and 5% HNTs.

4.2.5   S-beta-galactosidase staining

Figure 4-48 below show images of pre-osteoblast cells stained with S-beta galactosidase stain after 7 days of exposure to chitosan-based samples compared with untreated control group. S-beta galactosidase positive cells are seen stained in blue in the image.
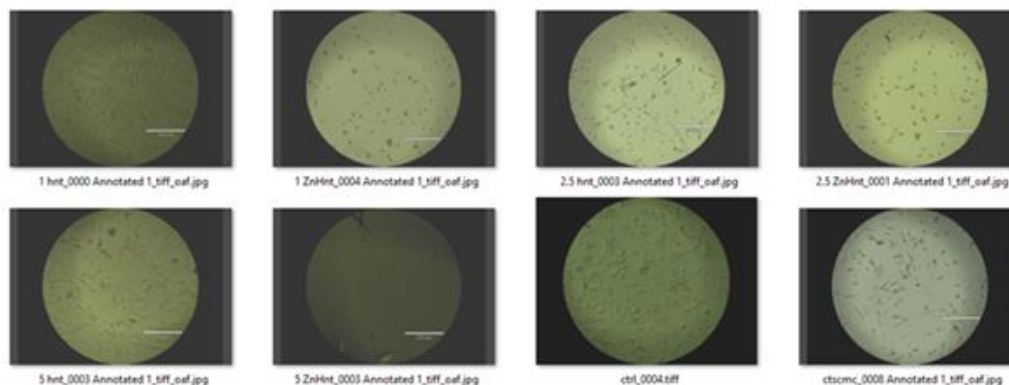
Figure 4-48 Images of fibroblast cells stained with s-β-galactosidase staining dye after exposure to chitosan-based composites. Pristine fibroblasts cultured in complete fibroblast cell culture medium cells served as the control group.

The results show few cells in the groups exposed to chitosan-based composites doped with HNTs to be s-beta galactosidase positive. The control group had the least number of cells stained positively for S-beta galactosidase. The group of cells exposed to chitosan-based composites doped with zinc coated HNTs though s-beta galactosidase negative, were seen to have a distorted morphology with decreased viability which is not representative of healthy fibroblast cells. A quantitative analysis of the s-beta galactosidase assay was carried out to assess the percentage of positively stained cells, with the results presented in Figure 4-49 below.
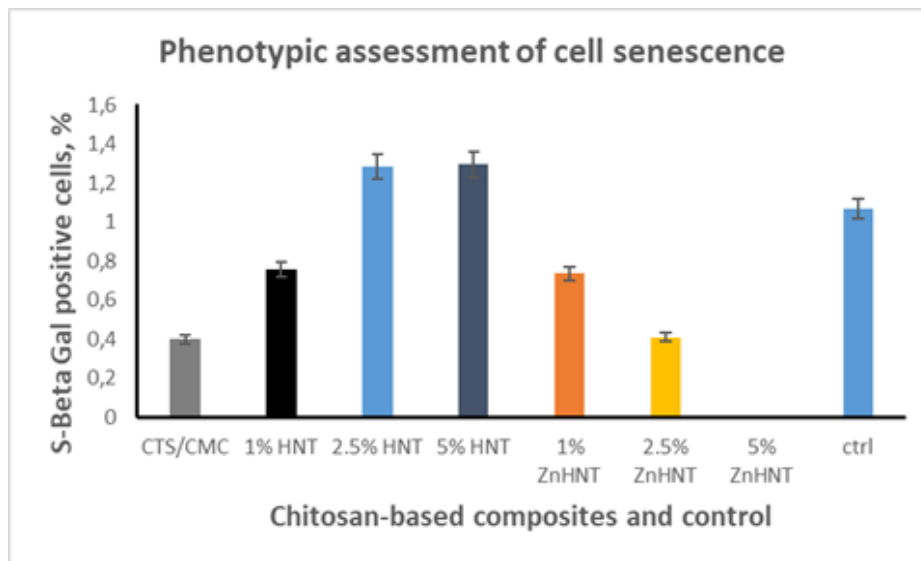
Figure 4-49 Quantification of β-Galactosidase positive stained cells cultured in medium pre-conditioned with chitosan-based composites compared to control group. Error bars are standard deviations where n = 3

4.2.6   Scratch assay

A scratch assay experiment mimicking the wound closure process was conducted over a 12-hour period to assess the migratory effect of fibroblast exposure to chitosan-based composites with respect to a control group of unexposed fibroblast cells. A 12-hour period was chosen due to doubling time of the cells causing the complete closure of the scratch area at times beyond 12 hours. The results of tracking migrating cells towards the scratch area are presented in Figure 4-50 and Figure 4-51 below.
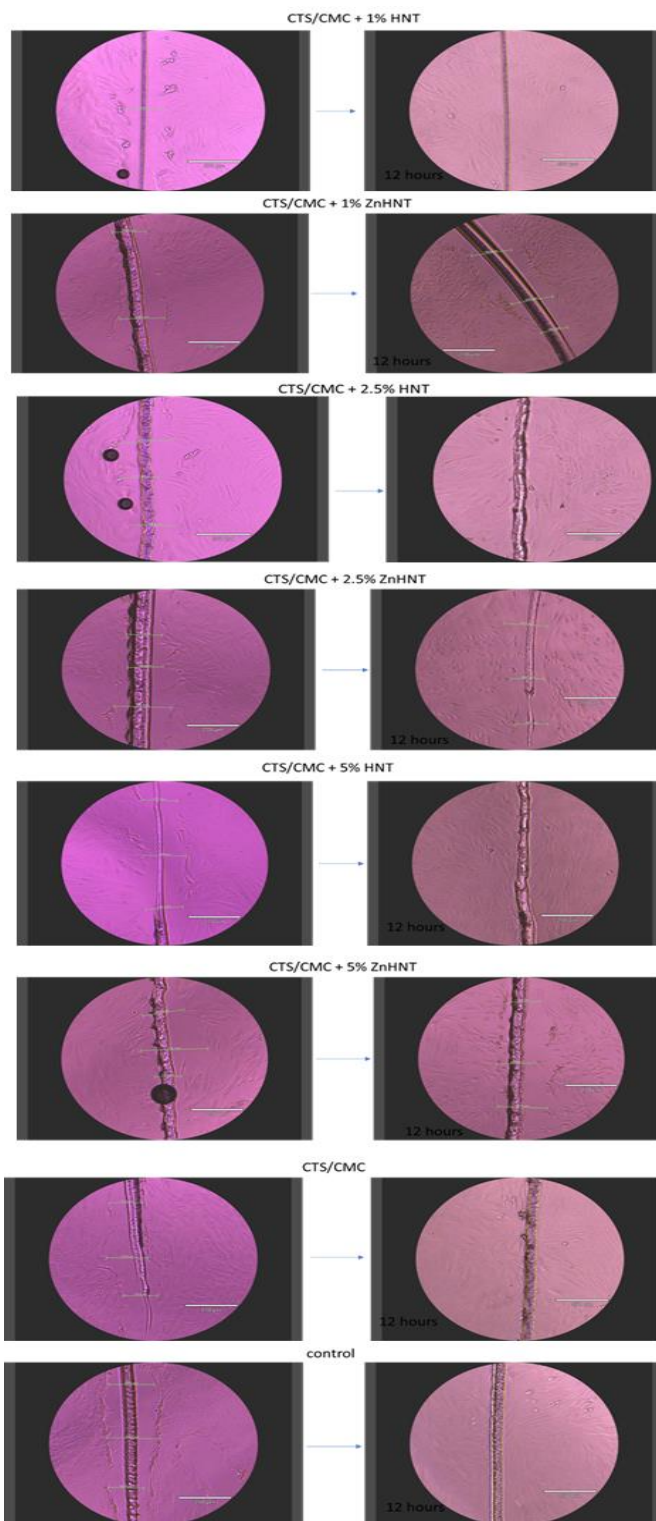
Figure 4-50 Scratch assay of controls compared to chitosan-based composites from time 0 hour to 12 hours.
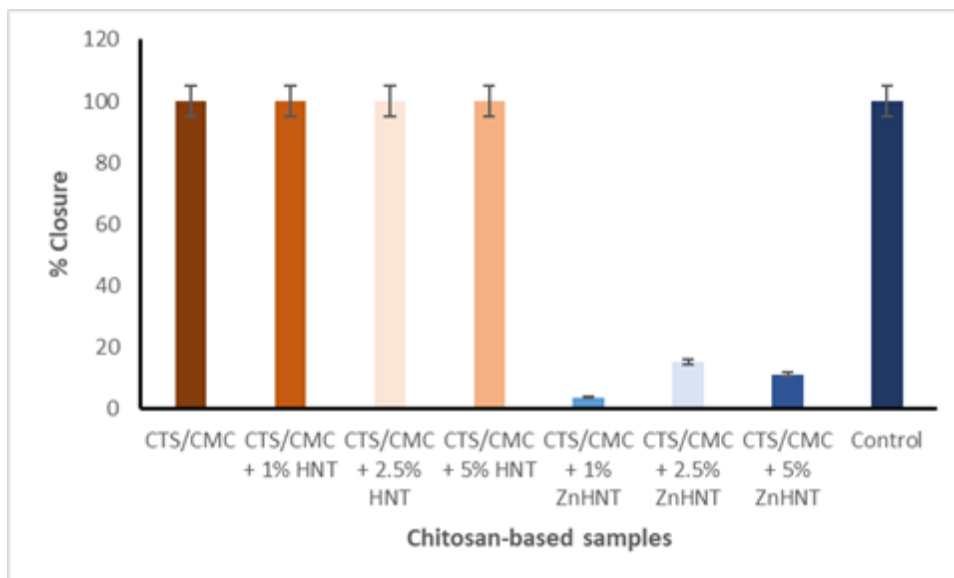
Figure 4-51 Graphical representation of scratch assay showing the percentage closure of scratch area by control fibroblast cells and cells exposed to chitosan-based composites for 12 hours. N=3

4.3 Project 3: Biofabrication and material characterization of Chitosan/Carboxymethyl cellulose solution casted membranes for various biomedical applications.

4.3.1 Evaluation of halloysite coating with copper oxide

FT-IR Analysis

Similar to the FT-IR results obtained and described in the sections above, Figure 4-52 below shows the peak comparison of pristine halloysites, copper oxide, and copper oxide halloysites. The HNT FT-IR spectrum of showed peaks at 748, 903, 1000, 3620 and 3690 cm^{-1} that are attributed to Si-O stretching vibrations, vibrations of inner hydroxyl groups (O-H), in-plane Si-O stretching, inner groups vibrations and inner surface O-H group stretching respectively. In agreement with data published in literature [135], [138], copper oxide FTIR spectrum showed the most agreeable peaks for CuO

located at 440 cm^{-1} and 480 cm^{-1} and 540. Copper doped HNTs did not show any distinct

peaks possibly due to the overlapping of peaks attributed to HNTs and CuO withing the

400 cm^{-1} to 1000 cm^{-1} range.
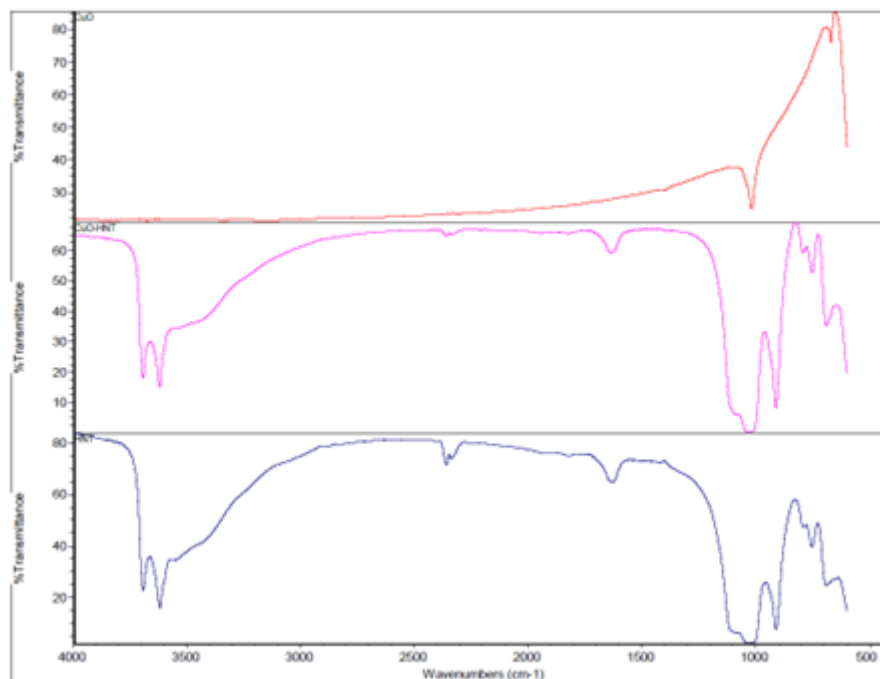
Figure 4-52 Transmission FTIR analysis of HNTs, copper oxide and copper oxide-HNTs demonstrating the characteristic FTIR absorption bands.

Scanning electron microscopy and EDX post CuO coating of HNTs

The structure and morphology of HNTs were captured by SEM with its elemental

composition assessed via EDX. Similar structural, morphological, and elemental analysis

of CuO-doped HNTs were carried out with the results present in figure 4-53 below. CuO

was deposited on the surface of halloysites in a mechanism similar to the deposition of

zinc oxide nanoparticles on halloysites explained in previous sections.
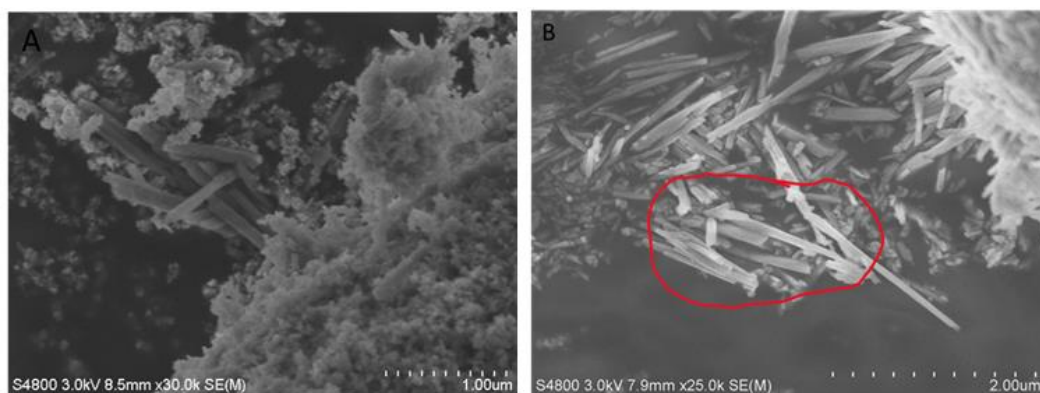
Figure 4-53 SEM images of A. Plain HNTs and B. CuO-coated HNTs

The results obtained confirm that halloysite nanoparticles exist as hollow

cylindrical tubes, which are rod-like in nature. Pristine halloysite nanotubes are seen to

have a plain and smooth surface topography in figure 4-53 A, whereas in figure 4-53B,

these rod-like tubes are seen to be granulated suggesting the successful coating of their

surfaces with copper oxide nanoparticles.
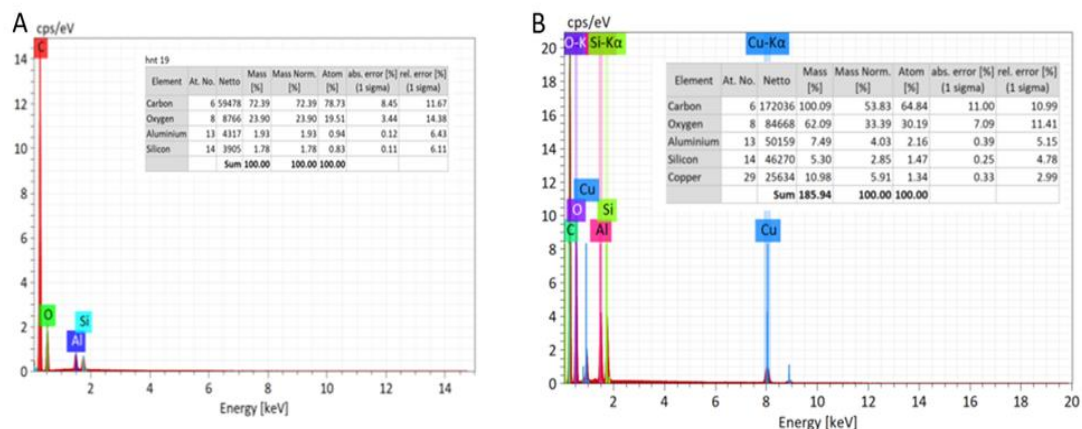
Figure 4-54 The quantitative elemental analysis of zinc doped HNTS, showing the weight
% of A) carbon [C], aluminum [Al], silicon [Si], oxygen [O] and B) copper [Cu].

The EDS results of pristine HNTs demonstrate the presence of its constituent elements in percentage weight. Carbon [C], aluminum [Al], silicon [Si], and oxygen [O] had values of 72.39%, 1.93%, 1.78%, and 23.9% respectively. As seen from figure 4-54 B, the EDS elemental analysis of copper oxide doped HNTs confirmed the presence of copper at 10.98%.

4.3.2   Fabrication of chitosan-based membranes

Chitosan/carboxymethyl cellulose film membranes (CTS/CMC), CTS/CMC membranes reinforced with 1% HNT, CTS/CMC membranes reinforced with 5% HNT, CTS/CMC membranes reinforced with 1% CuHNT and CTS/CMC membranes reinforced with 5% CuHNT were fabricated via solvent casting method and the results

shown in Figure 4-55 below.
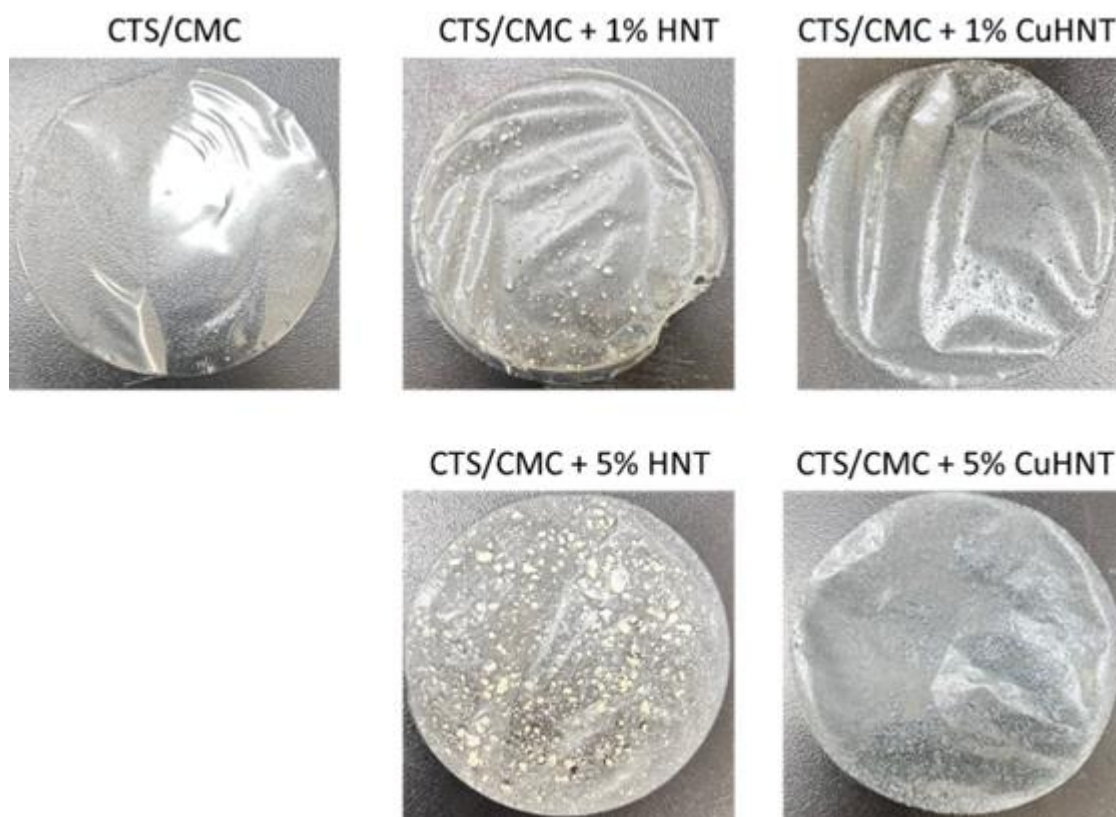
Figure 4-55 Images of chitosan-based membrane reinforced by different concentrations of HNTs and Copper doped HNTs.

FTIR Analysis

Figure 4-56 below confirms the presence of the expected functional groups of

HNT, Copper oxide and copper oxide HNT, chitosan-based film membrane, as well as

the membranes reinforced with HNTs, and copper oxide doped HNTs. All functional

groups were described in previous sections of this dissertation. All the film membranes

exhibited peaks at approximately 1578 cm^{-1} attributed to COO- group, which suggests an electrostatic interaction between chitosan and carboxymethyl cellulose.
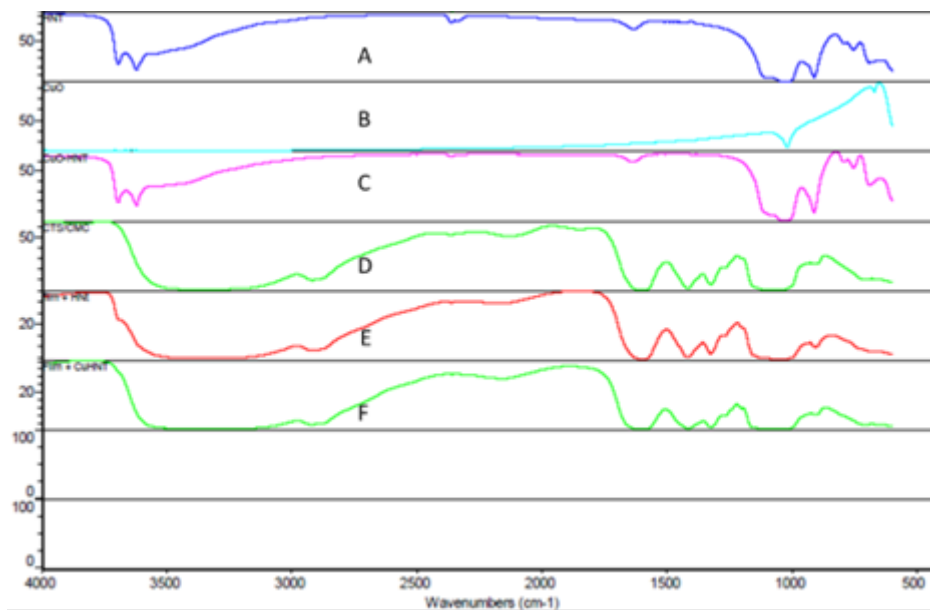
Figure 4-56 FTIR wavelengths of the materials and membranes A) HNT B) CuO C) CuO-HNT D) CTS/CMC E) CTS/CMC + HNT F) CTS/CMC + CuO-HNT

Scanning electron microscopy (SEM)

The morphology of the fabricated film membranes was assessed via FE-SEM with the results shown in Figure 4-57 and Figure 4-58. The CTS/CMC film is seen to have a smooth surface structure with no evidence of pores. The CTS/CMC membranes incorporated with HNT and CuO-HNTs nanofillers showed roughness of the surface of the membranes attributed to the poor dispersion and aggregation of the halloysite nanotubes. This non uniform dispersion caused the formation of voids. A stark difference in terms of surface homogeneity is evident when comparing the CTS/CMC film to the film membranes reinforced with HNTs and copper oxide HNTs due to the presence of rod-like structures on the latter membranes.
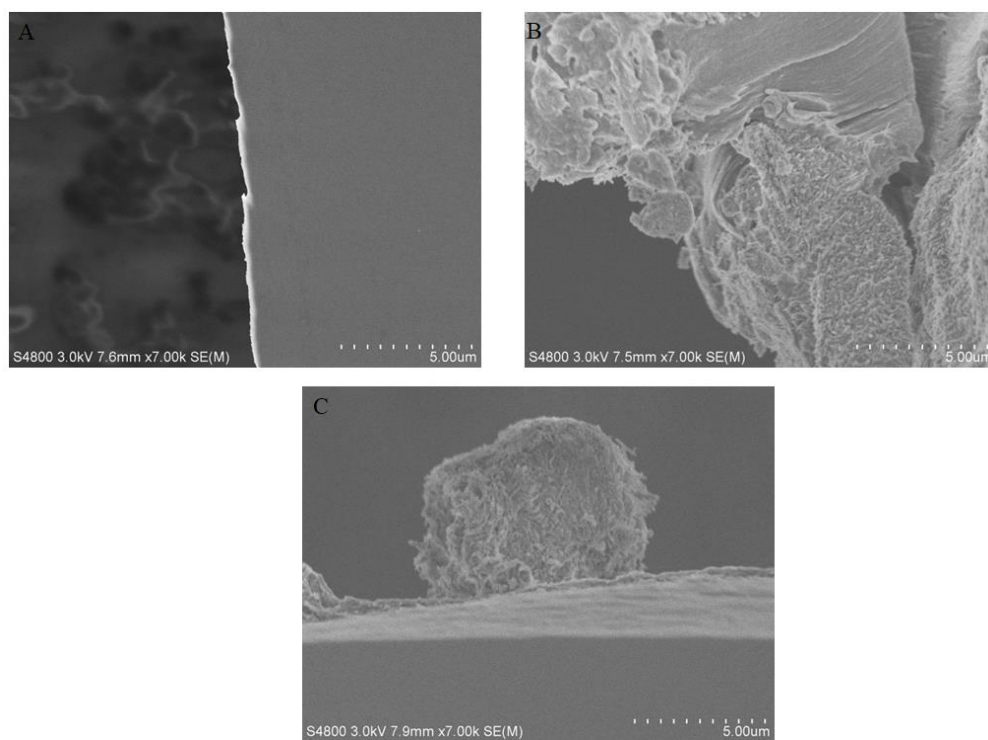
Figure 4-57 FE-SEM images of membranes at 7.00K magnification A) CTS/CMC film B) CTS/CMC film + HNT C) CTS/CMC film + CuHNT

The figure below further shows the film membranes reinforced with HNTs and Copper doped HNTs at a magnification of 20 k, with the nanotubes visibly embedded withing the membrane.
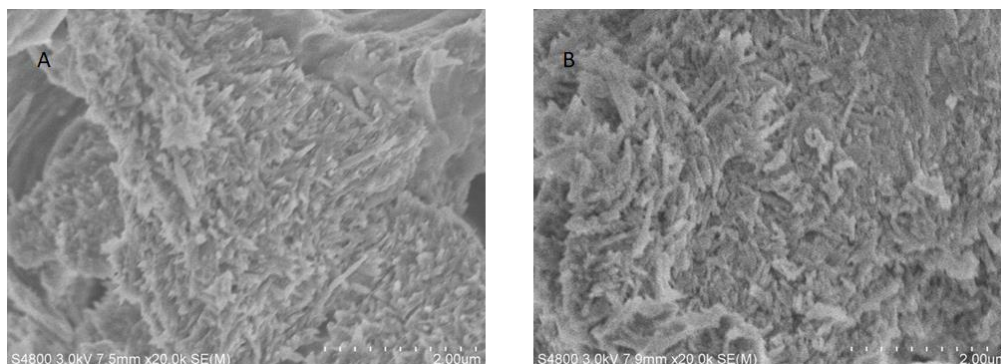
Figure 4-58 FE-SEM 20 k magnification images of chitosan-based film membranes reinforced with A) HNTs B) CuO-HNTs

Tensile strength test

Figure 4-59 below shows the relationship between the force applied and the resultant displacement of the individual chitosan-based membranes. The CTS/CMC experienced a first breakpoint when a force of 2.339 N resulted in a displacement of 0,776 mm. The membrane withstood further pulling force until complete breakage that required a force of 0.806 N at a displacement of 12.195. The breakpoints of membranes reinforced with 1% HNT and 5% HNT were observed when forces of 2.006 N and 2.419 N respectively were applied, resulting in displacements of 0.175 mm and 1.978 mm. Great pull forces of 4.094 N and 4.391 N were required to break the CTS/CMC + 1%

CuHNT and CTS/CMC + 5% CuHNT membranes at displacements of 1.176 mm and

1.778 mm respectively.
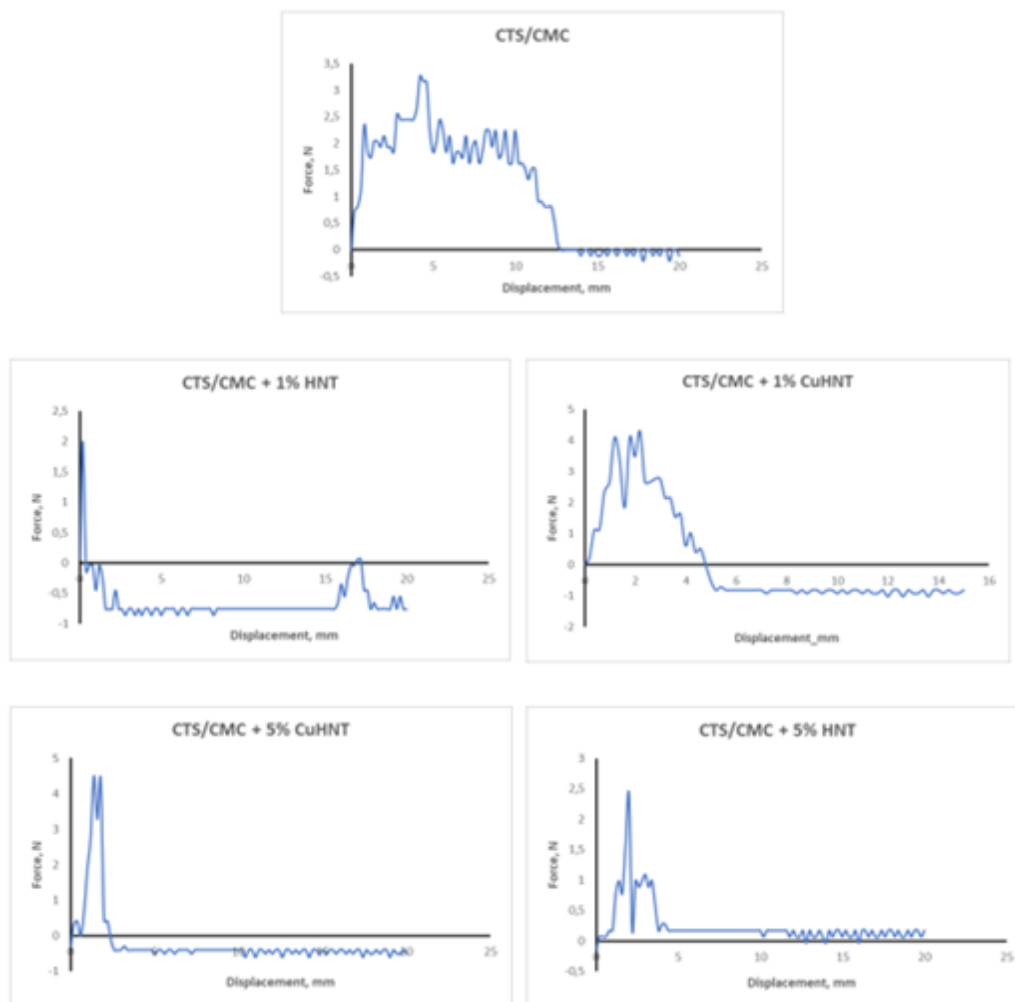
Figure 4-59 Graph showing the stress-displacement relationship of the various
membranes.

From the tensile strength assessment results in Figure 4-60 below a significant

difference ($p<0.05$) was seen between the CTS/CMC, CTS/CMC +1% CuHNT and

CTS/CMC + 5% CuHNT membranes. The highest tensile strength was exhibited by the

CTS/CMC + 5% CuHNT membrane. The addition of 1% CuHNT also significantly

increased the tensile strength of the membrane in comparison with the CTS/CMC

membrane. Figure 4-61 below shows the tensile strength measurements being taking on a Cellscale instrument.
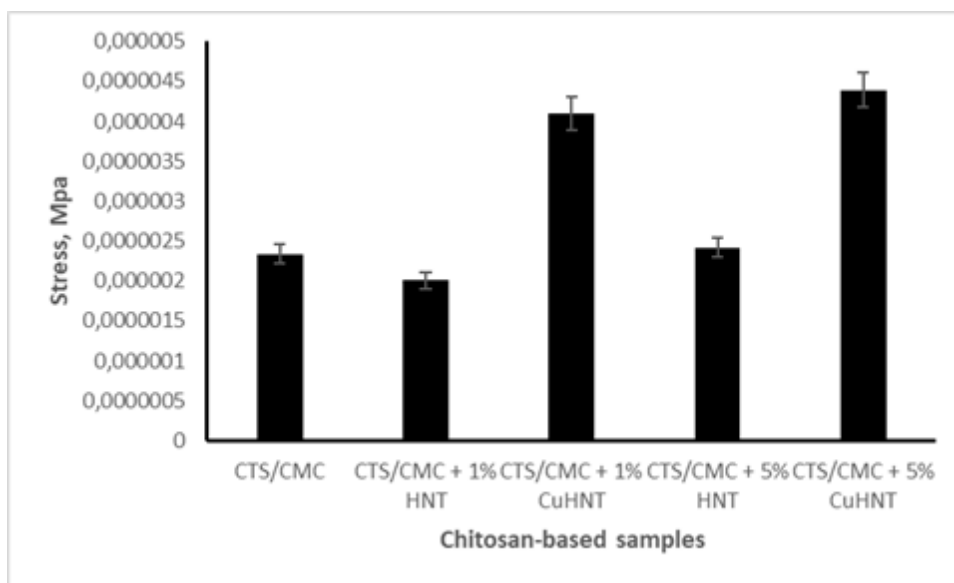
Figure 4-60 Graph showing the tensile strengths (σ) of the various membranes. N=3
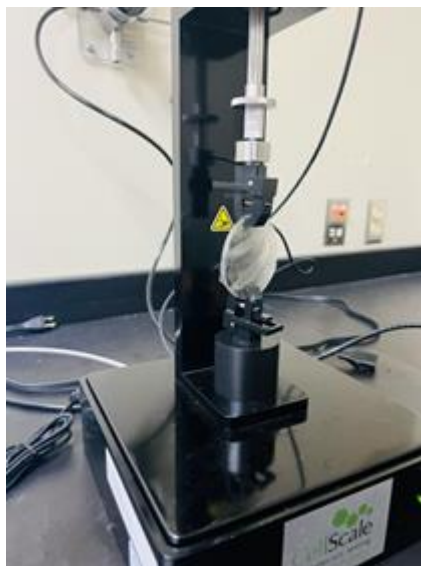
Figure 4-61 Tensile strengths (σ) testing using the various membranes on a Cellscale instrument.

Thermogravimetric analysis

The TGA plot for CTS/CMC membrane in figure 4-57A below showed an initial gradual 5% weight loss at approximately the 250 $^\circ$C temperature mark associated with the loss of adsorbed water mo;ecules. A second weight loss of 40% is observed from 250 $^\circ$C to 350 $^\circ$C attributed to the thermal degradation of the composite material. A 50% weight loss of the CTS/CMC film was seen at 475 $^\circ$C.
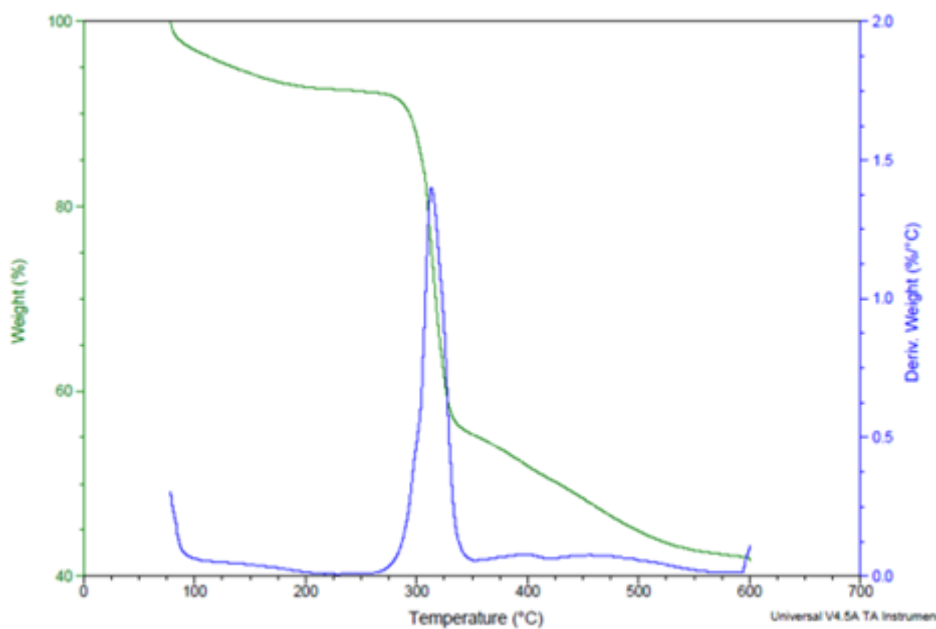
Figure 4-62 TGA analysis of CTS/CMC film membrane.

The film membranes reinforced with halloysites, and copper oxide doped halloysites showed similar TGA profiles as seen in Figure 4-63 and Figure 4-64 below. Further thermal degradation processes resulting in weight loss is observed at temperatures beyond 450 $^\circ$C and is characteristic of degradation of halloysites. With respect to the film membranes incorporated with halloysites and copper oxide halloysites, 30% and 40% weight losses were observed at 600 $^\circ$C respectively.
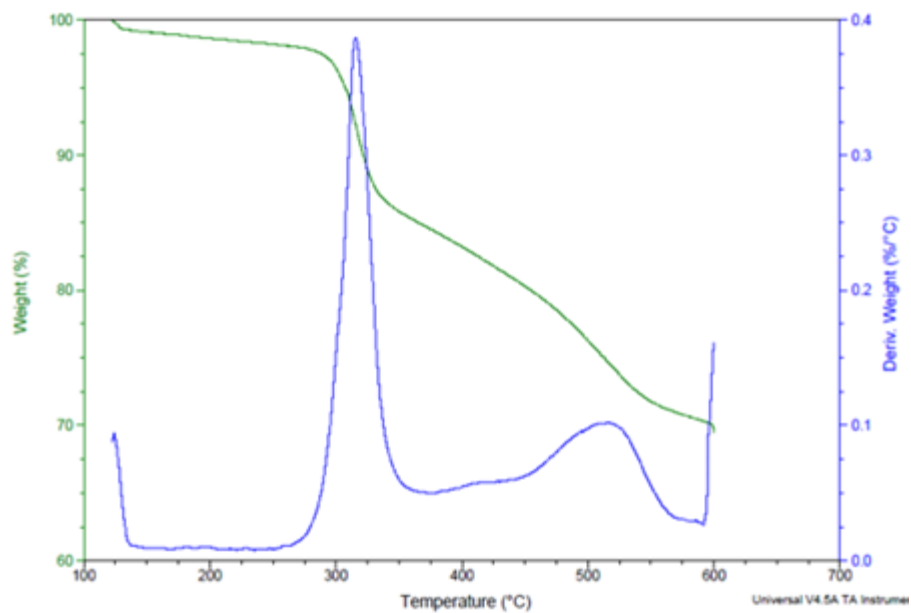
Figure 4-63 TGA analysis of film membrane reinforced with HNTs.
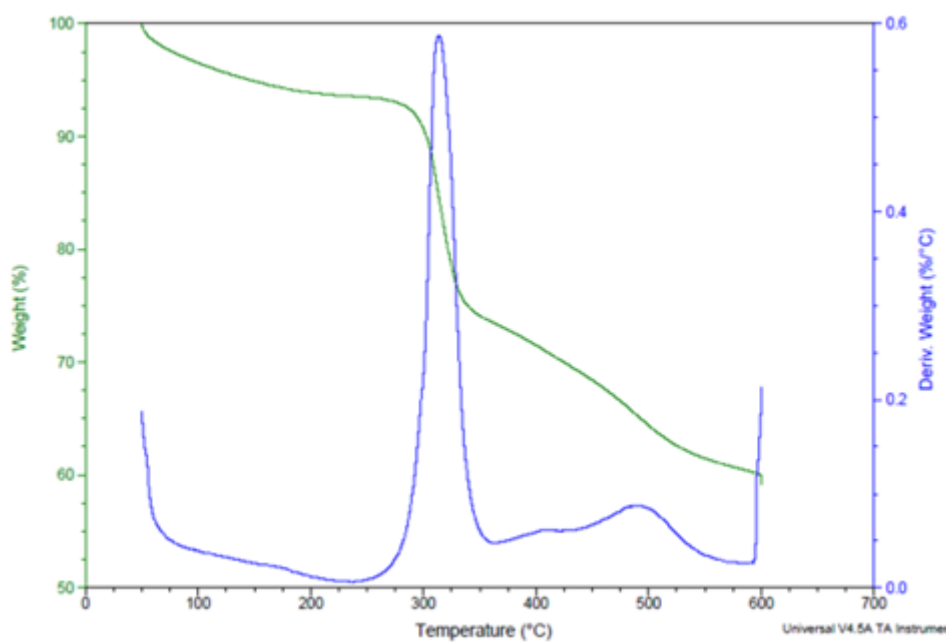
Figure 4-64 TGA analysis of film membrane reinforced with copper oxide HNTs.

Kirby Bauer Disk Susceptibility Test

The standard gentamicin disk inhibited the growth of *E. coli*, creating a zone of inhibition with a mean value of 1.9 ± 0.06 cm as seen in Figure 4-65 below. The CTS/CMC, CTS/CMC+1%HNT, CTS/CMC+1% CuHNT, CTS/CMC+5% HNT, and CTS/CMC+5%CuHNT film membranes did not exhibit antimicrobial activity against *E. coli*. However, the film membranes reinfoced with gentamicin sulphate loaded HNTs and copper oxide HNTs significantly inhibited bacterial growth in comparison with the samples without gentamicin sulphate. The highest zone of inhition, with a value of 2.37 ± 0.33 was seen in the film membrane incorporated with 1% copper oxide HNT loaded with gentamicin as seen in Figure 4-65 and Figure 4-66.
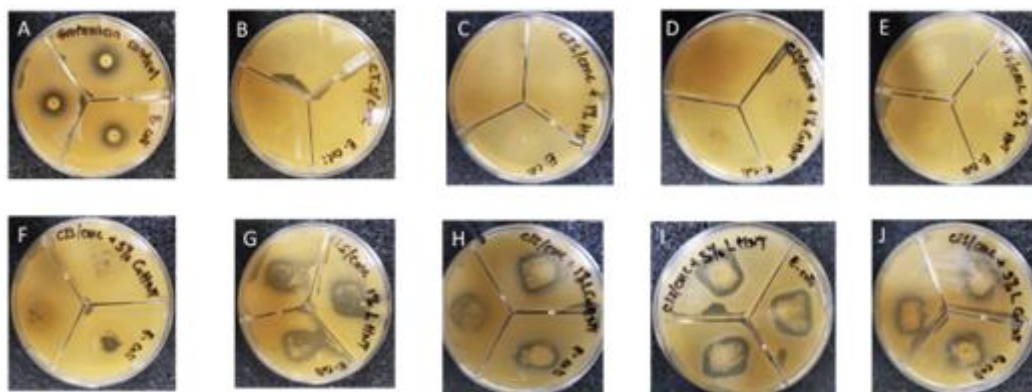
Figure 4-65 Image of *E. coli* bacteria culture plates with different membranes (A) Gentamicin control disc (B) CTS/CMC disc (C) CTS/CMC+1%HNT (D) CTS/CMC+1% CuHNT (E) CTS/CMC+5% HNT (F) CTS/CMC+5%CuHNT (G) CTS/CMC+1%LHNT (H) CTS/CMC+1%LCuHNT (I) CTS/CMC+5%LHNT (J) CTS/CMC+5%LCuHNT
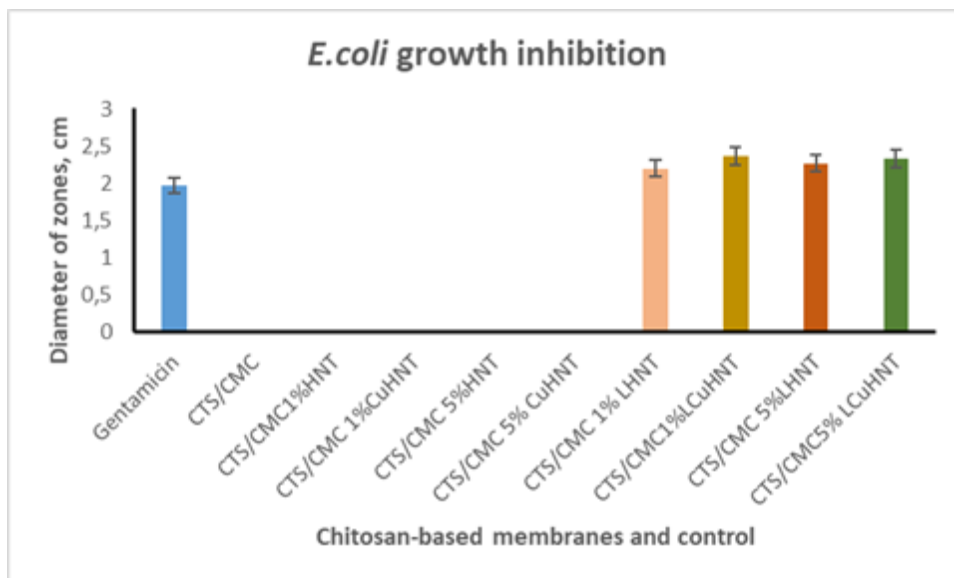
Figure 4-66 Graphical representation of *E. coli* susceptibility to different chitosan-based samples and gentamicin control disc. N=3

Similar to the test results using *E. coli*, the membranes showed antimicrobial properties against *S. aureus* as seen in figures Figure 4-67 and Figure 4-68 below. The gentamicin control disc significantly suppressed the growth of *S. aureus* compared to the film membranes with and without halloysites and copper oxide halloysites. The control disc resulted in a zone of inhibition with a mean value of 1.93 ± 0.11. The CTS/CMC, CTS/CMC+1%HNT, CTS/CMC+1% CuHNT, CTS/CMC+5% HNT, and CTS/CMC+5%CuHNT film membranes did not exhibit antimicrobial activity against *S. aureus*. The chitosan-based film membrane incorporated with 1% copper oxide HNT loaded with gentamicin had the highest zone of inhibition with a value of 2.77 ± 0.25 cm.
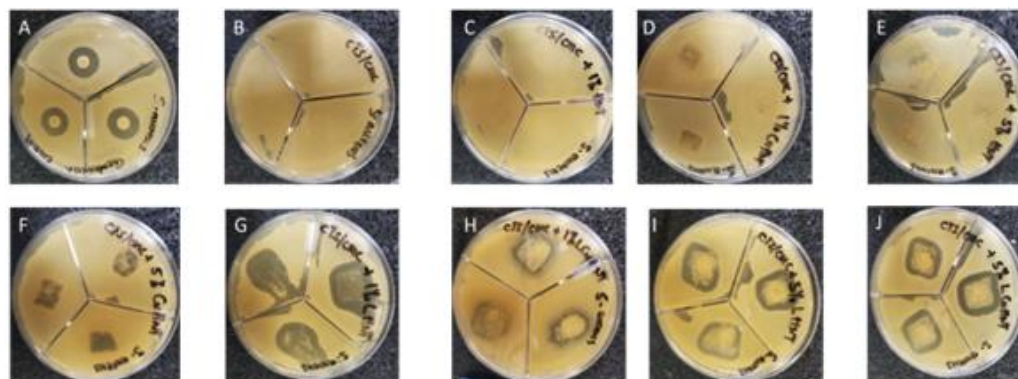
Figure 4-67 Image of *S. aureus* bacteria culture plates with different membranes (A) Gentamicin control disc (B) CTS/CMC disc (C) CTS/CMC+1%HNT (D) CTS/CMC+1% CuHNT (E) CTS/CMC+5% HNT (F) CTS/CMC+5%CuHNT (G) CTS/CMC+1%LHNT (H) CTS/CMC+1%LCuHNT (I) CTS/CMC+5%LHNT (J)CTS/CMC+5%LCuHNT
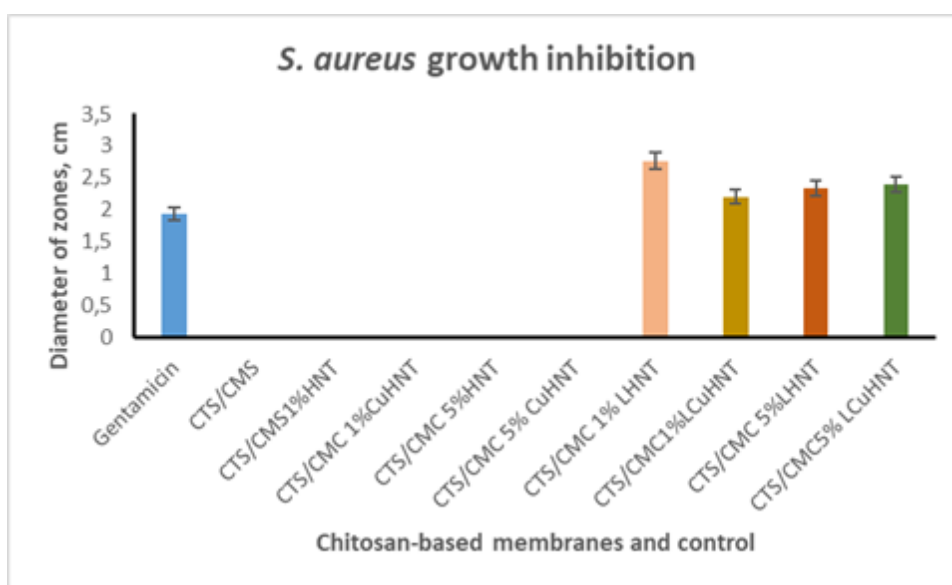
Figure 4-68 Graphical representation of *S. aureus* susceptibility to different chitosan-based samples and gentamicin control disc.

Cell proliferation assay

The results of the proliferation assay, which was carried out as a measure of cell viability post exposure to different chitosan-based film membranes in comparison to a control group of cells, are presented in Figure 4-69 below. A steady cell growth was seen in all groups of cells after day 1. This steady growth continued on days 2 and 3 but fibroblasts in the CTS/CMC +5% HNT and CTS/CMC +5% Cu HNT grew at a slightly higher rate. The growth rate in all groups plummeted on day 4 before steadily rising on day 5.
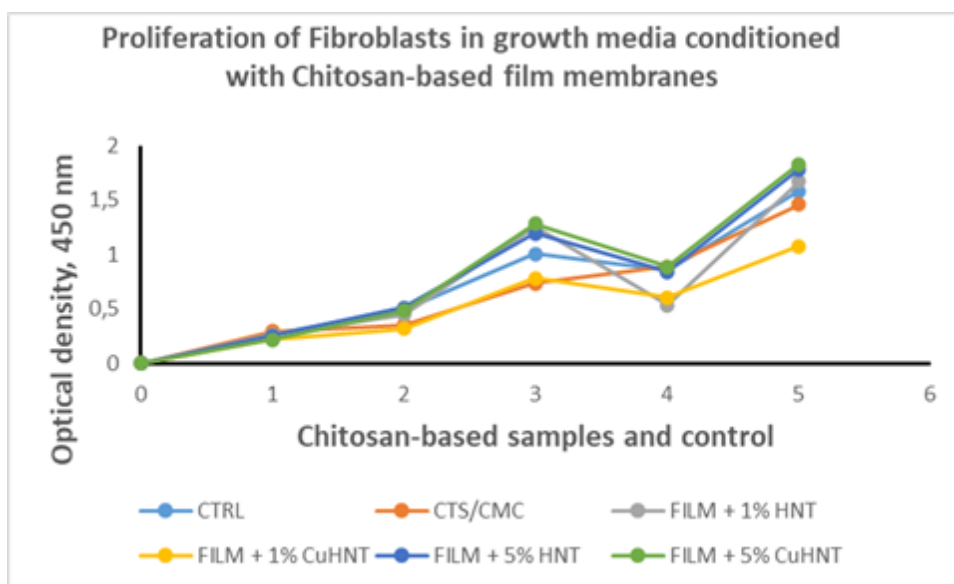
Figure 4-69 Proliferation assay using fibroblasts cultured in medium pre-conditioned with chitosan-based film membranes.

Cytotoxicity test (live/dead assay)

Results of the live/dead assay carried out as a measure of cytotoxicity is illustrated in Figure 4-70 below. From the results, a steady increase in number of cells in both the experimental and control groups is seen with increasing number of days. Viable cells are seen labeled in green with no dead cell (red) recorded in any of the groups. The

fibroblasts were seen to maintain their morphology over the 5-day period. A graph was

plotted quantifying the viability of the fibroblasts post exposure to the chitosan-based

film membranes, compared to the control group of cells cultured in complete growth

medium as seen in Figure 4-70 Overlay Images of Cytotoxicity test (live/dead assay)

using fibroblasts cultured for 1, 3 & 5 days in media pre-conditioned with chitosan-based

membranes. Live cells are stained green, dead cells are stained red.Figure 4-70. One way

ANOVA test showed no significant difference between the experimental and control

groups $p \geq 0.05$.
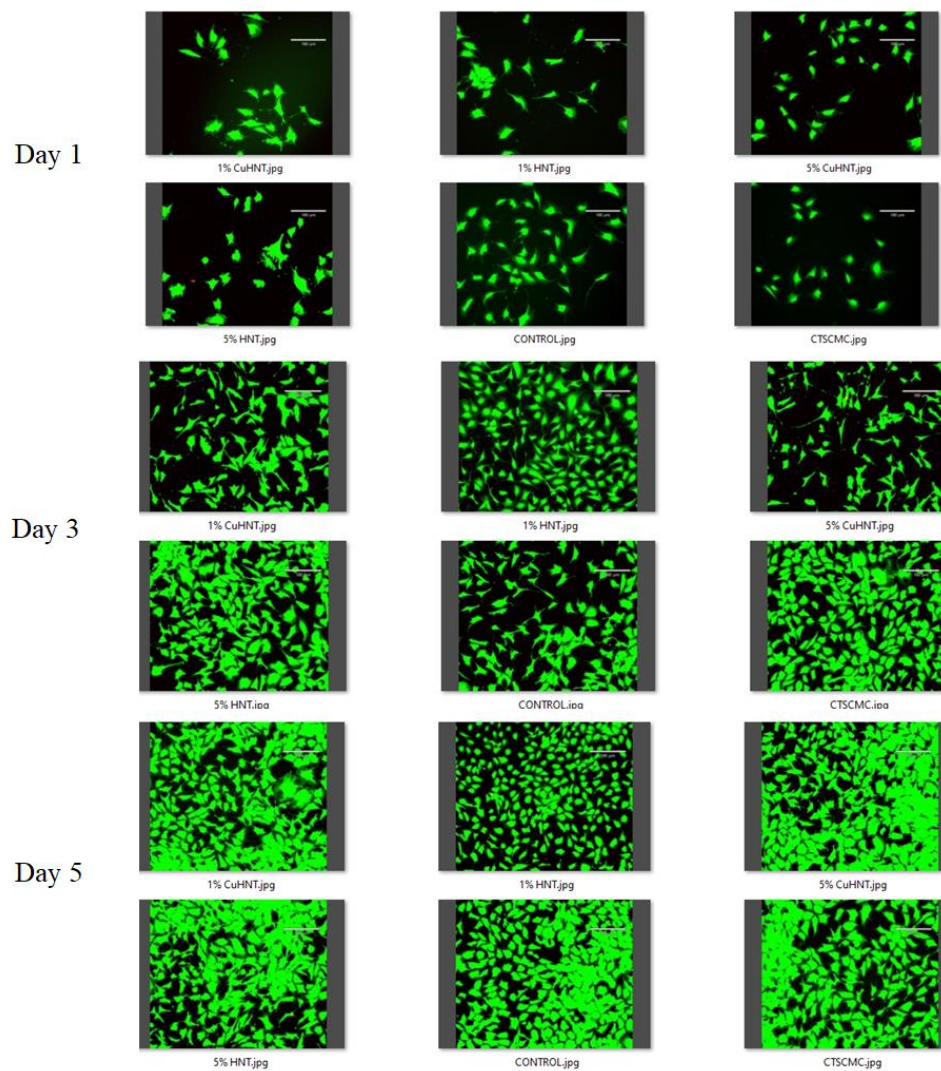
Figure 4-70 Overlay Images of Cytotoxicity test (live/dead assay) using fibroblasts cultured for 1, 3 & 5 days in media pre-conditioned with chitosan-based membranes. Live cells are stained green, dead cells are stained red.
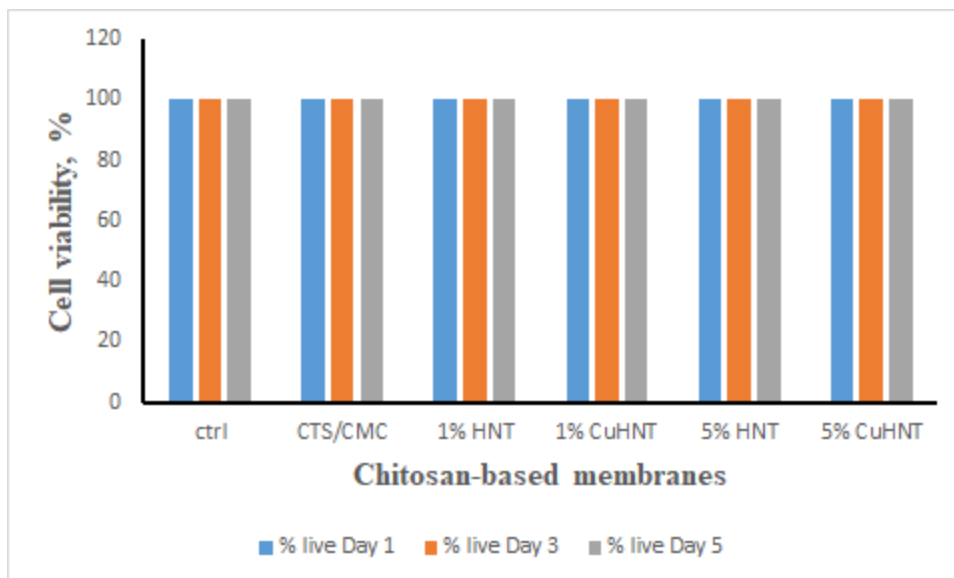
Figure 4-71 Graph showing viability of fibroblasts (live cells/total cell count) post treatment with medium pre-conditioned with chitosan-based membranes.

The results above showed that fibroblast cells remained 100% viable over the 5-day experimental period in the control group as well as the experimental group of cells cultured in medium pre-conditioned with the different chitosan-based membrane samples.

CHAPTER 5

DISCUSSION

5.1   Project 1: Fabrication and characterization of Sol-Gel Chitosan/Carboxymethylcellulose composite incorporated with zinc-doped halloysites (HNTs) and characterization of its physico-chemical properties.

The Sol-Gel composite fabrication method was shown to be a quick and effective way of fabricating chitosan-carboxymethyl cellulose composites, possibly reinforcing the composites with halloysites and zinc-doped halloysites for added functionality. The halloysite nanoparticles served the function of nanocarriers for the attachment of metal nanoparticles on the surface and loading antibiotics. The successful electrodeposition of zinc oxide nanoparticles on the surface of halloysites was demonstrated in this study and confirmed by the aggregation of particles seen on the SEM images. The results are in agreement with those obtained by Humayan and co-authors [119], [134]. These nanotubes could, therefore, effectively play the role of nanocarriers in various drug delivery systems, as demonstrated by this research and numerous other research works [122], [139]. In addition, the minimum inhibitory concentration test showed promising results as all the components used for the composite material fabrication exhibited some antibacterial properties by suppressing the growth of gram-positive and gram-negative bacteria, specifically *E. coli* and *S. aureus* at concentrations as low as 2 mg per microliter. The good swelling property demonstrated by the CTS/CMC composite points

the hydrophilic nature of carboxymethyl cellulose as well as the porous nature of the fabricated composite. Incorporation of HNTS and zinc coated HNTS acted as nanofillers, occupying the void and pores formed by the conjugate polymer materials, thus reducing the swelling properties and water content of the fabricated biomaterials.

Hydrogels used in biomedical research, including wound healing, mimic the extracellular matrix that supports cell growth and influences cell behavior [140]. With the core of the chitosan/carboxymethyl cellulose formulation being based on a gelation process, it was necessary to develop a firm gel that would influence cell function. The viscoelastic parameters of the fabricated composites are attributed to the strong electrostatic force of attraction between the mixture of chitosan and carboxymethyl cellulose molecules, with the 1:1 mixing ratio resulting in a strong gel ($G' \geq G''$). Porosity studies were carried out to assess how effectively the fabricated composite would regulate oxygen diffusion, an essential property of composite biomaterials. Porous materials are classified as microporous, mesoporous, and microporous based on the size of the pores they possess [51], [141].

The porosity of biomaterials is influenced by several factors, including pH, with stimuli-responsive hydrogels able to undergo conformational changes in response to cues. The significant increase in pore size and surface area post-incorporation of 5% HNT could be explained by the increased distribution of hollow halloysite within and on the outer perimeters of the fabricated composites. Additionally, increasing pH resulted in an increase in pore size and a decrease in total surface area. This can be explained by the lower degree of protonation of chitosan at higher pH, resulting in lesser electrostatic

interaction with carboxymethyl cellulose. The resulting porous material decreased in surface area, in agreement with results obtained in another study [142].

5.2   Project 2: In vitro assessment of the effect of the fabricated chitosan-based composite on wound closure and cell migration.

The antibacterial test generally showed promising results for the use of the fabricated composites in suppressing the growth of both gram positive and gram-negative bacteria. The Kirby-Bauer disc susceptibility test is based on the principle that antibiotics, in the form of discs placed on a lawn of bacteria grown on an agar plate, diffuse from the disc into the agar killing or repelling bacteria in close proximity to it [143]. This creates a zone which is void of any bacteria. The static nature of the CTS/CMC discs as well as discs incorporated in HNTs and ZnHNTs meant that there was no diffusion of metal ions or polymer molecules, hence no significant zones of inhibition were created. However, discs reinforced with halloysites, and zinc oxide doped halloysites loaded with antibiotics resulted in prominent zones of inhibition since the antibiotics diffused readily from the discs into the surrounding agar, thus suppressing bacterial growth.

Furthermore, the proliferation tests showed the continued growth of fibroblasts and mesenchymal stem cells in groups exposed to the different chitosan-based composites. This outcome points to the biocompatibility property of chitosan and carboxymethyl cellulose, as reported by other researchers [138], [144]. However, several other researchers have indicated the toxicity of zinc and halloysites to cells in either a concentration-dependent manner or depending on the buffer conditions of the cell growth medium [126], [135], [145]. This phenomenon is shown by the stagnated growth, and increased number of dead cells in media pre-conditioned with CTS/CMC composites

containing 1% and 5% zinc oxide doped halloysite nanotubes. The incorporation of zinc

nanoparticles therefore, negatively affected the viability of bacterial cells as well as

fibroblasts and mesenchymal stem cells. S-beta-galactosidase has been implicated as a

cell senescence marker in a number of studies [146]. One way ANOVA tests did not

reveal any significant difference between groups exposed to chitosan-based composites

and the unexposed control group.

5.3 Project 3: Biofabrication and material characterization of Chitosan/Carboxymethyl cellulose solution casted membranes for various biomedical applications.

The tensile strength test demonstrated that incorporating HNTs and CuO-HNTs

into the film membranes generally improved the strength of the materials compared to the

pure CTS/CMC film membranes. However, there is a possibility of observing an opposite

effect, possibly due to the non-uniform distribution of halloysite nanotubes within the

film membrane, which hinders the displacement movement of the film when the pulling

force is applied. This was demonstrated in the film membranes reinforced with 1% HNT

and 5% copper oxide HNT. In addition, increased HNT aggregate formation leading to

the reduction in HNT-polymer interfacial regions has been suggested by some studies

[136], [147].

The surface properties of the CTS/CMC film membrane incorporated with HNT

compared to that of the pure CTSCMC film membraned showed the random dispersion

of HNTs within the membrane layer. Increased concentrations of HNT could lead to

aggregation of these nanotubes, thus affecting the physico-chemical properties of the film

membranes [147]. The FTIR analysis confirmed the strong electrostatic attraction

between chitosan and carboxymethyl cellulose. Further reinforcement of the film membranes with halloysite and copper oxide doped halloysite nanotubes was confirmed by the presence of peaks attributed to the corresponding nanomaterials. These results conform to results obtained from similar studies [136], [147]. The thermal stability gained by the membranes after incorporation of HNTs and copper oxide doped halloysite nanotubes at different concentrations is explained by the possible formation of char which has been implicated in the reduced loss of volatiles [148]. Increased thermal stability of the CTS/CMC membranes incorporated with HNTs and CuO-HNTs due the suppression of heat and mass transfer by the lumen of HNTs in an entrapment mechanism is also plausible as mentioned by Du and co-authors [149]. Current research into wound care and implant development point to the increased need to suppress biofilm formation on implants as well as keeping wound surfaces void of infections throughout the healing process [150], [151]. The results of the antibacterial studies in this research demonstrate the plausibility of using HNTs as nanocarriers for sustained release of antibiotics for suppressing bacterial growth. These nanotubes also provide a point of attachment of metal oxide nanoparticles that play crucial roles in wound healing, tissue regeneration and other biomedical applications [152]. The fabrication of the CTS/CMC film membranes as well as membranes containing HNTs and CuO-HNTs proved to be biocompatible in 2D applications as seen in the results from the proliferation test, as well in cytotoxicity test. The proliferation rate drop seen in cells from all the groups is explained by the fact that fibroblast grow in a monolayer and upon reaching confluence, cell growth is stagnated as there is not enough space for cell expansion.

CHAPTER 6

CONCLUSIONS AND FUTURE WORK

Three distinct projects related to the study of chitosan-based composed used in wound healing and other biomedical applications were elaborated on in this dissertation. The conclusions drawn from the observed results and the future prospects are presented in this chapter.

6.1   Conclusions

6.1.1   Project 1:

In conclusion, a chitosan/carboxymethyl composite for wound healing and other biomedical applications was fabricated via a solution – gel method. The physico-chemical properties of the fabricated membrane were also studied. A composition ratio of one-part chitosan to one-part carboxymethyl cellulose was shown to be ideal for fabricating a composite with strong spreadability, porosity, and swelling properties. The incorporation of HNTs and zinc oxide doped HNTs significantly improved the thermal stability, pore size and total surface area of the freeze-dried composite, while relatively reducing the contact angle and ultimately, the spreadability of the fabricated composites.

6.1.2   Project 2:

In conclusion, the fabricated chitosan-based composites were assessed for their effect on wound closure and cell migration. It was established that the composites were biocompatible and facilitated the closure of an in-vitro wound model, though high

127

concentrations of incorporated zinc oxide doped halloysite nanoparticles conferred some degree of cytotoxicity to human dermal fibroblasts as well as mouse adipose tissue-derived mesenchymal stem cells.

6.1.3   Project 3:

In conclusion, pristine chitosan film membranes and membranes reinforced with HNTs, and copper oxide doped HNTs were successfully fabricated by solution casting method. The physico-chemical and cellular characteristics of the fabricated membranes were also studied. The incorporation of HNTs and CuO-HNTs improved the mechanical properties and the thermal stability of the film membranes significantly. The membranes were also seen to be biocompatible, making them ideal candidates for biomedical applications.

6.2   Future Work

Advances in technology has seen the development of tissue-mimicking platforms that are aimed at cultivating cells in a spatially organized three-dimensional microenvironment. The data obtained from this study indicate biocompatibility and non-cytotoxicity of the fabricated chitosan/carboxymethyl cellulose composites, but this property has not been fully investigated in association with the ECM. Future work will, therefore, be directed towards studying the effect of the chitosan-based composites on cells in vivo or in a 3D culture under the influence of the extra cellular matrix. This will give a better understanding of the role external cues play in molecular and cellular mechanisms of wound healing and tissue repair. Additionally, phenotypic markers of aging were studied in this work, with the exposure of cells to the fabricated chitosan-based composites not showing any significant effects to these markers. Future work will

seek to elucidate to role of genetic markers, particularly the role of the small Rho family GTPase CDC 42, implicated in various cellular activities including cell adhesion, cell aging and senescence-associated inflammation.

Elucidating the influence of the fabricated biomaterial composites on biological materials has potential for use in biomedical, bioengineering and tissue regeneration fields.

BIBLIOGRAPHY

[1]   M. Zagho, E. Hussein, and A. Elzatahry, "Recent Overviews in Functional Polymer Composites for Biomedical Applications," *Polymers*, vol. 10, no. 7, p. 739, Jul. 2018, doi: 10.3390/polym10070739.

[2]   S. Kunugi, "Proteins as Polymers and Polyelectrolytes," in *Encyclopedia of Polymeric Nanomaterials*, S. Kobayashi and K. Müllen, Eds., Berlin, Heidelberg: Springer, 2014, pp. 1–6. doi: 10.1007/978-3-642-36199-9_167-1.

[3]   B. Alberts, A. Johnson, J. Lewis, M. Raff, K. Roberts, and P. Walter, "The Shape and Structure of Proteins," *Mol. Biol. Cell 4th Ed.*, 2002, Accessed: Jan. 28, 2023. [Online]. Available: https://www.ncbi.nlm.nih.gov/books/NBK26830/

[4]   M. Brovold *et al.*, "Naturally-Derived Biomaterials for Tissue Engineering Applications," in *Novel Biomaterials for Regenerative Medicine*, H. J. Chun, K. Park, C.-H. Kim, and G. Khang, Eds., in Advances in Experimental Medicine and Biology, vol. 1077. Singapore: Springer Singapore, 2018, pp. 421–449. doi: 10.1007/978-981-13-0947-2_23.

[5]   J. A. Burdick and G. D. Prestwich, "Hyaluronic Acid Hydrogels for Biomedical Applications," *Adv. Mater.*, vol. 23, no. 12, pp. H41–H56, Mar. 2011, doi: 10.1002/adma.201003963.

[6]   Q. Li *et al.*, "Silver Inlaid with Gold Nanoparticle/Chitosan Wound Dressing Enhances Antibacterial Activity and Porosity, and Promotes Wound Healing," *Biomacromolecules*, vol. 18, no. 11, pp. 3766–3775, Nov. 2017, doi: 10.1021/acs.biomac.7b01180.

[7]   H. Seddiqi *et al.*, "Cellulose and its derivatives: towards biomedical applications," *Cellulose*, vol. 28, no. 4, pp. 1893–1931, Mar. 2021, doi: 10.1007/s10570-020-03674-w.

[8]   C. Frantz, K. M. Stewart, and V. M. Weaver, "The extracellular matrix at a glance," *J. Cell Sci.*, vol. 123, no. 24, pp. 4195–4200, Dec. 2010, doi: 10.1242/jcs.023820.

[9]   B. Blombäck and N. Bark, "Fibrinopeptides and fibrin gel structure," *Biophys. Chem.*, vol. 112, no. 2–3, pp. 147–151, Dec. 2004, doi: 10.1016/j.bpc.2004.07.013.

[10]   P. Sacco, F. Furlani, G. de Marzo, E. Marsich, S. Paoletti, and I. Donati, "Concepts for Developing Physical Gels of Chitosan and of Chitosan Derivatives," *Gels*, vol. 4, no. 3, p. 67, Aug. 2018, doi: 10.3390/gels4030067.

[11]   P. Sahariah *et al.*, "The Effect of Substituent, Degree of Acetylation and Positioning of the Cationic Charge on the Antibacterial Activity of Quaternary Chitosan Derivatives," *Mar. Drugs*, vol. 12, no. 8, pp. 4635–4658, Aug. 2014, doi: 10.3390/md12084635.

[12] N. R. Sudarshan, D. G. Hoover, and D. Knorr, "Antibacterial action of chitosan," *Food Biotechnol.*, vol. 6, no. 3, pp. 257–272, Jan. 1992, doi: 10.1080/08905439209549838.

[13] S. Jana and S. Jana, Eds., *Functional Chitosan: Drug Delivery and Biomedical Applications*. Singapore: Springer Singapore, 2019. doi: 10.1007/978-981-15-0263-7.

[14] A. B. Muley and R. S. Singhal, "Extension of postharvest shelf life of strawberries (Fragaria ananassa) using a coating of chitosan-whey protein isolate conjugate," *Food Chem.*, vol. 329, p. 127213, Nov. 2020, doi: 10.1016/j.foodchem.2020.127213.

[15] G. Romanazzi and M. Moumni, "Chitosan and other edible coatings to extend shelf life, manage postharvest decay, and reduce loss and waste of fresh fruits and vegetables," *Curr. Opin. Biotechnol.*, vol. 78, p. 102834, Dec. 2022, doi: 10.1016/j.copbio.2022.102834.

[16] I. Aranaz *et al.*, "Cosmetics and Cosmeceutical Applications of Chitin, Chitosan and Their Derivatives," *Polymers*, vol. 10, no. 2, p. 213, Feb. 2018, doi: 10.3390/polym10020213.

[17] A. Sionkowska, B. Kaczmarek, M. Michalska, K. Lewandowska, and S. Grabska, "Preparation and characterization of collagen/chitosan/hyaluronic acid thin films for application in hair care cosmetics," *Pure Appl. Chem.*, vol. 89, no. 12, pp. 1829–1839, Nov. 2017, doi: 10.1515/pac-2017-0314.

[18] P. K. Dutta, M. N. V. Ravikumar, and J. Dutta, "Chitin and Chitosan for versatile applications," *J. Macromol. Sci. Part C Polym. Rev.*, vol. 42, no. 3, pp. 307–354, Aug. 2002, doi: 10.1081/MC-120006451.

[19] E. Guibal, M. Van Vooren, B. A. Dempsey, and J. Roussy, "A Review of the Use of Chitosan for the Removal of Particulate and Dissolved Contaminants," *Sep. Sci. Technol.*, vol. 41, no. 11, pp. 2487–2514, Aug. 2006, doi: 10.1080/01496390600742807.

[20] L. Fan, C. Luo, Z. Lv, F. Lu, and H. Qiu, "Removal of Ag+ from water environment using a novel magnetic thiourea-chitosan imprinted Ag+," *J. Hazard. Mater.*, vol. 194, pp. 193–201, Oct. 2011, doi: 10.1016/j.jhazmat.2011.07.080.

[21] B. Liu, D. Wang, H. Li, Y. Xu, and L. Zhang, "As(III) removal from aqueous solution using α-Fe2O3 impregnated chitosan beads with As(III) as imprinted ions," *Desalination*, vol. 272, no. 1–3, pp. 286–292, May 2011, doi: 10.1016/j.desal.2011.01.034.

[22] Y. Wang *et al.*, "Synthesis of chitosan molecularly imprinted polymers for solid-phase extraction of methandrostenolone," *Carbohydr. Polym.*, vol. 101, pp. 517–523, Jan. 2014, doi: 10.1016/j.carbpol.2013.09.078.

[23] L. Giorno, E. Piacentini, and F. Bazzarelli, "Macroporous, Mesoporous, and Microporous Membranes," in *Encyclopedia of Membranes*, E. Drioli and L. Giorno, Eds., Berlin, Heidelberg: Springer Berlin Heidelberg, 2015, pp. 1–2. doi: 10.1007/978-3-642-40872-4_2244-1.

[24] G. Joshi, S. Naithani, V. K. Varshney, S. S. Bisht, V. Rana, and P. K. Gupta, "Synthesis and characterization of carboxymethyl cellulose from office waste paper: A greener approach towards waste management," *Waste Manag.*, vol. 38, pp. 33–40, Apr. 2015, doi: 10.1016/j.wasman.2014.11.015.

[25] H. Bidgoli, A. Zamani, A. Jeihanipour, and M. J. Taherzadeh, "Preparation of carboxymethyl cellulose superabsorbents from waste textiles," *Fibers Polym.*, vol. 15, no. 3, pp. 431–436, Mar. 2014, doi: 10.1007/s12221-014-0431-5.

[26] S. S. Bisht, K. K. Pandey, G. Joshi, and S. Naithani, "New route for carboxymethylation of cellulose: synthesis, structural analysis and properties".

[27] A. K. H.P.S *et al.*, "A review on chitosan-cellulose blends and nanocellulose reinforced chitosan biocomposites: Properties and their applications," *Carbohydr. Polym.*, vol. 150, pp. 216–226, Oct. 2016, doi: 10.1016/j.carbpol.2016.05.028.

[28] N. Verma, K. Pramanik, A. K. Singh, and A. Biswas, "Design of magnesium oxide nanoparticle incorporated carboxy methyl cellulose/poly vinyl alcohol composite film with novel composition for skin tissue engineering," *Mater. Technol.*, vol. 37, no. 8, pp. 706–716, Jul. 2022, doi: 10.1080/10667857.2021.1873634.

[29] S. Javanbakht, M. T. Nazeri, A. Shaabani, and M. Ghorbani, "Green one-pot synthesis of multicomponent-crosslinked carboxymethyl cellulose as a safe carrier for the gentamicin oral delivery," *Int. J. Biol. Macromol.*, vol. 164, pp. 2873–2880, Dec. 2020, doi: 10.1016/j.ijbiomac.2020.08.168.

[30] J. Sheikh, I. Bramhecha, and M. D. Teli, "Recycling of terry towel (cellulosic) waste into carboxymethyl cellulose (CMC) for textile printing," *Fibers Polym.*, vol. 16, no. 5, pp. 1113–1118, May 2015, doi: 10.1007/s12221-015-1113-7.

[31] A. Gregorova, N. Saha, T. Kitano, and P. Saha, "Hydrothermal effect and mechanical stress properties of carboxymethylcellulose based hydrogel food packaging," *Carbohydr. Polym.*, vol. 117, pp. 559–568, Mar. 2015, doi: 10.1016/j.carbpol.2014.10.009.

[32] Z. Cai, J. Wu, B. Du, and H. Zhang, "Impact of distribution of carboxymethyl substituents in the stabilizer of carboxymethyl cellulose on the stability of acidified milk drinks," *Food Hydrocoll.*, vol. 76, pp. 150–157, Mar. 2018, doi: 10.1016/j.foodhyd.2016.12.034.

[33] Md. S. Rahman *et al.*, "Recent Developments of Carboxymethyl Cellulose," *Polymers*, vol. 13, no. 8, p. 1345, Apr. 2021, doi: 10.3390/polym13081345.

[34] J. P. Jose and K. Joseph, "Advances in Polymer Composites: Macro- and Microcomposites – State of the Art, New Challenges, and Opportunities," in *Polymer Composites*, S. Thomas, J. Kuruvilla, S. K. Malhotra, K. Goda, and M. S. Sreekala, Eds., 1st ed.Wiley, 2012, pp. 1–16. doi: 10.1002/9783527645213.ch1.

[35] Purnomo, P. H. Setyarini, and D. Cahyandari, "Potential Natural Fiber-Reinforced Composite for Biomedical Application," *IOP Conf. Ser. Mater. Sci. Eng.*, vol. 494, p. 012018, Mar. 2019, doi: 10.1088/1757-899X/494/1/012018.

[36] A. M. Díez-Pascual, "Synthesis and Applications of Biopolymer Composites," *Int. J. Mol. Sci.*, vol. 20, no. 9, p. 2321, May 2019, doi: 10.3390/ijms20092321.

[37] J. L. Daristotle, "A review of the fundamental principles and applications of solution blow spinning," *J Daristotle M Behrens Sandler P KofinasA Rev. Fundam. Princ. Appl. Solut. Blow Spinn. ACS Appl Mater Interfaces*, vol. 8, no. 51, pp. 139–148, 2016.

[38] A. M. Behrens, "In Situ deposition of PLGA nanofibers via solution Bbow spinning," *M Behrens Al Sstu Depos. PLGA Nanofibers Solut. Bbow Spinn.*, vol. 3, no. 3, pp. 249–254, 2014.

[39] C. T. L. Zhang, S. Ramakrishna, and Z.-M. Huang, Eds., "Recent development of polymer nanofibers for biomedical and biotechnological applications," in *Y*, J. Mater. Sci. Mater. Med., vol. 16, no. 10: Recent development of polymer nanofibers for biomedical and biotechnological applications, 2005, pp. 933–946.

[40] R. Singh, S. Khan, S. M. Basu, M. Chauhan, N. Sarviya, and J. Giri, "Fabrication, Characterization, and Biological Evaluation of Airbrushed Gelatin Nanofibers," *ACS Appl. Bio Mater.*, vol. 2, no. 12, pp. 5340–5348, Dec. 2019, doi: 10.1021/acsabm.9b00636.

[41] K. Deshmukh, S. Sankaran, M. Basheer Ahamed, and S. K. Khadheer Pasha, "Biomedical Applications of Electrospun Polymer Composite Nanofibres," in *Polymer Nanocomposites in Biomedical Engineering*, K. K. Sadasivuni, D. Ponnamma, M. Rajan, B. Ahmed, and M. A. S. A. Al-Maadeed, Eds., in Lecture Notes in Bioengineering. Cham: Springer International Publishing, 2019, pp. 111–165. doi: 10.1007/978-3-030-04741-2_5.

[42] M. Liu, X.-P. Duan, Y.-M. Li, D.-P. Yang, and Y.-Z. Long, "Electrospun nanofibers for wound healing," *Mater. Sci. Eng. C*, vol. 76, pp. 1413–1423, Jul. 2017, doi: 10.1016/j.msec.2017.03.034.

[43] P. Agrawal and K. Pramanik, "Chitosan-poly(vinyl alcohol) nanofibers by free surface electrospinning for tissue engineering applications," *Tissue Eng. Regen. Med.*, vol. 13, no. 5, pp. 485–497, Oct. 2016, doi: 10.1007/s13770-016-9092-3.

[44] R. D. Farahani, D. Therriault, M. Dubé, S. Bodkhe, and M. Mahdavi, "6.13 Additive Manufacturing of Multifunctional Nanocomposites and Composites," in *Comprehensive Composite Materials II*, Elsevier, 2018, pp. 380–407. doi: 10.1016/B978-0-12-803581-8.10019-0.

[45] F. Wang *et al.*, "Fabrication and Characterization of PCL/HA Filament as a 3D Printing Material Using Thermal Extrusion Technology for Bone Tissue Engineering," *Polymers*, vol. 14, no. 4, p. 669, Feb. 2022, doi: 10.3390/polym14040669.

[46] I. Kong, K. Y. Tshai, and M. E. Hoque, "Manufacturing of Natural Fibre-Reinforced Polymer Composites by Solvent Casting Method," in *Manufacturing of Natural Fibre Reinforced Polymer Composites*, M. S. Salit, M. Jawaid, N. B. Yusoff, and M. E. Hoque, Eds., Cham: Springer International Publishing, 2015, pp. 331–349. doi: 10.1007/978-3-319-07944-8_16.

[47] O. WICHTERLE and D. LÍM, "Hydrophilic Gels for Biological Use," *Nature*, vol. 185, no. 4706, pp. 117–118, Jan. 1960, doi: 10.1038/185117a0.

[48] S. N. Dobić, J. M. Filipović, and S. Lj. Tomić, "Synthesis and characterization of poly(2-hydroxyethyl methacrylate/itaconic acid/poly(ethylene glycol) dimethacrylate) hydrogels," *Chem. Eng. J.*, vol. 179, pp. 372–380, Jan. 2012, doi: 10.1016/j.cej.2011.10.083.

[49] J.-Y. Lee *et al.*, "Enhanced bone formation by controlled growth factor delivery from chitosan-based biomaterials," *J. Control. Release Off. J. Control. Release Soc.*, vol. 78, no. 1–3, pp. 187–197, Jan. 2002, doi: 10.1016/s0168-3659(01)00498-9.

[50] K. Y. Lee, M. C. Peters, K. W. Anderson, and D. J. Mooney, "Controlled growth factor release from synthetic extracellular matrices," *Nature*, vol. 408, no. 6815, pp. 998–1000, Dec. 2000, doi: 10.1038/35050141.

[51] T. P. Richardson, M. C. Peters, A. B. Ennett, and D. J. Mooney, "Polymeric system for dual growth factor delivery," *Nat. Biotechnol.*, vol. 19, no. 11, pp. 1029–1034, Nov. 2001, doi: 10.1038/nbt1101-1029.

[52] W. Zhu and J. Ding, "Synthesis and characterization of a redox-initiated, injectable, biodegradable hydrogel," *J. Appl. Polym. Sci.*, vol. 99, no. 5, pp. 2375–2383, Mar. 2006, doi: 10.1002/app.22674.

[53] Y. Yeo and D. S. Kohane, "Polymers in the prevention of peritoneal adhesions," *Eur. J. Pharm. Biopharm. Off. J. Arbeitsgemeinschaft Pharm. Verfahrenstechnik EV*, vol. 68, no. 1, pp. 57–66, Jan. 2008, doi: 10.1016/j.ejpb.2007.03.027.

[54] A. Baral *et al.*, "Assembly of an injectable noncytotoxic peptide-based hydrogelator for sustained release of drugs," *Langmuir ACS J. Surf. Colloids*, vol. 30, no. 3, pp. 929–936, Jan. 2014, doi: 10.1021/la4043638.

[55] V. Guarnizo-Herrero, C. Torrado-Salmerón, N. S. Torres Pabón, G. Torrado Durán, J. Morales, and S. Torrado-Santiago, "Study of Different Chitosan/Sodium Carboxymethyl Cellulose Proportions in the Development of Polyelectrolyte Complexes for the Sustained Release of Clarithromycin from Matrix Tablets," *Polymers*, vol. 13, no. 16, p. 2813, Aug. 2021, doi: 10.3390/polym13162813.

[56] N. B. Gol, P. R. Patel, and T. V. R. Rao, "Improvement of quality and shelf-life of strawberries with edible coatings enriched with chitosan," *Postharvest Biol. Technol.*, vol. 85, pp. 185–195, Nov. 2013, doi: 10.1016/j.postharvbio.2013.06.008.

[57] S. A. Akintelu, A. S. Folorunso, F. A. Folorunso, and A. K. Oyebamiji, "Green synthesis of copper oxide nanoparticles for biomedical application and environmental remediation," *Heliyon*, vol. 6, no. 7, p. e04508, Jul. 2020, doi: 10.1016/j.heliyon.2020.e04508.

[58] Q. Maqbool *et al.*, "Green fabricated CuO nanobullets via Olea europaea leaf extract shows auspicious antimicrobial potential," *IET Nanobiotechnol.*, vol. 11, no. 4, pp. 463–468, 2017, doi: 10.1049/iet-nbt.2016.0125.

[59] R. I. Mahmood *et al.*, "Biosynthesis of copper oxide nanoparticles mediated Annona muricata as cytotoxic and apoptosis inducer factor in breast cancer cell lines," *Sci. Rep.*, vol. 12, no. 1, Art. no. 1, Sep. 2022, doi: 10.1038/s41598-022-20360-y.

[60] J. Salvo and C. Sandoval, "Role of copper nanoparticles in wound healing for chronic wounds: literature review," *Burns Trauma*, vol. 10, p. tkab047, Jan. 2022, doi: 10.1093/burnst/tkab047.

[61] C. Sandoval, G. Ríos, N. Sepúlveda, J. Salvo, V. Souza-Mello, and J. Farías, "Effectiveness of Copper Nanoparticles in Wound Healing Process Using In Vivo and In Vitro Studies: A Systematic Review," *Pharmaceutics*, vol. 14, no. 9, p. 1838, Aug. 2022, doi: 10.3390/pharmaceutics14091838.

[62] M. B. Gawande *et al.*, "Cu and Cu-Based Nanoparticles: Synthesis and Applications in Catalysis," *Chem. Rev.*, vol. 116, no. 6, pp. 3722–3811, Mar. 2016, doi: 10.1021/acs.chemrev.5b00482.

[63] J. Chou, J. Hao, H. Hatoyama, B. Ben-Nissan, B. Milthorpe, and M. Otsuka, "Effect of biomimetic zinc-containing tricalcium phosphate (Zn-TCP) on the growth and osteogenic differentiation of mesenchymal stem cells: Effect of Zn-

TCP on growth and osteogenic differentiation of MSCs," *J. Tissue Eng. Regen. Med.*, vol. 9, no. 7, pp. 852–858, Jul. 2015, doi: 10.1002/term.1901.

[64] M.-Y. Moon, H. J. Kim, B. Y. Choi, M. Sohn, T. N. Chung, and S. W. Suh, "Zinc Promotes Adipose-Derived Mesenchymal Stem Cell Proliferation and Differentiation towards a Neuronal Fate," *Stem Cells Int.*, vol. 2018, p. 5736535, 2018, doi: 10.1155/2018/5736535.

[65] M. Premanathan, K. Karthikeyan, K. Jeyasubramanian, and G. Manivannan, "Selective toxicity of ZnO nanoparticles toward Gram-positive bacteria and cancer cells by apoptosis through lipid peroxidation," *Nanomedicine Nanotechnol. Biol. Med.*, vol. 7, no. 2, pp. 184–192, Apr. 2011, doi: 10.1016/j.nano.2010.10.001.

[66] A. Sirelkhatim *et al.*, "Review on Zinc Oxide Nanoparticles: Antibacterial Activity and Toxicity Mechanism," *Nano-Micro Lett.*, vol. 7, no. 3, pp. 219–242, 2015, doi: 10.1007/s40820-015-0040-x.

[67] amica panja, "Silver Nanoparticles – A Review," *Eurasian J. Med. Oncol.*, 2021, doi: 10.14744/ejmo.2021.59602.

[68] S. Gurunathan *et al.*, "Biosynthesis, purification and characterization of silver nanoparticles using Escherichia coli," *Colloids Surf. B Biointerfaces*, vol. 74, no. 1, pp. 328–335, Nov. 2009, doi: 10.1016/j.colsurfb.2009.07.048.

[69] P. Banerjee, M. Satapathy, A. Mukhopahayay, and P. Das, "Leaf extract mediated green synthesis of silver nanoparticles from widely available Indian plants: synthesis, characterization, antimicrobial property and toxicity analysis," *Bioresour. Bioprocess.*, vol. 1, no. 1, p. 3, Dec. 2014, doi: 10.1186/s40643-014-0003-y.

[70] K. Raja, A. Saravanakumar, and R. Vijayakumar, "Efficient synthesis of silver nanoparticles from Prosopis juliflora leaf extract and its antimicrobial activity using sewage," *Spectrochim. Acta. A. Mol. Biomol. Spectrosc.*, vol. 97, pp. 490–494, Nov. 2012, doi: 10.1016/j.saa.2012.06.038.

[71] M. Goudarzi, N. Mir, M. Mousavi-Kamazani, S. Bagheri, and M. Salavati-Niasari, "Biosynthesis and characterization of silver nanoparticles prepared from two novel natural precursors by facile thermal decomposition methods," *Sci. Rep.*, vol. 6, no. 1, p. 32539, Sep. 2016, doi: 10.1038/srep32539.

[72] G. Pletikapić, V. Žutić, I. Vinković Vrček, and V. Svetličić, "Atomic force microscopy characterization of silver nanoparticles interactions with marine diatom cells and extracellular polymeric substance," *J. Mol. Recognit. JMR*, vol. 25, no. 5, pp. 309–317, May 2012, doi: 10.1002/jmr.2177.

[73] H. I. O. Gomes, C. S. M. Martins, and J. A. V. Prior, "Silver Nanoparticles as Carriers of Anticancer Drugs for Efficient Target Treatment of Cancer Cells," *Nanomaterials*, vol. 11, no. 4, p. 964, Apr. 2021, doi: 10.3390/nano11040964.

[74] T. Bruna, F. Maldonado-Bravo, P. Jara, and N. Caro, "Silver Nanoparticles and Their Antibacterial Applications," *Int. J. Mol. Sci.*, vol. 22, no. 13, p. 7202, Jul. 2021, doi: 10.3390/ijms22137202.

[75] K. K. Y. Wong *et al.*, "Further Evidence of the Anti-inflammatory Effects of Silver Nanoparticles," *ChemMedChem*, vol. 4, no. 7, pp. 1129–1135, Jul. 2009, doi: 10.1002/cmdc.200900049.

[76] D. Rawtani and Y. K. Agrawal, "Multifarious applications of halloysite nanotubes: A Review".

[77] E. Joussein, "Halloysite clay minerals---a review,'' Clay Minerals," *E Joussein Petit J Churchm. B Theng Righi B Delvaux Halloysite Clay Miner.--- Rev. Clay Min.*, vol. 40, no. 4, pp. 383–426, 2005.

[78] E. Abdullayev, R. Price, D. Shchukin, and Y. Lvov, "Halloysite tubes as nanocontainers for anticorrosion coating with benzotriazole," *ACS Appl. Mater. Interfaces*, vol. 1, no. 7, pp. 1437–1443, Jul. 2009, doi: 10.1021/am9002028.

[79] K. A. Askar and K. Song, "Epoxy-Based Multifunctional Nanocomposites," in *Polymer-Based Multifunctional Nanocomposites and Their Applications*, Elsevier, 2019, pp. 111–135. doi: 10.1016/B978-0-12-815067-2.00004-4.

[80] Y. M. Lvov, D. G. Shchukin, H. Möhwald, and R. R. Price, "Halloysite clay nanotubes for controlled release of protective agents," *ACS Nano*, vol. 2, no. 5, pp. 814–820, May 2008, doi: 10.1021/nn800259q.

[81] C. Duce, V. D. Porta, E. Bramanti, B. Campanella, A. Spepi, and M. R. Tiné, "Loading of halloysite nanotubes with BSA, α-Lac and β-Lg: a Fourier transform infrared spectroscopic and thermogravimetric study," *Nanotechnology*, vol. 28, no. 5, p. 055706, Dec. 2016, doi: 10.1088/1361-6528/28/5/055706.

[82] J. M. Falcón, T. Sawczen, and I. V. Aoki, "Dodecylamine-Loaded Halloysite Nanocontainers for Active Anticorrosion Coatings," *Front. Mater.*, vol. 2, Nov. 2015, doi: 10.3389/fmats.2015.00069.

[83] Y. Fu, D. Zhao, W. Wang, and Y. Lvov, "Aging Resistant Elastomer Reinforcement by Antioxidant Loaded Clay Nanotubes," *IOP Conf. Ser. Mater. Sci. Eng.*, vol. 64, p. 012047, Aug. 2014, doi: 10.1088/1757-899X/64/1/012047.

[84] L. Lisuzzo, G. Cavallaro, P. Pasbakhsh, S. Milioto, and G. Lazzara, "Why does vacuum drive to the loading of halloysite nanotubes? The key role of water confinement," *J. Colloid Interface Sci.*, vol. 547, pp. 361–369, Jul. 2019, doi: 10.1016/j.jcis.2019.04.012.

[85] A. Humayun, Y. Luo, and D. K. Mills, "Electrophoretic Deposition of Gentamicin-Loaded ZnHNTs-Chitosan on Titanium," *Coatings*, vol. 10, no. 10, p. 944, Sep. 2020, doi: 10.3390/coatings10100944.

[86] Y. Yang, Y. Chen, F. Leng, L. Huang, Z. Wang, and W. Tian, "Recent Advances on Surface Modification of Halloysite Nanotubes for Multifunctional Applications," *Appl. Sci.*, vol. 7, no. 12, Art. no. 12, Dec. 2017, doi: 10.3390/app7121215.

[87] H. Ismail, P. Pasbakhsh, M. N. Ahmad Fauzi, and A. Abu Bakar, "The Effect of Halloysite Nanotubes as a Novel Nanofiller on Curing Behaviour, Mechanical and Microstructural Properties of Ethylene Propylene Diene Monomer (EPDM) Nanocomposites," *Polym.-Plast. Technol. Eng.*, vol. 48, no. 3, pp. 313–323, Feb. 2009, doi: 10.1080/03602550802675736.

[88] M. Y. Saleh, N. Prajapati, M. A. DeCoster, and Y. Lvov, "Tagged Halloysite Nanotubes as a Carrier for Intercellular Delivery in Brain Microvascular Endothelium," *Front. Bioeng. Biotechnol.*, vol. 8, 2020, Accessed: Jan. 31, 2023. [Online]. Available: https://www.frontiersin.org/articles/10.3389/fbioe.2020.00451

[89] Y. Zhang, R. Gao, M. Liu, C. Yan, and A. Shan, "Adsorption of modified halloysite nanotubes *in vitro* and the protective effect in rats exposed to zearalenone," *Arch. Anim. Nutr.*, vol. 68, no. 4, pp. 320–335, Jul. 2014, doi: 10.1080/1745039X.2014.927710.

[90]   M. Massaro, R. Noto, and S. Riela, "Halloysite Nanotubes: Smart Nanomaterials in Catalysis," *Catalysts*, vol. 12, no. 2, p. 149, Jan. 2022, doi: 10.3390/catal12020149.

[91]   D. Mills, "Biocompatibility of halloysite clay nanotubes in a rat dermal model (87.4)," *FASEB J.*, vol. 28, no. S1, p. 87.4, 2014, doi: 10.1096/fasebj.28.1_supplement.87.4.

[92]   D. Sawicka, L. Zapor, L. Chojnacka-Puchta, and K. Miranowicz-Dzierzawska, "The in vitro toxicity evaluation of halloysite nanotubes (HNTs) in human lung cells," *Toxicol. Res.*, vol. 37, no. 3, pp. 301–310, Jul. 2021, doi: 10.1007/s43188-020-00062-1.

[93]   V. Vergaro *et al.*, "Cytocompatibility and uptake of halloysite clay nanotubes," *Biomacromolecules*, vol. 11, no. 3, pp. 820–826, Mar. 2010, doi: 10.1021/bm9014446.

[94]   A. Masoud and D. K. Mills, "Harnessing antibacterial properties of biomaterials for fabricating wound healing patch," *FASEB J.*, vol. 36, no. S1, 2022, doi: 10.1096/fasebj.2022.36.S1.R3615.

[95]   C. Liu *et al.*, "Enhancement of mechanical properties of poly(vinyl chloride) with polymethyl methacrylate-grafted halloysite nanotube," *Express Polym. Lett.*, vol. 5, no. 7, pp. 591–603, 2011, doi: 10.3144/expresspolymlett.2011.58.

[96]   C. Li, J. Liu, X. Qu, B. Guo, and Z. Yang, "Polymer-modified halloysite composite nanotubes," *J. Appl. Polym. Sci.*, vol. 110, no. 6, pp. 3638–3646, Dec. 2008, doi: 10.1002/app.28879.

[97]   J. C. Nicholson, J. A. Weisman, C. J. Boyer, C. G. Wilson, and D. K. Mills, "Dry Sintered Metal Coating of Halloysite Nanotubes," *Appl. Sci.*, vol. 6, no. 9, Art. no. 9, Sep. 2016, doi: 10.3390/app6090265.

[98]   U. Jammalamadaka, K. Tappa, J. A. Weisman, J. C. Nicholson, and D. K. Mills, "Effect of barium-coated halloysite nanotube addition on the cytocompatibility, mechanical and contrast properties of poly(methyl methacrylate) cement," *Nanotechnol. Sci. Appl.*, vol. 10, pp. 105–114, 2017, doi: 10.2147/NSA.S131412.

[99]   A. W. McFarland, A. Elumalai, C. C. Miller, A. Humayun, and D. K. Mills, "Effectiveness and Applications of a Metal-Coated HNT/Polylactic Acid Antimicrobial Filtration System," *Polymers*, vol. 14, no. 8, p. 1603, Apr. 2022, doi: 10.3390/polym14081603.

[100]   A. Humayun and D. Mills, "Voltage regulated electrophoretic deposition of silver nanoparticles on halloysite nanotubes," *Results Mater.*, vol. 7, p. 100112, Sep. 2020, doi: 10.1016/j.rinma.2020.100112.

[101]   S. Mellouk *et al.*, "Intercalation of halloysite from Djebel Debagh (Algeria) and adsorption of copper ions," *Appl. Clay Sci.*, vol. 44, no. 3, pp. 230–236, May 2009, doi: 10.1016/j.clay.2009.02.008.

[102]   V. A. Vinokurov *et al.*, "Formation of metal clusters in halloysite clay nanotubes," *Sci. Technol. Adv. Mater.*, vol. 18, no. 1, pp. 147–151, Feb. 2017, doi: 10.1080/14686996.2016.1278352.

[103]   W. Yang *et al.*, "In-situ grown Ag on magnetic halloysite nanotubes in scaffolds: Antibacterial, biocompatibility and mechanical properties," *Ceram. Int.*, vol. 47, no. 23, pp. 32756–32765, Dec. 2021, doi: 10.1016/j.ceramint.2021.08.172.

[104] G. Kiani, "High removal capacity of silver ions from aqueous solution onto Halloysite nanotubes," *Appl. Clay Sci.*, vol. 90, pp. 159–164, Mar. 2014, doi: 10.1016/j.clay.2014.01.010.

[105] A. C. de O. Gonzalez, T. F. Costa, Z. de A. Andrade, and A. R. A. P. Medrado, "Wound healing - A literature review," *An. Bras. Dermatol.*, vol. 91, no. 5, pp. 614–620, 2016, doi: 10.1590/abd1806-4841.20164741.

[106] M. Rodrigues, N. Kosaric, C. A. Bonham, and G. C. Gurtner, "Wound Healing: A Cellular Perspective," *Physiol. Rev.*, vol. 99, no. 1, pp. 665–706, Jan. 2019, doi: 10.1152/physrev.00067.2017.

[107] J. R. Silva, B. Burger, C. M. C. Kühl, T. Candreva, M. B. P. dos Anjos, and H. G. Rodrigues, "Wound Healing and Omega-6 Fatty Acids: From Inflammation to Repair," *Mediators Inflamm.*, vol. 2018, pp. 1–17, 2018, doi: 10.1155/2018/2503950.

[108] J. G. Pool, "Normal hemostatic mechanisms: a review," *Am. J. Med. Technol.*, vol. 43, no. 8, pp. 776–780, Aug. 1977.

[109] K. L. Kaplan, M. J. Broekman, A. Chernoff, G. R. Lesznik, and M. Drillings, "Platelet alpha-granule proteins: studies on release and subcellular localization," *Blood*, vol. 53, no. 4, pp. 604–618, Apr. 1979.

[110] G. S. Hotamisligil, "Inflammation, metaflammation and immunometabolic disorders," *Nature*, vol. 542, no. 7640, Art. no. 7640, Feb. 2017, doi: 10.1038/nature21363.

[111] M. Dovedytis, Z. J. Liu, and S. Bartlett, "Hyaluronic acid and its biomedical applications: A review," *Eng. Regen.*, vol. 1, pp. 102–113, 2020, doi: 10.1016/j.engreg.2020.10.001.

[112] L. A. DiPietro, P. J. Polverini, S. M. Rahbe, and E. J. Kovacs, "Modulation of JE/MCP-1 expression in dermal wound repair.," *Am. J. Pathol.*, vol. 146, no. 4, pp. 868–875, Apr. 1995.

[113] G. Gabbiani, G. B. Ryan, and G. Majne, "Presence of modified fibroblasts in granulation tissue and their possible role in wound contraction," *Experientia*, vol. 27, no. 5, pp. 549–550, May 1971, doi: 10.1007/BF02147594.

[114] J. J. Tomasek, G. Gabbiani, B. Hinz, C. Chaponnier, and R. A. Brown, "Myofibroblasts and mechano-regulation of connective tissue remodelling," *Nat. Rev. Mol. Cell Biol.*, vol. 3, no. 5, pp. 349–363, May 2002, doi: 10.1038/nrm809.

[115] P. Rousselle, M. Montmasson, and C. Garnier, "Extracellular matrix contribution to skin wound re-epithelialization," *Matrix Biol.*, vol. 75–76, pp. 12–26, Jan. 2019, doi: 10.1016/j.matbio.2018.01.002.

[116] M. Xue and C. J. Jackson, "Extracellular Matrix Reorganization During Wound Healing and Its Impact on Abnormal Scarring," *Adv. Wound Care*, vol. 4, no. 3, pp. 119–136, Mar. 2015, doi: 10.1089/wound.2013.0485.

[117] S. M. Levenson, E. F. Geever, L. V. Chowley, J. F. Oates, C. W. Berard, and H. Rosen, "The Healing of Rat Skin Wounds:," *Ann. Surg.*, vol. 161, no. 2, pp. 293–308, Feb. 1965, doi: 10.1097/00000658-196502000-00019.

[118] P. Sensharma, G. Madhumathi, R. D. Jayant, and A. K. Jaiswal, "Biomaterials and cells for neural tissue engineering: Current choices," *Mater. Sci. Eng. C*, vol. 77, pp. 1302–1315, 2017, doi: 10.1016/j.msec.2017.03.264.

[119] S.-K. Tae, S.-H. Lee, J.-S. Park, and G.-I. Im, "Mesenchymal stem cells for tissue engineering and regenerative medicine," *Biomed. Mater.*, vol. 1, no. 2, pp. 63–71, Jun. 2006, doi: 10.1088/1748-6041/1/2/003.

[120] L. Warren *et al.*, "Highly Efficient Reprogramming to Pluripotency and Directed Differentiation of Human Cells with Synthetic Modified mRNA," *Cell Stem Cell*, vol. 7, no. 5, pp. 618–630, Nov. 2010, doi: 10.1016/j.stem.2010.08.012.

[121] D. Kim *et al.*, "Generation of Human Induced Pluripotent Stem Cells by Direct Delivery of Reprogramming Proteins," *Cell Stem Cell*, vol. 4, no. 6, pp. 472–476, Jun. 2009, doi: 10.1016/j.stem.2009.05.005.

[122] K. Okita, M. Nakagawa, H. Hyenjong, T. Ichisaka, and S. Yamanaka, "Generation of Mouse Induced Pluripotent Stem Cells Without Viral Vectors," *Science*, vol. 322, no. 5903, pp. 949–953, Nov. 2008, doi: 10.1126/science.1164270.

[123] K. K. Hirschi, S. Li, and K. Roy, "Induced Pluripotent Stem Cells for Regenerative Medicine," *Annu. Rev. Biomed. Eng.*, vol. 16, no. 1, pp. 277–294, Jul. 2014, doi: 10.1146/annurev-bioeng-071813-105108.

[124] K. Shimoji *et al.*, "G-CSF Promotes the Proliferation of Developing Cardiomyocytes In Vivo and in Derivation from ESCs and iPSCs," *Cell Stem Cell*, vol. 6, no. 3, pp. 227–237, Mar. 2010, doi: 10.1016/j.stem.2010.01.002.

[125] Y.-C. Kuo and M.-J. Huang, "Material-driven differentiation of induced pluripotent stem cells in neuron growth factor-grafted poly(ε-caprolactone)-poly(β-hydroxybutyrate) scaffolds," *Biomaterials*, vol. 33, no. 23, pp. 5672–5682, Aug. 2012, doi: 10.1016/j.biomaterials.2012.04.046.

[126] Y.-F. Chen, C.-Y. Tseng, H.-W. Wang, H.-C. Kuo, V. W. Yang, and O. K. Lee, "Rapid generation of mature hepatocyte-like cells from human induced pluripotent stem cells by an efficient three-step protocol," *Hepatology*, vol. 55, no. 4, pp. 1193–1203, Apr. 2012, doi: 10.1002/hep.24790.

[127] C. Mauritz *et al.*, "Generation of Functional Murine Cardiac Myocytes From Induced Pluripotent Stem Cells," *Circulation*, vol. 118, no. 5, pp. 507–517, Jul. 2008, doi: 10.1161/CIRCULATIONAHA.108.778795.

[128] H. Composites and Y. Luo, "gels The E ff ect of Halloysite Addition on the Material Properties of Chitosan – Halloysite," pp. 1–18, 2019.

[129] P.-H. Lin, M. Sermersheim, H. Li, P. H. U. Lee, S. M. Steinberg, and J. Ma, "Zinc in Wound Healing Modulation," *Nutrients*, vol. 10, no. 1, p. 16, Dec. 2017, doi: 10.3390/nu10010016.

[130] M. A. Matica, F. L. Aachmann, A. Tøndervik, H. Sletta, and V. Ostafe, "Chitosan as a Wound Dressing Starting Material: Antimicrobial Properties and Mode of Action," *Int. J. Mol. Sci.*, vol. 20, no. 23, p. 5889, Nov. 2019, doi: 10.3390/ijms20235889.

[131] S. Same, S. A. Nakhjavani, G. Samee, G. Navidi, Y. jahanbani, and S. Davaran, "Halloysite clay nanotube in regenerative medicine for tissue and wound healing," *Ceram. Int.*, vol. 48, no. 21, pp. 31065–31079, Nov. 2022, doi: 10.1016/j.ceramint.2022.05.037.

[132] R. A. Bozym *et al.*, "Free zinc ions outside a narrow concentration range are toxic to a variety of cells in vitro," *Exp. Biol. Med. Maywood NJ*, vol. 235, no. 6, pp. 741–750, Jun. 2010, doi: 10.1258/ebm.2010.009258.

[133] J. Liu *et al.*, "Zinc oxide nanoparticles induce toxic responses in human neuroblastoma SHSY5Y cells in a size-dependent manner," *Int. J. Nanomedicine*, vol. 12, pp. 8085–8099, Nov. 2017, doi: 10.2147/IJN.S149070.

[134] A. Mittag, A. Singer, C. Hoera, M. Westermann, A. Kämpfe, and M. Glei, "Impact of in vitro digested zinc oxide nanoparticles on intestinal model systems," *Part. Fibre Toxicol.*, vol. 19, no. 1, p. 39, May 2022, doi: 10.1186/s12989-022-00479-6.

[135] A. R. N. Reddy, "Evaluation of In Vitro Cytotoxicity of Zinc Oxide (ZnO) Nanoparticles Using Human Cell Lines", doi: 10.23937/2572-4061.1510009.

[136] K. Govindasamy, M. H. Ramli, P. Pasbakhsh, V. Pushpamalar, and B. Salamatinia, "Chitosan/Cellulose/Halloysite Membranes Produced Using Solvent Casting Method," *Polym. Polym. Compos.*, vol. 23, no. 5, pp. 325–332, Jun. 2015, doi: 10.1177/096739111502300506.

[137] R. Kanagadurai, R. DURAIRAJAN, and R. Sankar, "Nucleation Kinetics, Growth and Characterization Studies of a Diamagnetic Crystal-Zinc Sulphate Heptahydrate (ZSHH)," *J. Chem.*, vol. 6, Jul. 2009, doi: 10.1155/2009/459656.

[138] Y.-L. Hu, W. Qi, F. Han, J.-Z. Shao, and J.-Q. Gao, "Toxicity evaluation of biodegradable chitosan nanoparticles using a zebrafish embryo model," *Int. J. Nanomedicine*, vol. 6, pp. 3351–3359, 2011, doi: 10.2147/IJN.S25853.

[139] M. Hanif, F. Jabbar, S. Sharif, G. Abbas, A. Farooq, and M. Aziz, "Halloysite nanotubes as a new drug-delivery system: a review," *Clay Miner.*, vol. 51, no. 3, pp. 469–477, Jun. 2016, doi: 10.1180/claymin.2016.051.3.03.

[140] K. Alam, M. Iqbal, A. Hasan, and N. Al-Maskari, "Rheological Characterization of Biological Hydrogels in Aqueous State," *J. Appl. Biotechnol. Rep.*, no. Online First, Jul. 2020, doi: 10.30491/jabr.2020.109994.

[141] M. Ahumada, E. Jacques, C. Calderon, and F. Martínez-Gómez, "Porosity in Biomaterials: A Key Factor in the Development of Applied Materials in Biomedicine," in *Handbook of Ecomaterials*, L. M. T. Martínez, O. V. Kharissova, and B. I. Kharisov, Eds., Cham: Springer International Publishing, 2019, pp. 3503–3522. doi: 10.1007/978-3-319-68255-6_162.

[142] D. Liu *et al.*, "Impact of Pore Size and Surface Chemistry of Porous Silicon Particles and Structure of Phospholipids on Their Interactions," *ACS Biomater. Sci. Eng.*, vol. 4, no. 7, pp. 2308–2313, Jul. 2018, doi: 10.1021/acsbiomaterials.8b00343.

[143] A. W. Bauer, W. M. Kirby, J. C. Sherris, and M. Turck, "Antibiotic susceptibility testing by a standardized single disk method," *Am. J. Clin. Pathol.*, vol. 45, no. 4, pp. 493–496, Apr. 1966.

[144] G. Priya, B. Madhan, U. Narendrakumar, R. V. Suresh Kumar, and I. Manjubala, "In Vitro and In Vivo Evaluation of Carboxymethyl Cellulose Scaffolds for Bone Tissue Engineering Applications," *ACS Omega*, vol. 6, no. 2, pp. 1246–1253, Jan. 2021, doi: 10.1021/acsomega.0c04551.

[145] J. Borovanský and P. A. Riley, "Cytotoxicity of zinc in vitro," *Chem. Biol. Interact.*, vol. 69, no. 2–3, pp. 279–291, 1989, doi: 10.1016/0009-2797(89)90085-9.

[146] B. Umbayev *et al.*, "Elevated levels of the small GTPase Cdc42 induces senescence in male rat mesenchymal stem cells," *Biogerontology*, vol. 19, no. 3–4, pp. 287–301, Jul. 2018, doi: 10.1007/s10522-018-9757-5.

[147] R. T. De Silva, P. Pasbakhsh, K. L. Goh, S.-P. Chai, and H. Ismail, "Physico-chemical characterisation of chitosan/halloysite composite membranes," *Polym. Test.*, vol. 32, no. 2, pp. 265–271, Apr. 2013, doi: 10.1016/j.polymertesting.2012.11.006.

[148] C. M. Dick, J. J. Liggat, and C. E. Snape, "Solid state 13C NMR study of the char forming processes in polychloroprene," *Polym. Degrad. Stab.*, vol. 74, no. 3, pp. 397–405, Jan. 2001, doi: 10.1016/S0141-3910(01)00174-4.

[149] M. Du, B. Guo, and D. Jia, "Thermal stability and flame retardant effects of halloysite nanotubes on poly(propylene)," *Eur. Polym. J.*, vol. 42, no. 6, pp. 1362–1369, Jun. 2006, doi: 10.1016/j.eurpolymj.2005.12.006.

[150] A. Escobar, N. Muzzio, and S. E. Moya, "Antibacterial Layer-by-Layer Coatings for Medical Implants," *Pharmaceutics*, vol. 13, no. 1, Art. no. 1, Jan. 2021, doi: 10.3390/pharmaceutics13010016.

[151] Y. Dhar and Y. Han, "Current developments in biofilm treatments: Wound and implant infections," *Eng. Regen.*, vol. 1, pp. 64–75, Jan. 2020, doi: 10.1016/j.engreg.2020.07.003.

[152] S. Murthy, P. Effiong, and C. C. Fei, "11 - Metal oxide nanoparticles in biomedical applications," in *Metal Oxide Powder Technologies*, Y. Al-Douri, Ed., in Metal Oxides. Elsevier, 2020, pp. 233–251. doi: 10.1016/B978-0-12-817505-7.00011-7.